

REPORT DOCUMENTATION PAGE			Form Approved OMB No. 0705-0188	
1. AGENCY USE ONLY (Leave blank)		2. REPORT DATE May 14, 1999	3. REPORT TYPE AND DATES COVERED Final Report 3/1/97 through 2/28/99	
4. TITLE AND SUBTITLE The Role of Microstructural Damage in the Thermal Diffusivity of Fiber-Reinforced Ceramic-Matrix Composites			5. FUNDING NUMBERS N00014-97-1-0394	
6. AUTHOR(S) Frank W. Zok				
7. PERFORMING ORGANIZATION NAME(S) AND ADDRESS(ES) Materials Department College of Engineering University of California Santa Barbara, CA 93106-5050			8. PERFORMING ORGANIZATION REPORT NUMBER 8-442490-25838	
9. SPONSORING/MONITORING AGENCY NAME(S) AND ADDRESS(ES) Office of Naval Research Program Officer Steven G. Fishman ONR 332 Ballston Centre Tower One 800 North Quincy Street Arlington, VA 22217-5660			10. SPONSORING/MONITORING AGENCY REPORT NUMBER	
11. SUPPLEMENTARY NOTES				
12A. DISTRIBUTION/AVAILABILITY STATEMENT Approved for public release.			12B. DISTRIBUTION CODE	
13. ABSTRACT (Maximum 200 words) <p>A phase-sensitive photothermal technique for the determination of the thermal diffusivity of solids and the thermal conductance of cracks and interfaces has been developed. The technique has been validated using a model systems comprising stainless steel disks, placed either in direct contact with each other or with thin polyethylene sheets between them. The corresponding heat flow analysis has also been developed.</p> <p>The technique has been used to study in detail the thermal conductance of delamination cracks in a unidirectionally reinforced ceramic composite, with measurements being made <i>in situ</i> under load. Special emphasis has been placed on the effects of the local crack opening displacement and fiber bridging. A model for the crack conductance that takes into account the contributions from both the air and the bridging fibers within the crack has been developed and validated by comparison with the measurements.</p> <p>Complementary studies have been performed of the effects of multiple matrix cracks on the in plane diffusivity of two unidirectional CMCs, with measurements being made in situ under uniaxial tensile loading. The effects of the cracks have been rationalized on the basis of a model that incorporates the matrix crack density, the crack opening displacement, and the Biot number associated with heat flow through the bridging fibers.</p> <p style="text-align: center; font-size: 2em; font-weight: bold;">1 9 9 9 0 6 0 1 1 4 4</p>				
14. SUBJECT TERMS Thermal diffusivity, crack conductance, ceramic composites.			15. NUMBER OF PAGES 16	
			16. PRICE CODE	
17. SECURITY CLASSIFICATION OF REPORT Unclassified	18. SECURITY CLASSIFICATION OF THIS PAGE Unclassified	19. SECURITY CLASSIFICATION OF ABSTRACT Unclassified	20. LIMITATION OF ABSTRACT	

Final Report on

THE ROLE OF MICROSTRUCTURAL DAMAGE IN THE THERMAL DIFFUSIVITY OF FIBER-REINFORCED CERAMIC- MATRIX COMPOSITES

Frank Zok

Materials Department
University of California
Santa Barbara, CA 93106-5050

EXECUTIVE SUMMARY

The present investigation has focused on the development and implementation of a phase-sensitive photothermal technique for measuring the thermal diffusivity of solids and thermal conductance of cracks, with emphasis on applications to ceramic matrix composites. The technique involves sinusoidally-modulated heating at one point on the surface of a specimen using a focused laser beam and measurement of the phase shift ϕ of the thermal wave at some other point. The unique characteristics of the test apparatus developed under the present program include the ability to probe materials at a relatively fine scale (in relation to conventional laser flash methods) and to make measurements *in situ* under load. The latter characteristic allows measurement of properties while cracks are open and hence provide maximum resistance to heat flow. A schematic of the apparatus is shown in Fig. 1. The corresponding theory needed for interpretation of the experimental measurements has also been developed.

CMCs with 2D fiber architectures exhibit two characteristic damage modes.

(i) Under in-plane tensile loading, the damage involves multiple matrix cracks

normal to the loading direction as well as interfacial debonding and sliding. The resulting nonlinear straining imparts high fracture toughness and low notch sensitivity. However, such cracks also impede heat flow in the plane containing the fibers, thereby reducing thermal conductivity. Furthermore, the debonding and sliding may reduce the conductance of the interfaces and hence reduce the transverse diffusivity. (ii) Under out-of-plane loading, failure occurs by delamination through the matrix, with relatively little resistance coming from the fibers. Delamination cracks present a particularly large impediment to heat flow in the through-thickness direction because of the relatively small amounts of fiber bridging and hence the large crack opening displacements. The effects of these two damage modes on the relevant thermal properties have been the focus of this investigation. The experiments have been performed on relatively simple unidirectional ceramic composites in which the damage modes are well understood.

In the absence of cracks, the key parameters governing the phase lag ϕ in the photothermal technique are: the distance, r , between the heat source and the location of temperature measurement; the heating frequency, f ; the thermal diffusivity, α ; and the specimen thickness, A . The theoretical analysis is presented in the appended articles by McDonald *et al.* (1999b) and by Ohson *et al.* (1999). Some representative numerical results are shown in Fig. 2(a). To illustrate the main effects of these parameters on ϕ , a limiting case that yields straightforward analytical solutions is considered. When the specimen thickness, A , is large compared with the distance, r , the phase lag along the top surface reduces to

$$\phi = \beta r = r \sqrt{\pi f / \alpha} \quad (1)$$

where β is the wave number. Consequently, the thermal diffusivity can be determined from a series of phase lag measurements, either at fixed distance r and

with varying frequency, f , or, alternatively, at fixed f and with varying r . A similar result applies to the point on the bottom surface directly across from the heat source; that is, $\phi = \beta A$ when $\beta A > 1$.

When a delamination crack exists along the midplane of the specimen, there is an additional phase lag across the specimen thickness, dependent on the nondimensional resistance parameter, $\rho \equiv h/2kA$, where h is the crack conductance and k is the thermal conductivity, $k = \alpha c$, with c being the volumetric heat capacity. Some representative numerical results are shown in Fig. 2(b) (McDonald *et al.*, 1999b; Ohson *et al.*, 1999). Again, to illustrate the main effects of ρ on ϕ , it is useful to consider a limiting case which yields a straightforward analytical result. Notably, when both the crack conductance and the frequency are sufficiently high, characterized by $\rho \ll 1$ and $\beta A > 1$, the phase lag on the bottom surface directly across from the heat source approaches

$$\phi = \beta A + \arctan \left[\frac{\rho \beta A}{1 + \rho \beta A} \right] \approx \beta A (1 + \rho) \quad (2)$$

Thus, the *additional* phase lag due to the crack is

$$\Delta \phi_c \approx \beta A (1 + \rho) - \beta A = \rho \beta A = \frac{c \sqrt{\pi f \alpha}}{2h} \quad (3)$$

This result illustrates how the crack conductance h can be determined from a series of phase lag measurements before and after cracking coupled with measurements of α and c . In the present studies, the measurements were made over a range of ρ and βA values that were outside the range for which Eqns. (2) and (3) are valid; consequently, the experimental data were fit by the complete solutions from the heat flow analysis in order to determine crack conductance.

In the presence of an array of parallel cracks, the in-plane conductivity is reduced by an amount dictated by another normalized resistance, $\rho_c \equiv h_c/ka$ where h_c is the conductance of each of the cracks and a is the crack spacing. The full numerical solutions for the phase lag measured normal to the crack planes is given in Dryden *et al.* (1999). At low frequencies, the phase lag ϕ_c across each crack is given by

$$\phi_c \approx \sqrt{1 + \rho_c} a/D \quad (4)$$

Comparisons between this approximation (labeled "equivalent solid model") and the exact numerical results are presented in Fig. 2(c). All of the present experiments on multiply cracked composites were performed at frequencies at which Eqn. (4) is valid, precluding the need for the full numerical solutions in interpreting the measurements.

The experimental techniques and the corresponding analysis to determine thermal diffusivity have been validated through measurements on a NIST standard stainless steel alloy (Fig. 3). Furthermore, the utility of the technique for probing interface properties has been demonstrated using model systems comprising steel disks with various types of interfaces or interlayers between them. Some typical results for steel/polyethylene/steel sandwich specimens are shown in Fig. 4.

The technique has been used to study in detail the thermal conductance of delamination cracks in a unidirectionally reinforced ceramic composite, with measurements being made *in situ* under load. Special emphasis has been placed on the effects of the local crack opening displacement and fiber bridging (Figs. 5-7). A model for crack conductance that takes into account the contributions from both the air and the bridging fibers within the crack has been developed. Measurements have been made of the key unknown properties in the model, notably the angle of

inclination of the fibers with respect to the matrix crack plane and the volume fraction of fibers contained within the crack. The latter results have been used to validate the predictive capability of the model, also shown in Fig. 7. The model is expected to find use in the design of CMC structures, especially for identifying the thermal loading conditions under which delamination may occur.

A complementary study has been performed of the effects of multiple matrix cracks on the in-plane diffusivity of the same Nicalon/MAS CMC. Measurements of both the longitudinal and transverse thermal diffusivity were made *in situ* while the test specimens were loaded in uniaxial tension. A surface replication technique was used to monitor and document the evolution of matrix cracking. The effects of cracks on the longitudinal diffusivity (Figs. 8 and 9) have been rationalized on the basis of a model that incorporates the matrix crack density, the crack opening displacement, and the Biot number associated with heat flow through the bridging fibers (Fig. 10) (McDonald *et al.* 1999c). Reductions in transverse diffusivity also arise following cracking, a result of interfacial debonding. Moreover, the longitudinal diffusivity is recovered to essentially the value for the pristine material following unloading, a consequence of almost complete closure of the cracks (Figs. 9(b) and 10). The latter difference highlights the importance of the *in-situ* measurements of diffusivity in the design and lifing of thermally-loaded CMC structures.

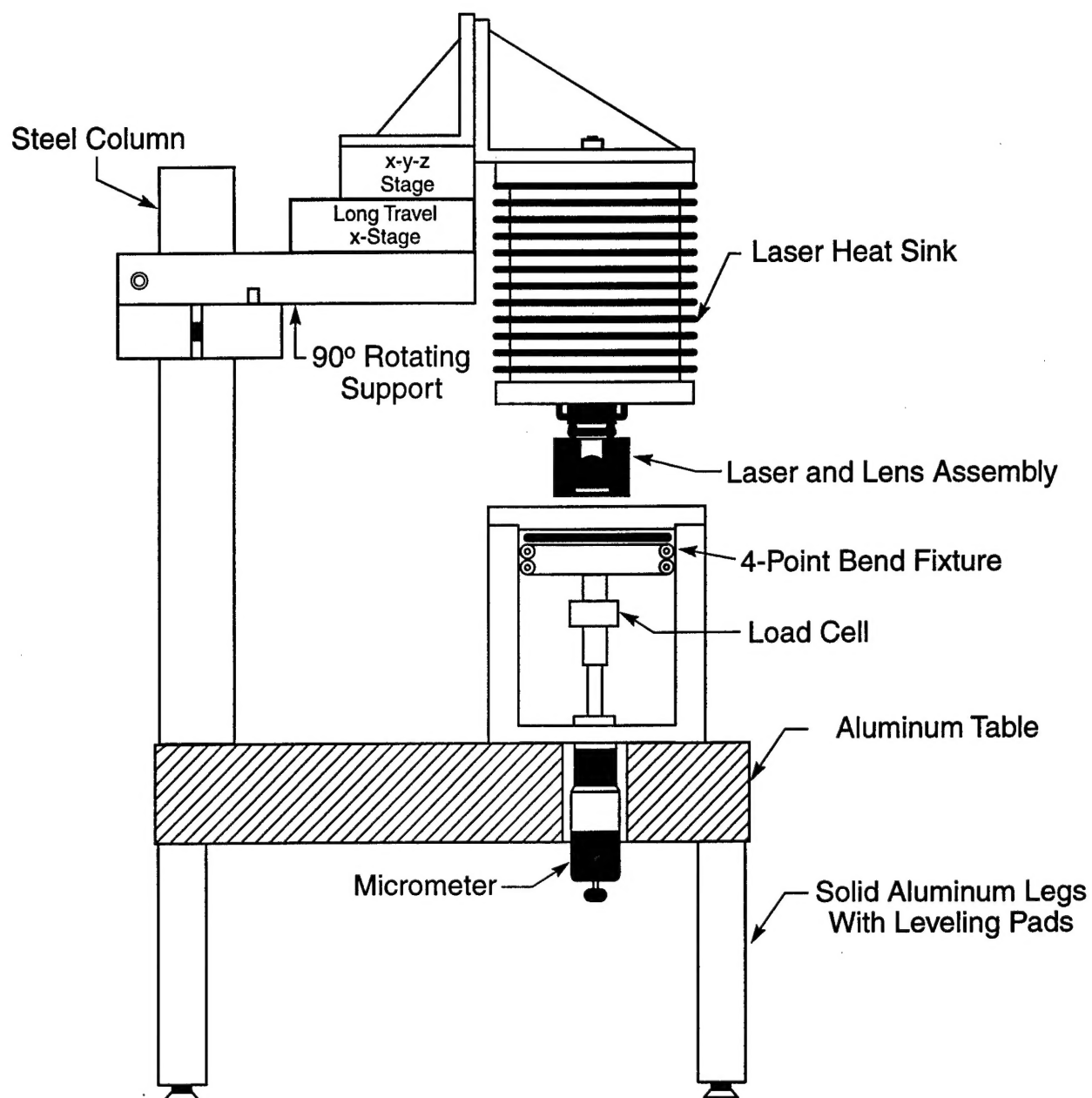


Figure 1 Schematic of apparatus for making photothermal measurements *in-situ* under load.

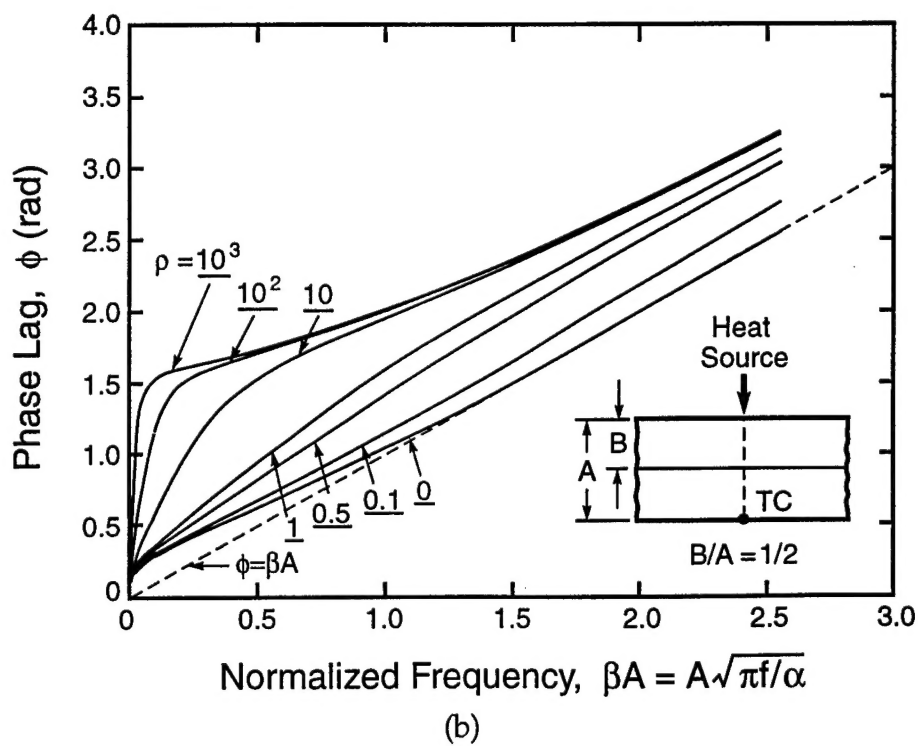
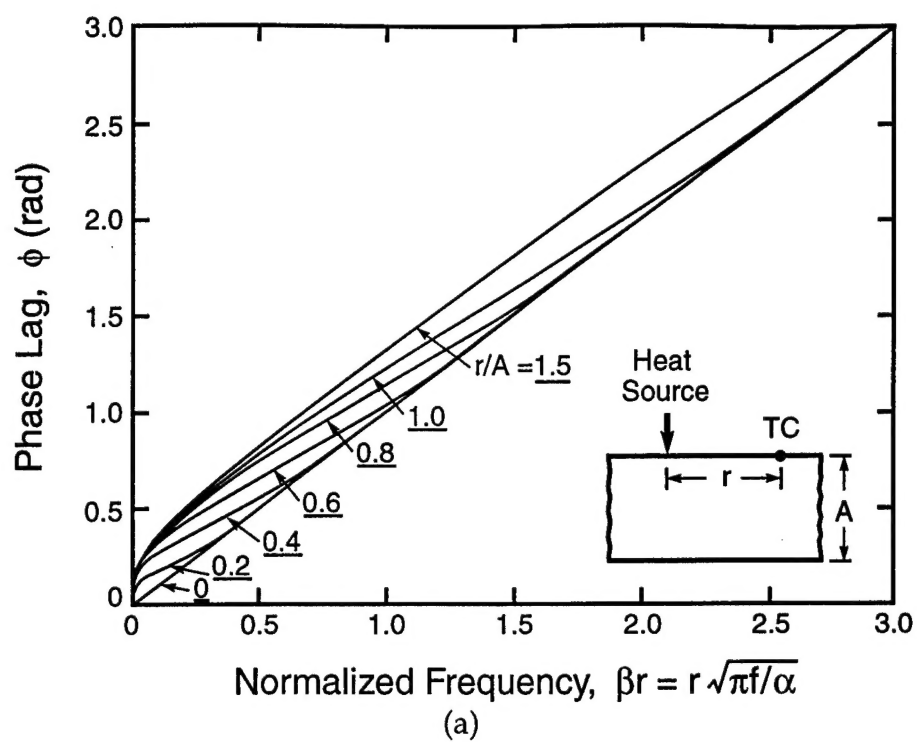
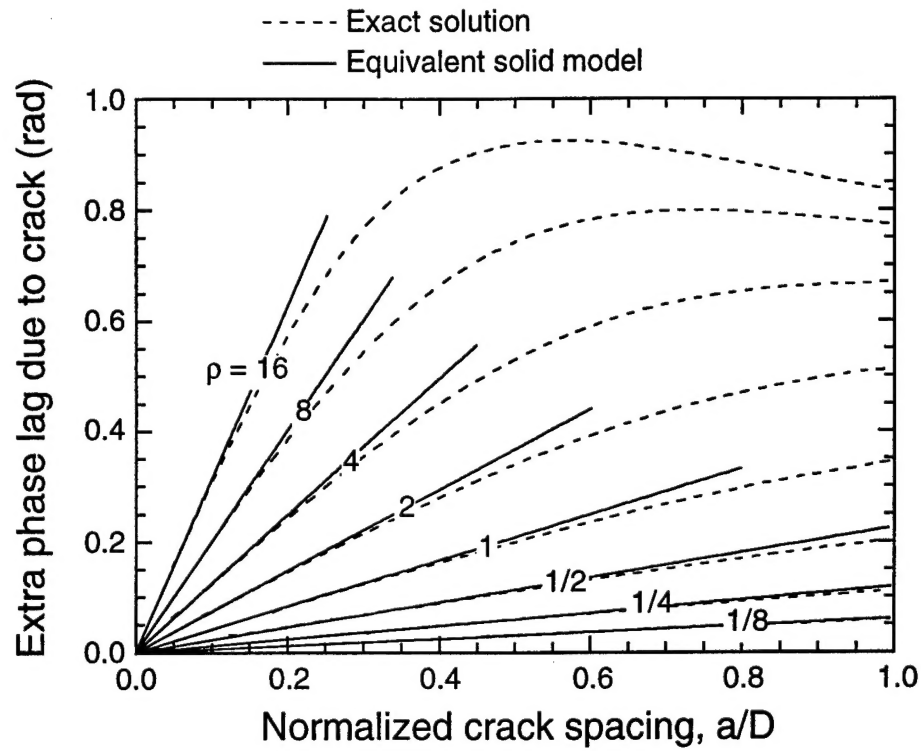


Fig. 2



(c)

Figure 2 Predictions of phase lag (a) in an uncracked specimen, measured on the top surface, (b) in a specimen containing a delamination crack at the mid-plane, measured directly across from the heat source, and (c) in a specimen containing an array of multiple cracks perpendicular to the direction of measurement.

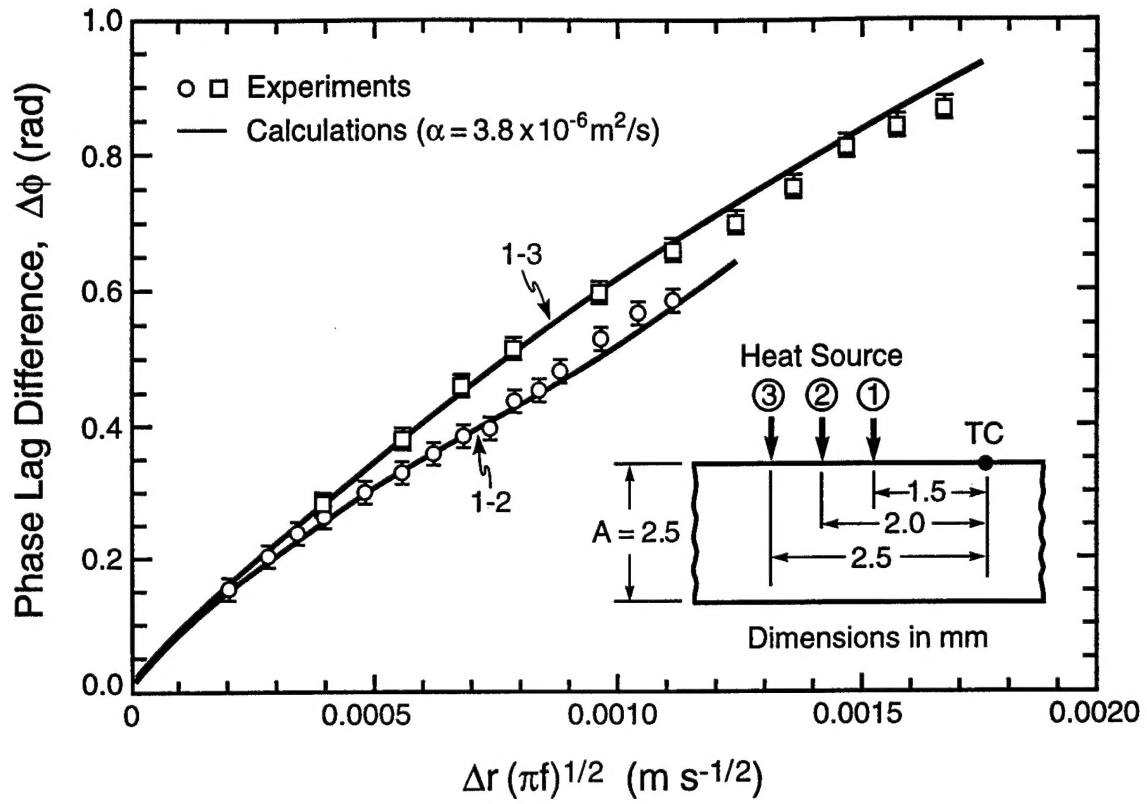
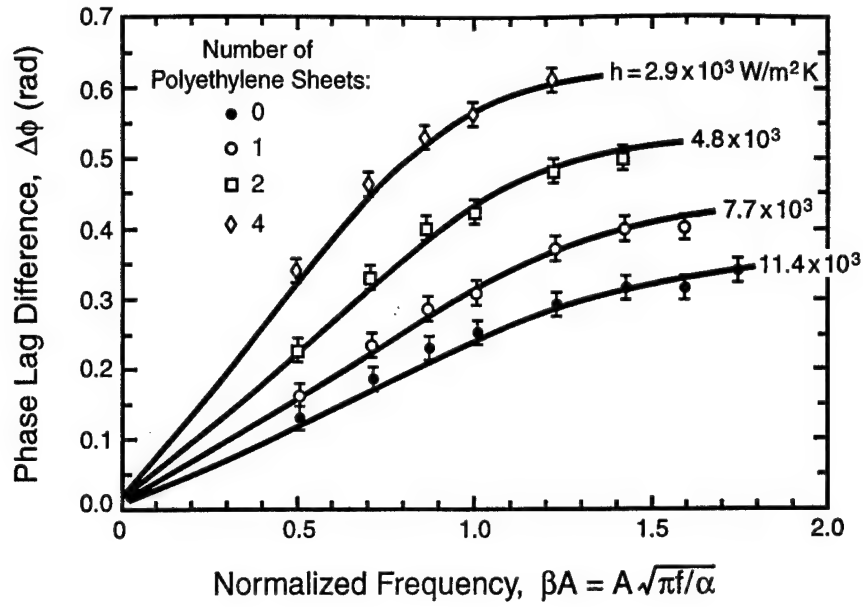
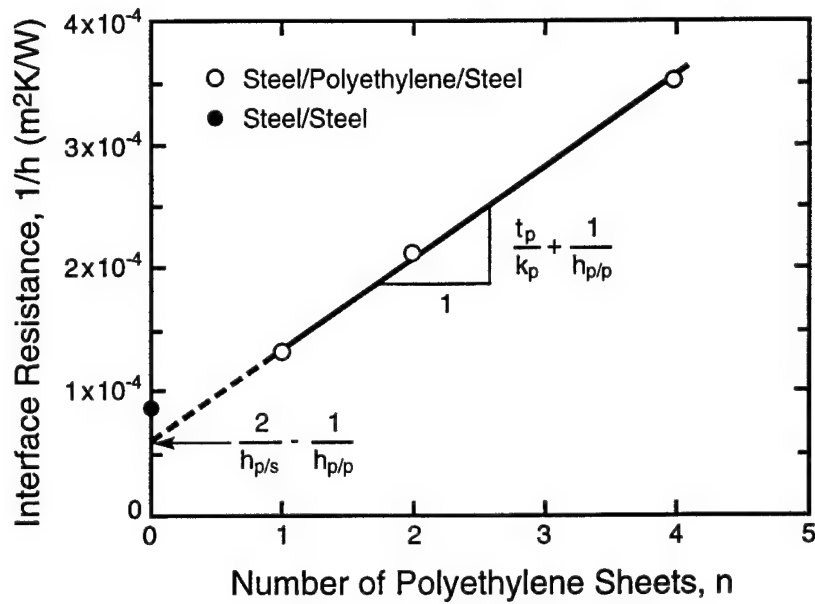


Figure 3 Validation of the thermal diffusivity technique, using a NIST standard stainless steel.



(a)



(b)

Figure 4 Experimental data and calculated curves for the phase lags obtained on the stainless steel sandwich specimens, showing the effects of the number, n , of polyethylene sheets on (a) the phase lag, $\Delta\phi_i$, associated with the interface itself, and (b) the interface conductance. The solid line in (b) is a least squares fit of the data for $n = 1, 2$ and 4 .

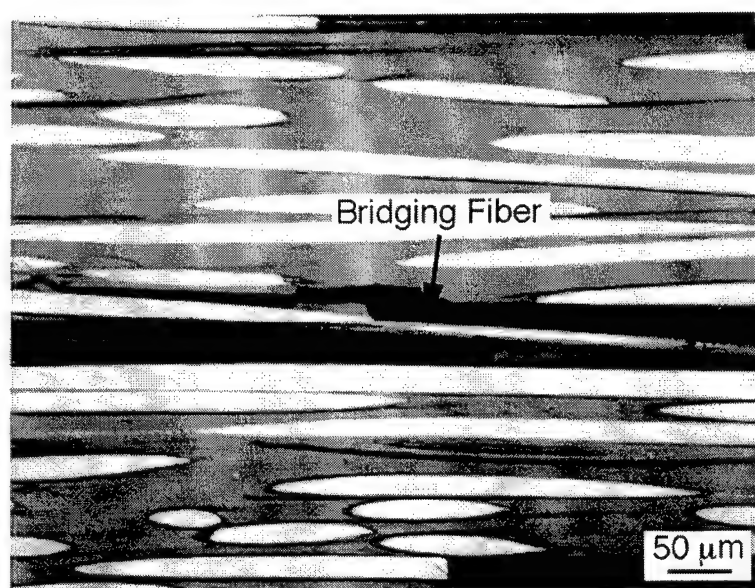
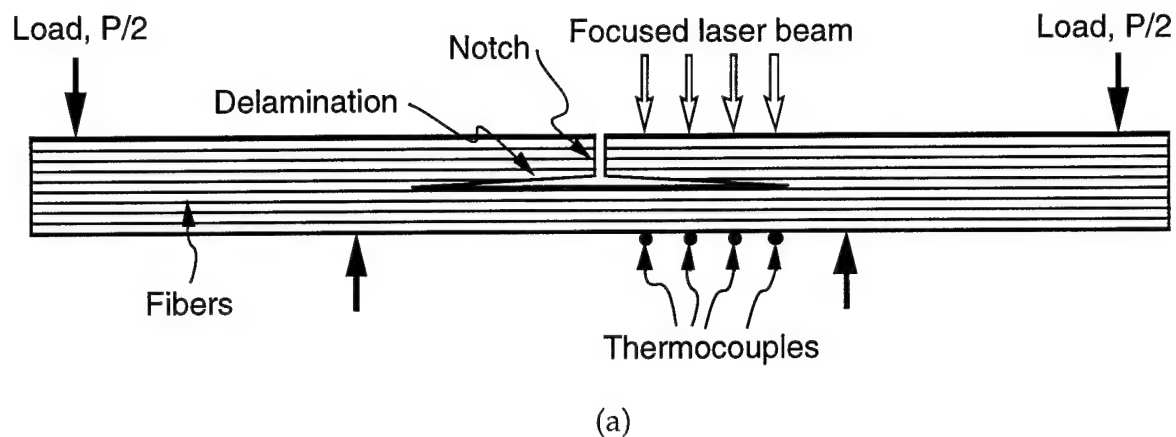


Figure 5 (a) Schematic of the specimen and loading configuration used to produce delamination cracks and subsequently measure their thermal conductance, and (b) example of a bridging fiber spanning the delamination crack.

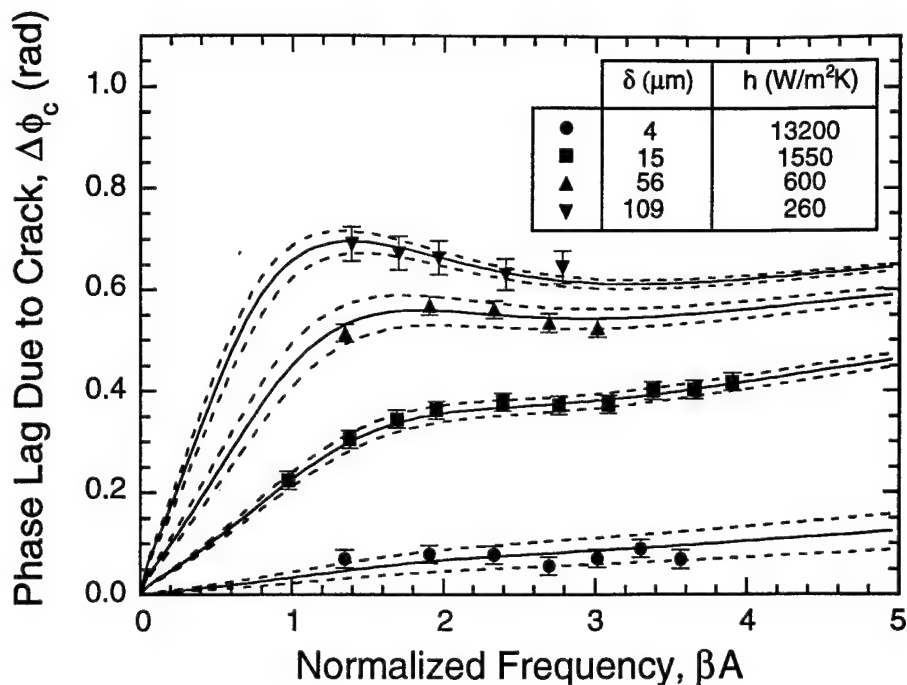


Figure 6 Typical measurements and calculations for the phase lag across a delamination crack at various opening displacements.

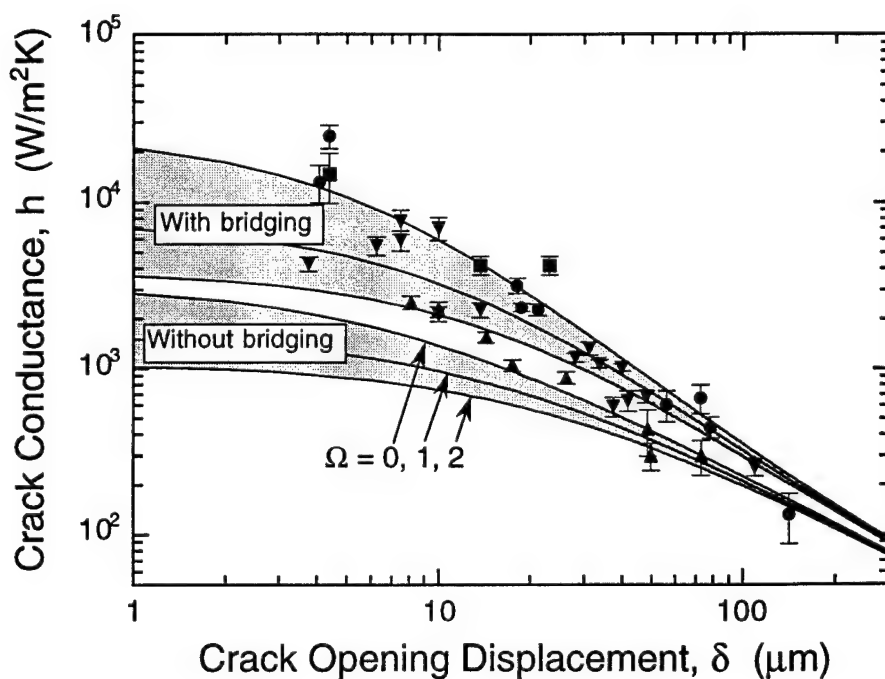


Figure 7 Comparisons of measured and predicted crack conductances in a unidirectional CMC. The top set of lines is based on the full crack bridging model; the bottom set is based on air conductance alone (without bridging). The parameter Ω characterizes the extent of matrix fragmentation during delamination.

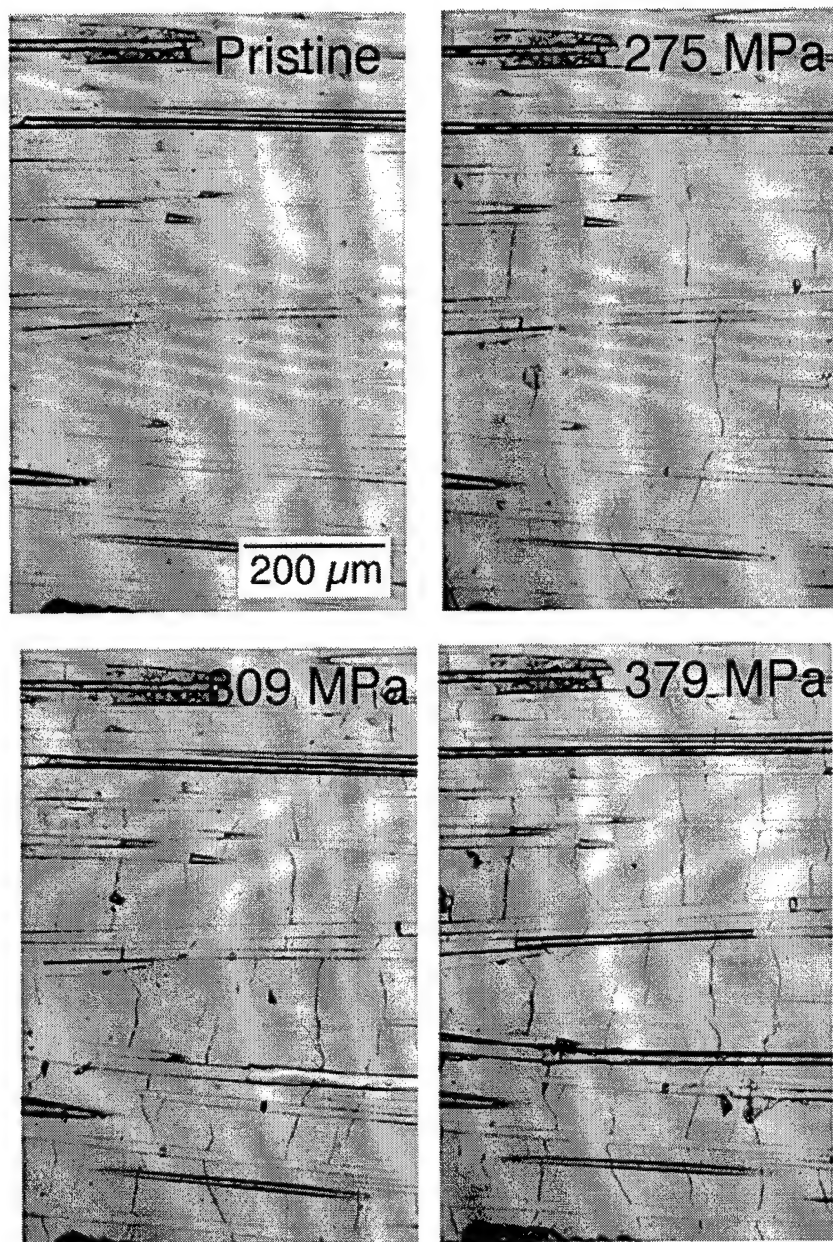


Figure 8 Micrographs showing the changes in crack density with increasing applied stress in the Nicalon/MAS composite. The micrographs are of the same region of the specimen, obtained from surface replicas.

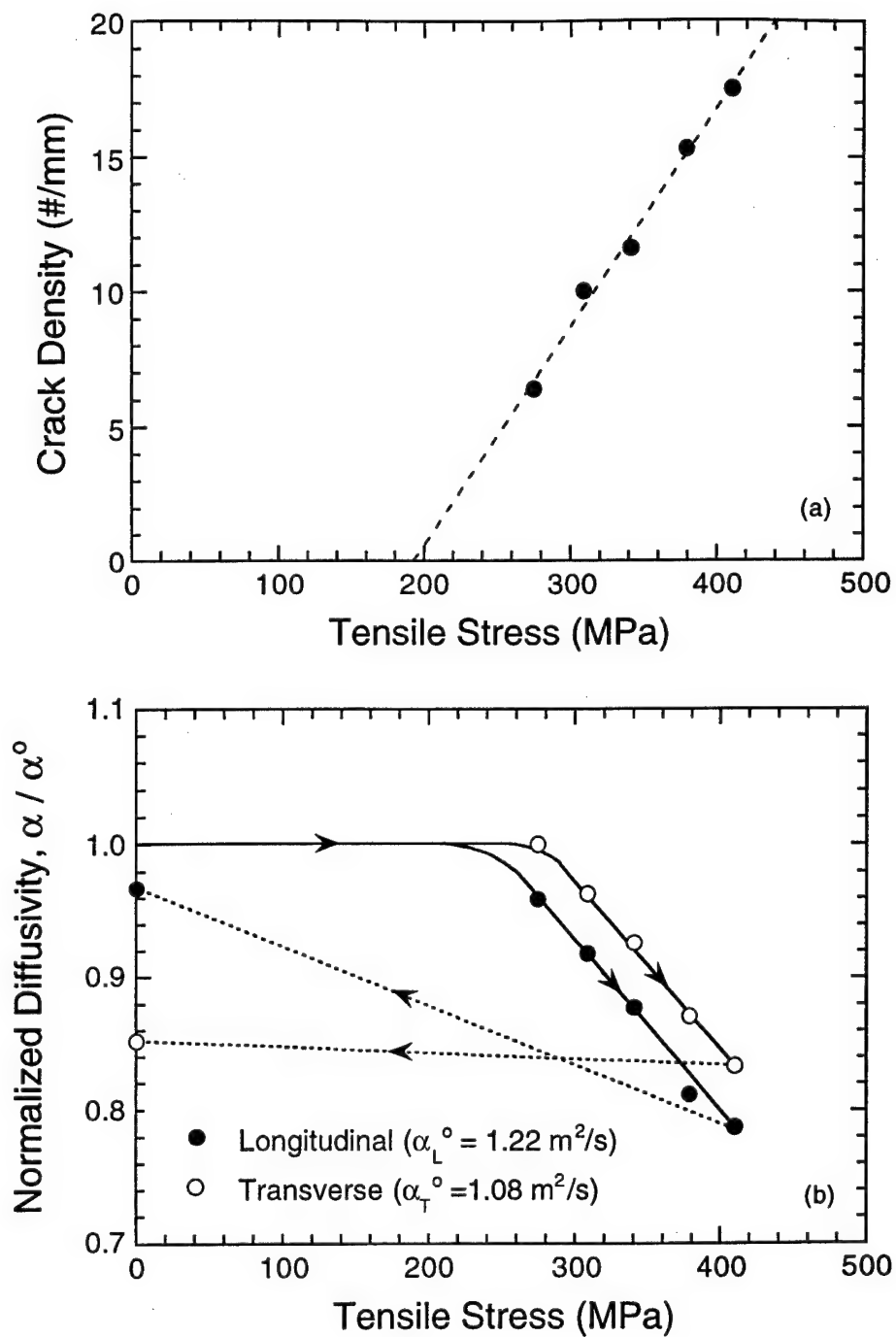


Figure 9 Changes in (a) crack density and (b) the longitudinal and transverse diffusivities of the Nicalon/MAS CMC with increasing tensile stress. Both the longitudinal and transverse diffusivity decrease with increasing stress, because of the corresponding increase in crack density.

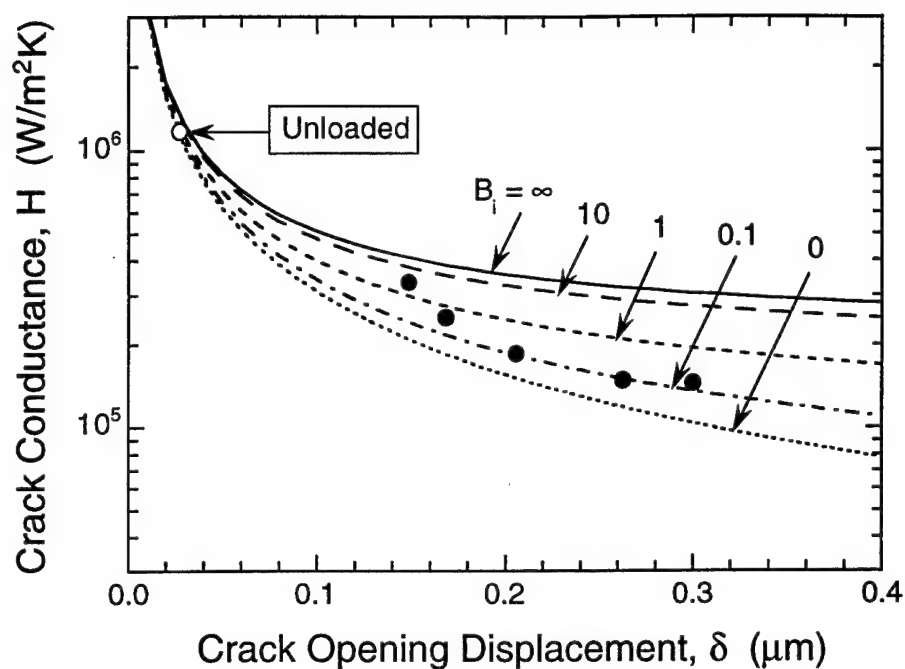


Figure 10 Variation in the crack conductance with crack opening displacement for Nicalon/MAS, obtained from both experimental measurements and model predictions. The Biot number is defined as $B_i \equiv h_i r / k_f$.

APPENDED MANUSCRIPTS:

1. K.R. McDonald, J.R. Dryden, A. Majumdar and F.W. Zok, "A Photothermal Technique for the Determination of the Thermal Conductance of Interfaces", submitted to *J. Heat Transfer*, 1999.
2. Y. Ohsone, G. Wu, J.R. Dryden, F.W. Zok and A. Majumdar, "Optical Measurement of Thermal Contact Conductance Between Wafer-Like Thin Solid Samples", *J. Heat Transfer*, in press (1999).
3. K.R. McDonald, J.R. Dryden, A. Majumdar and F.W. Zok, "Thermal Conductance of Delamination Cracks in a Fiber-reinforced Ceramic Composite", submitted to *J. Am. Ceram. Soc.*, 1999.

MANUSCRIPTS IN PREPARATION:

4. K.R. McDonald, J.R. Dryden, A. Majumdar and F.W. Zok, "Effects of Matrix Cracks on the Thermal Diffusivity of Unidirectionally Reinforced Ceramic Composites"
5. J.R. Dryden and F.W. Zok, "On the Interpretation of the Thermal Phase Lag in a Solid Containing Periodic Planar Cracks".



A PHOTOTHERMAL TECHNIQUE FOR THE DETERMINATION OF THE THERMAL CONDUCTANCE OF INTERFACES AND CRACKS

K.R. McDonald, J.R. Dryden*, A. Majumdar[‡] and F.W. Zok

Materials Department
University of California
Santa Barbara, California 93106

* On sabbatical leave from:
Department of Mechanical and Materials Engineering
University of Western Ontario
London, Ontario N6A 5B9
Canada

[‡] Department of Mechanical Engineering
University of California
Berkeley, California 94720

Submitted to
Journal of Heat Transfer

November, 1998
Revised April, 1999

ABSTRACT

The paper describes a phase-sensitive photothermal technique for the determination of the thermal conductance of an interface, a thin interlayer, or crack embedded within a plate. The technique involves sinusoidally-modulated heating at one point on the surface using a focused laser beam and measurement of the phase shift of the thermal wave at some other point. The technique is demonstrated using a model system comprising two stainless steel disks, placed either in direct contact with each other or with thin polyethylene sheets between them. The use of the technique for determining the conductance of delamination cracks in fiber-reinforced ceramic matrix composite is also demonstrated.

1. INTRODUCTION

The present article describes a photothermal technique for the determination of the thermal conductance of an interface or thin interlayer embedded within a plate. The technique is based on periodic heating at a point on one surface, using, for example, a focused laser beam, and measurement of the phase lag of the thermal wave at some other point. In the absence of an interface, the technique can be used to determine the thermal diffusivity of the material. The relevant theoretical analysis is presented in a recent paper by Ohsone *et al.* (1999). The work is motivated by concurrent studies on the thermal conductance of both delamination cracks in fiber-reinforced ceramic matrix composites and interfaces in multilayered structures for electronics packaging.

Photothermal techniques have been used extensively to study the thermal properties of materials (Hirshman, et al., 1961; Rosencwaig and Gersho, 1976; Rosencwaig, 1978; Maglic et al., 1984; Pessoa, Jr. et al., 1986; Reichling and Gronbeck, 1994; Kemp et al., 1995; Fabbri and Fenici, 1995; DeVecchio et al., 1995; Preston, 1995, 1996; Yu et al., 1996; Almond and Patel, 1996; Haji-Sheikh, et al., 1998). The techniques have been used also as nondestructive tools for detecting sub-surface defects (Almond and Patel, 1996; Opsal and Rosencwaig, 1982; Monchalín et al., 1981; Kuo et al., 1982; Grice et al., 1987; Yonushonis et al., 1992; Favro et al., 1993).

The focus of the present work is on one specific subgroup of these techniques, notably, that based upon periodic heating and phase lag measurement. The present technique provides quantitative information about the thermal conductance of interfaces. This information is crucial for thermomechanical analysis and failure prediction.

In the past, thermal contact conductances have been measured predominantly by DC techniques (Cooper et al., 1969; Fletcher, 1988; Madhusudana and Fletcher, 1983; Williamson and Majumdar, 1992). These techniques require a heat flux, q , to flow through the interface as well as through the bulk of the two contacting solids. The temperature distribution in the bulk solid is measured and extrapolated to the interface to estimate the interfacial temperature jump, ΔT_i . The contact conductance is then estimated by the relation, $h = q/\Delta T_i$. Although this technique is widely used, it suffers from several drawbacks. First, the heat flux must be constant over the bulk of both contacting solids which requires insulation material to be placed around the specimen. Second, it requires a cooling unit to remove the heat from the system; otherwise, the temperature of the sample increases monotonically with time. Finally, since the temperature distribution needs to be measured in the bulk, the samples must be sufficiently thick for at least three thermocouples to be inserted. Consequently, the technique is not easily adapted for measurement in thin and small specimens or structures.

The AC technique described in the present paper has the advantage over the DC techniques that it does not require insulation of the system from the surroundings nor of a cooling unit to extract heat. Moreover, it can be performed relatively quickly on both large and small specimens. The technique is demonstrated using two materials systems: (i) a model system comprising two stainless steel disks, placed either in direct contact with each other or with thin polyethylene sheets between them, and (ii) a unidirectional fiber-reinforced ceramic matrix composite containing a delamination crack along the specimen midplane.

2. EXPERIMENTAL TECHNIQUES AND MATERIALS

Measurements of thermal diffusivity and conductance were made using the apparatus shown schematically in Fig. 1. The apparatus consists of a 0.5 W diode laser, mounted on a x-y-z

translation stage with a precision of $\sim 10\text{ }\mu\text{m}$, and modulated with a lock-in amplifier.

Temperatures were measured using Type T thermocouples with a bead size of $\sim 200\text{ }\mu\text{m}$. The thermocouples were affixed to the surfaces using epoxy. The phase lag ϕ at the thermocouple location was obtained by comparing the laser input signal with the thermocouple signal using the lock-in amplifier.

To mitigate the effects of the thermal resistance of the thermocouple and the surrounding epoxy, all measurements and subsequent analyses were based on the *differences* of phase lags relative to a reference measurement. For instance, in determining the thermal diffusivity, a series of measurements was made along the top (heated) surface at several locations away from the laser spot (shown by the inset in Fig. 3). The measurements were subsequently compared with the one made at the location nearest to the laser spot, yielding a phase lag difference, $\Delta\phi(\Delta r)$, where Δr is the difference in the distance from the reference point. It is subsequently demonstrated that this measurement approach coupled with the appropriate heat flow analysis yields accurate values of thermal diffusivity. In cases where the crack or interface conductance was to be determined, phase lag measurements were made on the surface opposite to the one being heated, normal to the interface or crack. The corresponding reference measurement was that made on an equivalent specimen in the absence of the interface or crack.

2.1 Interface Conductance in a Model Steel System

The effects of interfaces were studied using a series of model systems comprising two circular stainless steel disks with known thermal properties [#] (Table I), each ground and polished to a final thickness of 1.25 mm and a diameter of 34 mm. The disks were polished to produce a unidirectional lay. The RMS value of surface roughness, measured orthogonal to the polishing direction using a Sloan Dektak II profilometer, was $0.42\text{ }\mu\text{m}$. As a check on the current technique, measurements were first made on the steel disks alone and the measurements used to confirm the reported thermal diffusivity, α . The latter measurements were made at frequencies, f , ranging

[#] Obtained from the NIST Standard Reference Materials Program.

from $\sim 0.05 - 2.6$ Hz, and at three distances from the thermocouple location: $r = 1.5, 2.0$ and 2.5 mm.

Various types of "interfaces" were produced between the two steel disks. The first was obtained by simply clamping together the disks with two binder clips, with the polishing directions of the two surfaces oriented perpendicular to one another. The force associated with the clips was measured to be ≈ 50 N and the calculated average pressure was 0.015 MPa. The laser was focused on the top surface, directly above the thermocouple. Phase lag measurements were made over the frequency range 0.05 to 1 Hz. For comparison, a parallel series of measurements at the same frequencies was made on the pristine sample with the same total thickness (2.5 mm). The differences in phase lags in the two specimens at each frequency were used to determine the interface conductance. In order to study the effects of interlayers, thin sheets of a commercial linear low density polyethylene (LLDPE), ~ 13 μm thick, were placed between the steel disks, the disks clamped together and the phase lag measurements repeated. Specimens containing 1, 2 and 4 polyethylene sheets were characterized.

To increase the absorption of the incident laser beam, the samples were coated with a sputtered carbon layer that was less than 0.1 μm in thickness. Assuming that the carbon layer is amorphous, a conservative lower-limit estimate for the thermal diffusivity is on the order of 10^{-6} m^2/s . Hence, the upper limit for the phase difference due to the bulk of the carbon layer is about 0.2 mrad at a frequency of 1 Hz. This is negligible compared to the phase difference measured for the bulk samples. The interface between the carbon layer and the underlying sample could also pose a thermal resistance. However, since the interface is chemically bonded, it is expected that this resistance would be much lower than that of the bulk sample studied in this paper.

2.2 Thermal Conductance of Delamination Cracks in Ceramic Composites

Experiments were also performed on a unidirectional composite comprising 37% NicalonTM fibers in a matrix of a magnesium aluminosilicate (MAS) glass ceramic. A delamination crack was produced by notching a long rectangular specimen at the center transverse

to the fibers, and subsequently loading the specimen in four-point bending. The specimen and loading geometries are shown schematically in Fig. 2(a). Thermocouples were attached at several locations on the bottom side of the specimen. Upon loading, delamination cracks initiated from the notch and propagated along the specimen length. One such crack is shown in Figs. 2(b) and (c). A notable feature in (c) is the presence of an inclined fiber spanning the crack faces.

The thermal conductance of the crack at various locations was determined through a series of phase lag measurements across the specimen thickness (directly over the thermocouples) both before and after delamination. In addition, the opening displacement of the delamination crack at the location of measurement was obtained by replicating the side surface of the specimen using cellulose acetate tape and subsequently examining the replicas in an optical microscope. All phase lag measurements and surface replicas were taken under load.

3. EXPERIMENTAL RESULTS AND ANALYSIS

2.1 Model Steel System

The experimental measurements for the pristine steel specimen (without interfaces) are plotted in Fig. 3. The results are presented in the form of phase lag *differences*, $\Delta\phi$, obtained at two locations, separated by a distance Δr . Also shown on the figure are the calculated curves, using the analysis presented in Ohson *et al.* (1999) and the reported thermal diffusivity of the alloy ($\alpha = 3.8 \times 10^{-6} \text{ m}^2/\text{s}$). Excellent correlations are obtained between the calculated curves and the experimental measurements, providing validation of the test technique for measuring thermal diffusivity.

Figure 4(a) shows the results for the specimens containing an interface along the midplane. The results are presented in terms of the phase lag difference, $\Delta\phi_i$, associated with the interface. Also shown are the calculated curves that give the best fit to the data for each type of interface along with the corresponding values of the thermal conductance, h . The trends in the calculated phase lag with frequency for a fixed interface conductance closely follow the ones obtained experimentally. This self-consistency provides confidence in both the theoretical results and the

measurement technique. The variation in the effective interface resistance, $1/h$, with the number of polyethylene sheets is plotted in Fig. 4(b). The trend is linear (with the exception of the point at $n = 0$, corresponding to the contact between the two steel disks), and can be rationalized in the following way.

The effective thermal resistance of the interfacial region in the presence of the polyethylene sheets can be partitioned into three components:

$$\frac{1}{h} = \frac{2}{h_{p/s}} + \frac{n-1}{h_{p/p}} + \frac{nt_p}{k_p} \quad (1)$$

where n is the number of sheets. The first term represents the resistance associated with the two interfaces between the polyethylene and the stainless steel, each with a conductance $h_{p/s}$; the second is the resistance of the polyethylene/polyethylene interfaces, with each interface having a conductance $h_{p/p}$; and the third is the resistance of the polyethylene itself, with t_p being the thickness of one sheet and k_p the thermal conductivity of the polyethylene. For the purpose of comparing this model with the data in Fig. 4(b), Eqn. (1) is re-written as

$$\frac{1}{h} = \left[\frac{2}{h_{p/s}} - \frac{1}{h_{p/p}} \right] + n \left[\frac{t_p}{k_p} + \frac{1}{h_{p/p}} \right] \quad (2)$$

The resistance is predicted to increase linearly with n , which agrees well with the measured trend. Upon performing a linear regression analysis of the data and using the reported value for k_p (Table I) along with Eqn. (2), the relevant conductances were determined to be $h_{p/p} = 3.0 \times 10^4 \text{ W/m}^2 \text{ K}$ and $h_{p/s} = 2.1 \times 10^4 \text{ W/m}^2 \text{ K}$. By comparison, the measured conductance of the steel/steel interface is $h_{s/s} = 1.1 \times 10^4 \text{ W/m}^2 \text{ K}$.

The ranking of the three conductance values can be further rationalized on the basis of surface roughnesses and the elastic/plastic properties of the constituent phases. Notably, because of the roughness of the stainless steel disks and the high modulus and strength of the steel, the interface conductance $h_{s/s}$ is expected to be the lowest of the three. The polyethylene has extremely

low modulus and yield stress and will readily deform locally upon contact with the steel, yielding a more conductive interface ($h_{p/s} > h_{s/s}$). Indeed, the measured values yield a ratio $h_{p/s}/h_{s/s} \approx 2$. Moreover, because of the smooth surfaces of the polyethylene sheets, the thermal contact between the polyethylene sheets is expected to be better yet. This, too, is in agreement with the experiments ($h_{p/p}/h_{p/s} \approx 1.5$).

At the most rudimentary level, the absolute value of the conductance of the steel/steel contact can be rationalized on the basis of the surface roughness, assuming that heat flow occurs by conduction through the air gap between the two surfaces. (The latter assumption can be justified on the basis of the very low pressures used in clamping the two disks together and thus the low area fraction of contacting asperities.) Thus the interface conductance is predicted to be

$$h \approx k_a / \delta \quad (3)$$

where k_a is the thermal conductivity of air at ambient temperature (0.024 W/mK) and d is the RMS separation between the two surfaces. Taking this separation to be approximately twice the RMS roughness of one of the two surfaces, the resulting predicted conductance is $h_{s/s} \approx 2.9 \times 10^4$ W/m² K, which is of the same order as the measured value of 1.1×10^4 W/m² K.

3.2 Thermal Conductance of a Delamination Crack

The results of three sets of measurements on the cracked composite specimen are presented in Fig. 5(a). Each corresponds to a different local crack opening displacement, as indicated on the figure. Clearly the phase lag associated with the delamination crack increases with increasing crack opening displacement. Also shown on Fig. 5(a) are the corresponding calculated curves using crack conductance values that yield the best fits to the experimental curves. In all cases, the shapes of the predicted curves are in good agreement with the measured ones.

The values of the inferred crack conductances are plotted against crack opening displacement in Fig. 5(b). Also shown are the predictions based on the assumption that the crack conductance is dictated by the air gap between the two crack surfaces, given by Eqn. (3). The latter prediction underestimates the measured conductance at small crack opening displacements.

However, the two appear to converge at larger crack opening displacements. The discrepancy can be attributed to the presence of bridging fibers of the type shown in Fig. 2(c), which must contribute to the crack conductance. Such bridging is expected to diminish with increasing crack opening because of failure of the bridging fibers. Indeed, once all the bridging fibers have failed, the crack conductance will be dictated by air conduction alone. This trend is in broad agreement with the experimental measurements. Studies are in progress to probe in more detail the contributions to thermal conductance from fiber bridging.

4. CONCLUDING REMARKS

The present technique of periodic heating and phase lag measurement provides a relatively simple and quick determination of both the thermal diffusivity of solids and the thermal conductance of embedded interfaces, interlayers and cracks. Temperature measurements can be made using standard thermocouples. The effects of the thermal resistance of the thermocouples are mitigated by using the differences in phase lag measurements relative to an appropriate reference state. In this way, the phase lag associated with the thermocouples is removed and the measurements then become a function only of the thermal properties of the system. The use of thermocouples is restricted to the low frequency regime, commensurate with the time constant associated with the thermocouple response. For time constants typical of most thermocouples (~ 10 ms), measurements can be made accurately in the frequency range used in the present experiments, *i.e.*, $f < 3$ Hz. At higher frequencies, alternate techniques for temperature measurement would be needed, such as the reflectance technique described by Ohson et al. (1999).

ACKNOWLEDGMENTS

Funding for this work was provided by ONR Contract No. N00014-97-1-0394 along with ARPA AASERT Award (Contract No. DAAH04-94-G-0374).

REFERENCES

- Almond, D.P. and Patel, P.M., (1996), Photothermal Science and Techniques, Chapman & Hall, London.
- Campbell, R., (1998), personal communication, Holometrix, Inc., Bedford, MA.
- Cooper, M.G., Mikic, B.B. and Yanovich, M.M., (1969), "Thermal Contact Conductance" *International Journal of Heat and Mass Transfer*, **12**, 279-300.
- Crawford, R.J., (1987), Plastics Engineering, Second edition, Pergamon Press, Oxford, UK, p. 33.
- DeVecchio, D., Russel, D. and Taborek, P., (1995), "Measurement of Thermal Diffusivity of Small, High Conductivity Samples Using a Phase Sensitive Technique", *Review of Scientific Instruments*, **66** [6], 3601-3605.
- Fabbri, L. and Fenici, P., (1995), "Three-dimensional Photothermal Radiometry for the Determination of Thermal Diffusivity of Solids", *Review of Scientific Instruments*, **66** [6], 3593-3600.
- Favro, L.D., Kuo, P.K., Thomas, R.L., and Shepard, S.M., (1993), "Thermal Wave Imaging for Aging Aircraft Inspection", *Materials Evaluation*, **51** [12], 1386-1389.
- Fletcher, L.S., (1988), "Recent Developments on Contact Conductance Heat Transfer", *ASME Journal of Heat Transfer*, **110**, 1059-1070.
- Grice, K.R., Inglehart, L.J., Favro, L.D., Kuo, P.K., and Thomas, R.L., (1983), "Thermal Wave Imaging of Closed Cracks in Opaque Solids", *Journal of Applied Physics*, **54** [11], 6245-6255.
- Haji-Sheikh, A., Hong, Y.S., You, S.M., and Beck, J.V., (1998) "Sensitivity Analysis for Thermophysical Property Measurements Using the Periodic Method", *J. Heat Transfer*, **120**, 568-576.
- Hirschman, A., et al., (1961), "An Optical Method for Measuring the Thermal Diffusivity of Solids", *International Developments in Heat Transfer*, Part IV, ASME, New York, pp.-863-869.
- Hust, J.G. and Lankford, A.B., (1984), "Standard Reference Materials 1460, 1461 and 1462: Austenitic Stainless Steel Thermal Conductivity and Electrical Resistivity as a Function of Temperature from 2 to 1200 K", National Bureau of Standards Certificate.
- Kemp, T., Srinivas, T.A.S., Fetting, R., and Ruppel, W., (1995), "Measurement of Thermal Diffusivity of Thin Films and Foils Using a Laser Scanning Microscope", *Review of Scientific Instruments*, **66** [1], 176-181.
- Kuo, P.K., Favro, L.D., Inglehart, L.J., Thomas, R.L., and Srinivasan, M., (1982), "Photoacoustic Phase Signatures of Closed Cracks", *Journal of Applied Physics*, **53** [2], 1258-1260.
- Madhusudana, C.V. and Fletcher, L.S., (1983), "Solid Spot Thermal Conductance of Zircaloy-2/Uranium Dioxide Interfaces", *Nuclear Science and Engineering*, **83**, 327-332.
- Maglic, K.D., Cezairliyan, A. and Peletsky, V.E., (1984), Compendium of Thermophysical Property Measurement Methods, Volume 1 Survey of Measurement Techniques, Plenum Press, New York, pp. 299-456.
- Monchalain, J.P., Parpal, J.L., Bertrand, L., and Gagne, J.M., (1981), "Thermal Contact Probing by the Photoacoustic Effect", *Applied Physics Letters*, **39** [1], 391-393.

Ohson, Y., Wu, G., Dryden, J.R., Zok, F.W. and Majumdar, A., (1999) "Optical Measurement of Thermal Contact Conductance Between Wafer-Like Thin Solid Samples", *J. Heat Transfer*, in press.

Opsal, J. and Rosencwaig, A., (1982), "Thermal-Wave Depth Profiling: Theory", *Journal of Applied Physics*, **53** [6], 4240-4241.

Pessoa, O. Jr., Cesar, C.L., Patel, N.A., Vargas, H., Ghizoni, C.C., and Miranda, L.C.M., (1986), "Two-beam Photoacoustic Phase Measurement of the Thermal Diffusivity of Solids", *Journal of Applied Physics*, **59** [4], 1316-1318.

Preston, S.D., (1995/1996), "A Review of Techniques for Measuring the Thermal Diffusivity of Thin Films and Coatings", *High Temperatures - High Pressures*, **27/28**, 111-134.

Reichling, M. and Gronbeck, H., (1994), "Harmonic Heat Flow in Isotropic Layered Systems and Its use for Thin Film Thermal Conductivity Measurements", *Journal of Applied Physics*, **75** [4], 1914-1922.

Rosencwaig, A., (1978), "Theoretical Aspects of Photoacoustic Spectroscopy", *Journal of Applied Physics*, **49** [5], 2905-2910.

Rosencwaig, A. and Gersho, A., (1976), "Theory of the Photoacoustic Effect with Solids", *Journal of Applied Physics*, **47** [1], 64-69.

Williamson, M. and Majumdar, A., (1992), "Effect of Surface Deformations on Contact Conductance", *ASME Journal of Heat Transfer*, **114**, 802-810.

Yonushonis, T.M., Stafford, R.J., Ahmed, T., Favro, L.D., Kuo, P.K., and Thomas, R.L., (1992), "Infrared Thermal Wave Imaging of Thermal Barrier Coatings for Diesel Applications", *American Ceramic Society Bulletin*, **71** [8], 1191-1202.

Yu, X.Y., Zhang, L. and Chen, G., (1996), "Thermal-wave Measurement of Thin-film Thermal Diffusivity with Different Laser Beam Configurations", *Review of Scientific Instruments*, **67** [6], 2312-2316.

Table I Thermal Properties of the Stainless Steel and the LLDPE

Material	Volumetric Heat Capacity, c (J/m ³ K)	Thermal Conductivity, k (W/mK)	Thermal Diffusivity, α (m ² /s)
Stainless Steel	3.8x10 ⁶ (Hust and Lankford, 1984; Campbell, 1998)	14.3 (Hust and Lankford, 1984)	3.8x10 ⁻⁶ *
LLDPE	2.1x10 ⁶ (Crawford, 1987)	0.33 (Crawford, 1987)	1.6x10 ⁻⁷ *

* Calculated from the other data, using $\alpha = k/c$.

FIGURE CAPTIONS

- Figure 1 Schematic of the experimental technique.
- Figure 2 (a) Schematic of the specimen and loading geometry used to cause delamination of the Nicalon/MAS composite specimen and subsequently determine the crack conductance. (b) Optical micrograph of a typical delamination crack. (c) Higher magnification view of the crack showing bridging by an inclined fiber.
- Figure 3 Phase lag measurements made on pristine steel specimen and the corresponding calculations from the analysis presented in Ohson *et al.* (1999). The error bars represent the maximum uncertainty in $\Delta\phi$, (0.017 rad), based on many repeat measurements under the same test conditions. The solid curves were calculated using the reported thermal diffusivity of the steel alloy, whereas the dotted curves represent calculations for thermal diffusivities that are either 8% higher or lower than the reported value.
- Figure 4 Experimental data and calculated curves for the stainless steel sandwich specimens, showing the effects of the polyethylene sheets on (a) the phase lag, $\Delta\phi_i$, associated with the interface itself, and (b) the interface conductance. The error bars in (b) represent the range of conductances needed to encompass the experimental data in (a). The solid line in (b) is a least squares fit of the data for $n = 1, 2$ and 4.
- Figure 5 Experimental data and calculated curves for the Nicalon/MAS composite specimens showing the effects of crack opening displacement on (a) the additional phase lag, $\Delta\phi_c$, and (b) the crack conductance. The error bars in (b) represent the range of conductances needed to encompass the experimental data in (a).

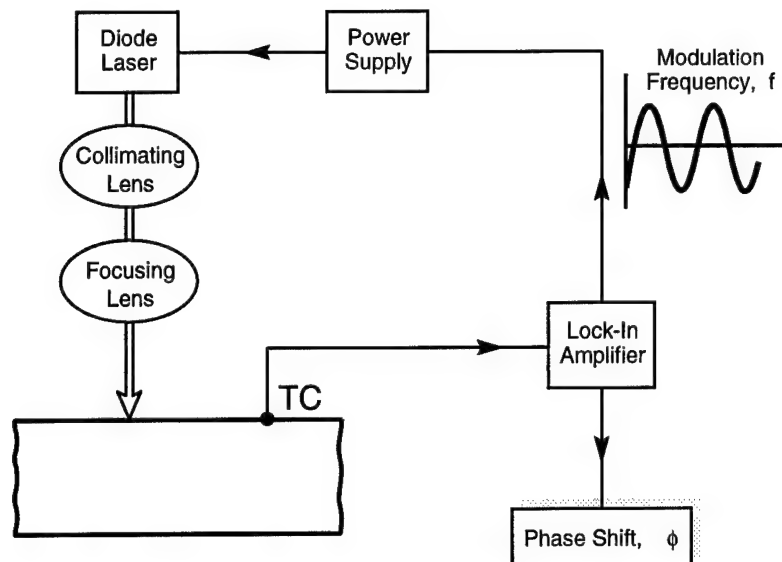


Figure 1 Schematic of the experimental technique.

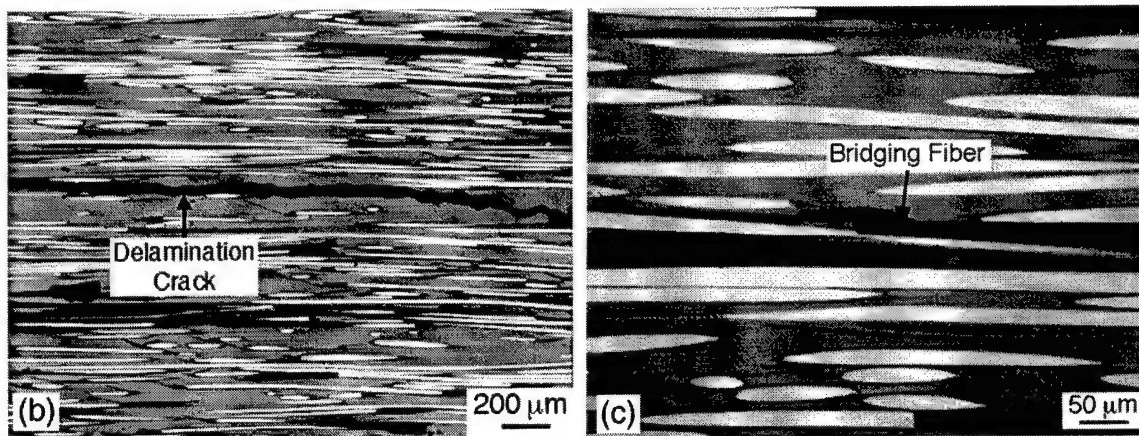
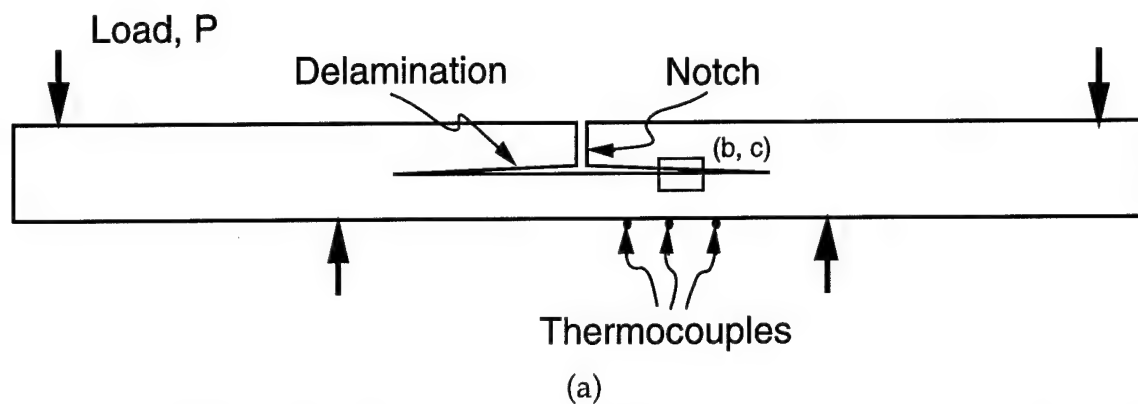


Figure 2 (a) Schematic of the specimen and loading geometry used to cause delamination of the Nicalon/MAS composite specimen and subsequently determine the crack conductance. (b) Optical micrograph of a typical delamination crack. (c) Higher magnification view of the crack showing bridging by an inclined fiber.

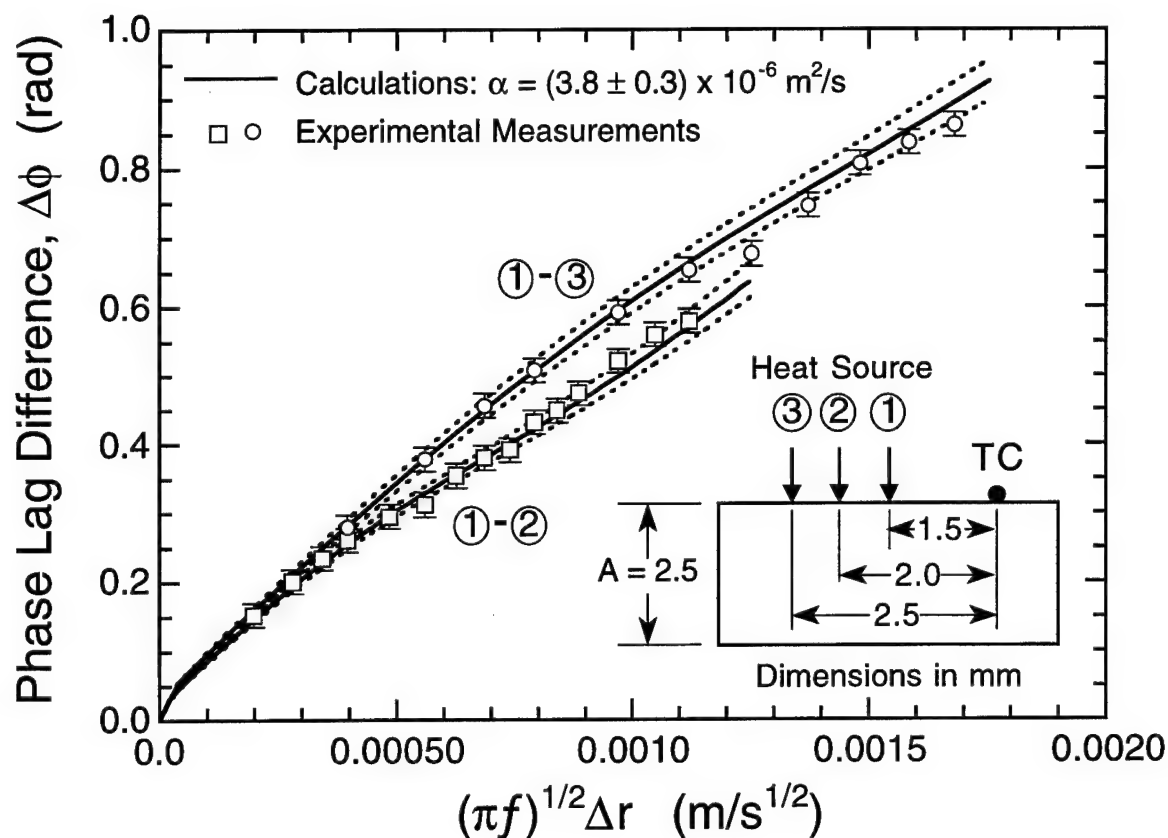


Figure 3 Phase lag measurements made on pristine steel specimen and the corresponding calculations from the analysis presented in Ohson *et al.* (1999). The error bars represent the maximum uncertainty in $\Delta\phi$, (0.017 rad), based on many repeat measurements under the same test conditions. The solid curves were calculated using the reported thermal diffusivity of the steel alloy, whereas the dotted curves represent calculations for thermal diffusivities that are either 8% higher or lower than the reported value.

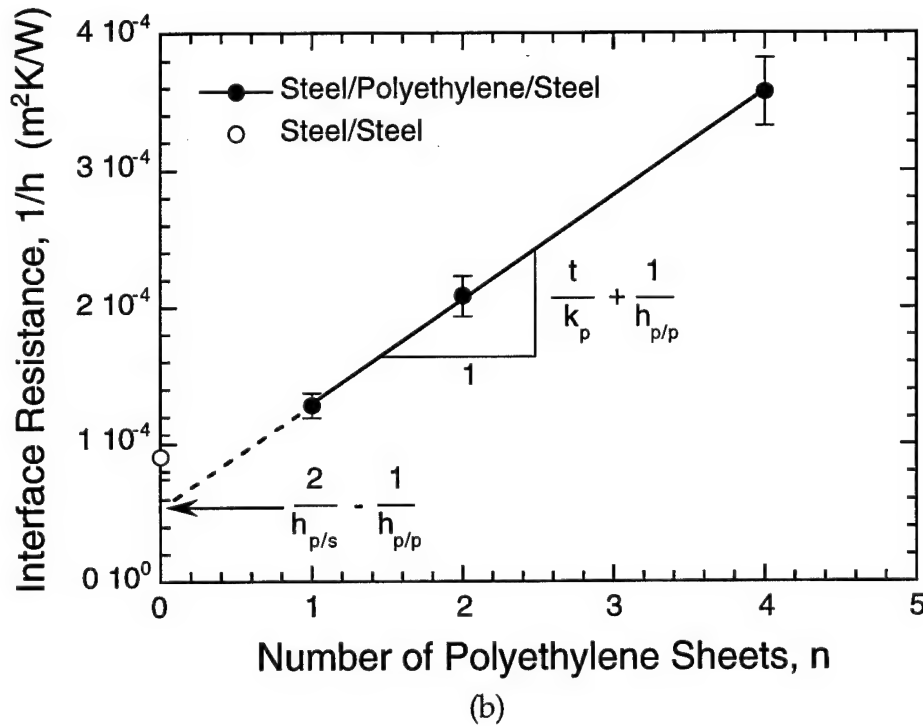
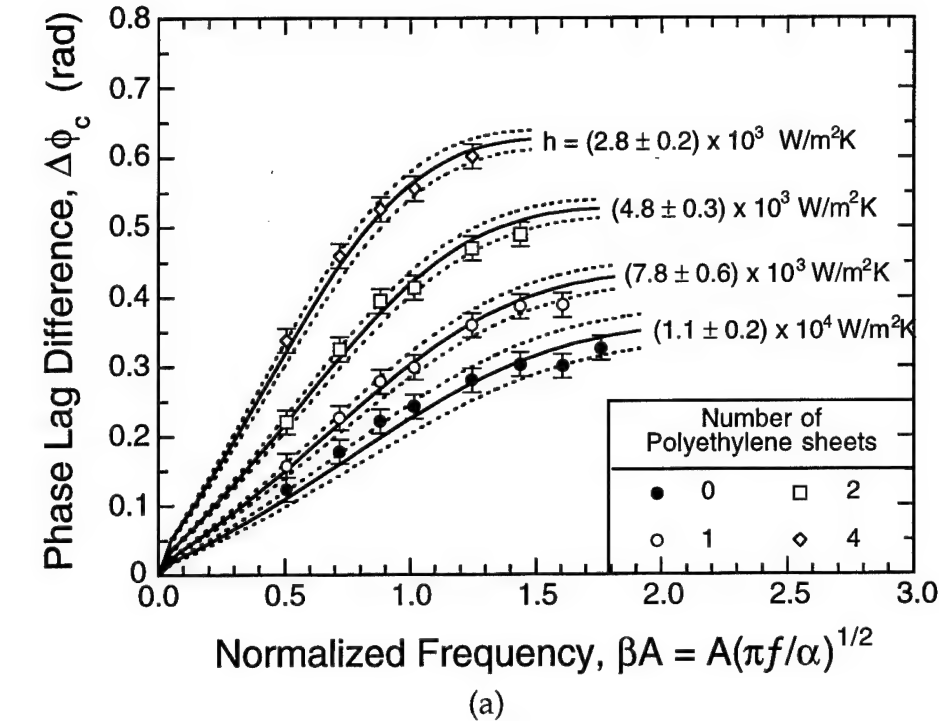


Figure 4 Experimental data and calculated curves for the stainless steel sandwich specimens, showing the effects of the polyethylene sheets on (a) the phase lag, $\Delta\phi_i$, associated with the interface itself, and (b) the interface conductance. The error bars in (b) represent the range of conductances needed to encompass the experimental data in (a). The solid line in (b) is a least squares fit of the data for $n = 1, 2$ and 4 .

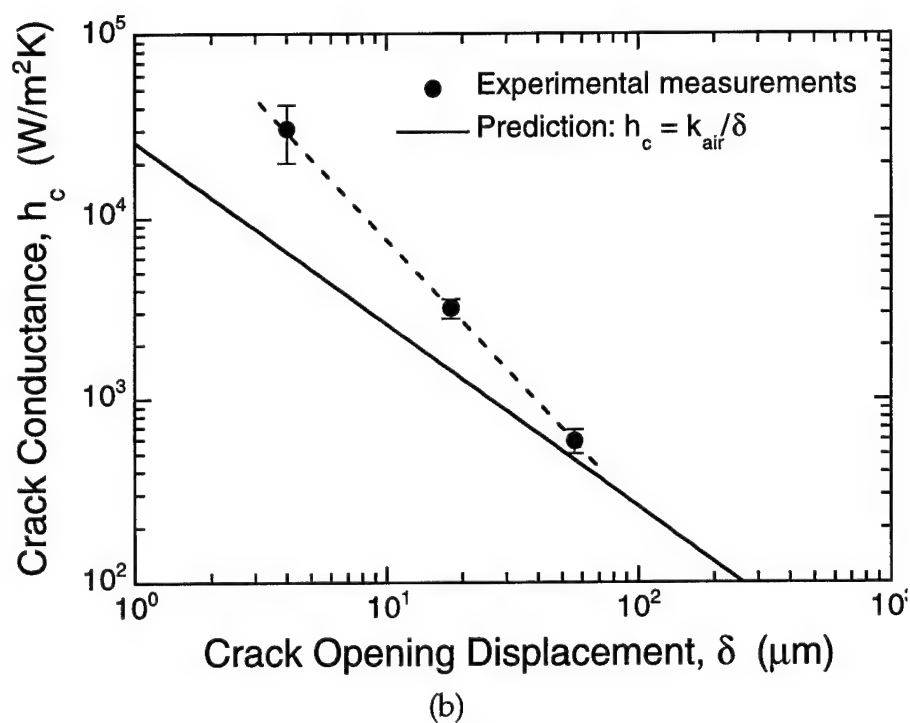
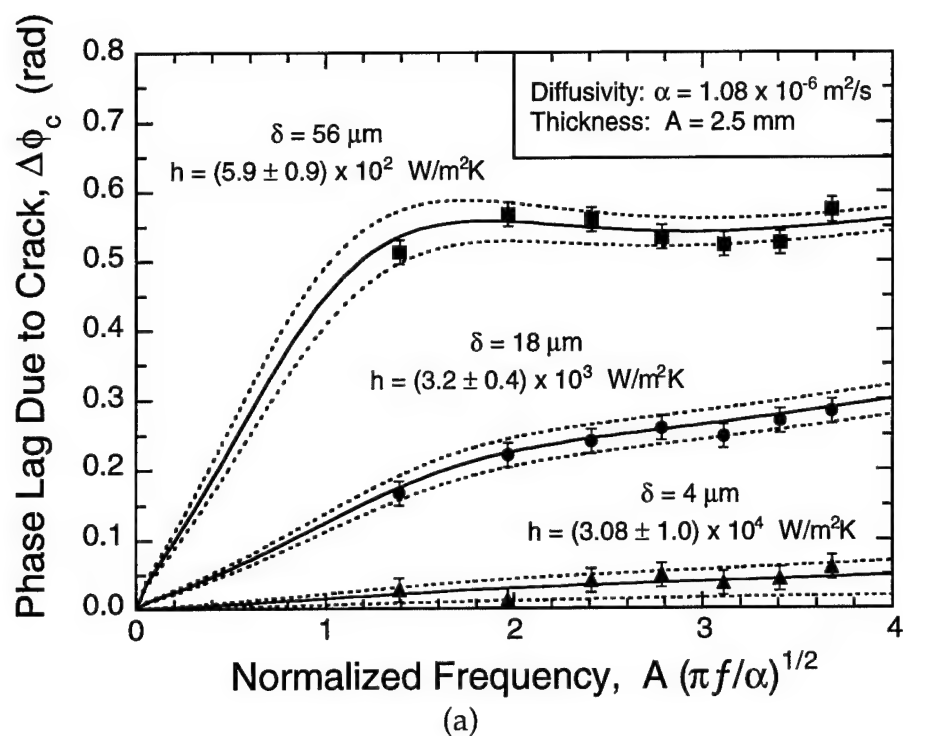


Figure 5 Experimental data and calculated curves for the Nicalon/MAS composite specimens showing the effects of crack opening displacement on (a) the additional phase lag, $\Delta\phi_c$, and (b) the crack conductance. The error bars in (b) represent the range of conductances needed to encompass the experimental data in (a).

Optical Measurement of Thermal Contact Conductance Between Wafer-Like Thin Solid Samples

Y. Ohsone¹, G. Wu, J.R. Dryden*, F.W. Zok[#] and A. Majumdar²

*Department of Mechanical Engineering
University of California
Berkeley, CA 94720, USA*

**Department of Mechanical and Materials Engineering
University of Western Ontario
London, Ontario N6A 5B9, Canada*

*[#]Materials Department
University of California
Santa Barbara, CA 93117*

Abstract

This paper presents a non-contact optical technique for measuring the thermal contact conductance between wafer-like thin solid samples. The technique is based on heating one solid surface by a modulated laser beam and monitoring the corresponding temperature modulation of the other solid surface across the interface using the reflectance of a probe laser beam. The phase lag between the two laser signals is independent of the optical properties of the samples as well as the laser intensities, and can be related to the thermal contact conductance. A detailed theoretical analysis is presented to estimate the thermal contact conductance as well as the thermophysical properties of the solids from the phase lag measured as a function of the modulation frequency. Closed form solutions in the high-frequency limit are derived in order to provide a simple estimation procedure. The effect of misalignment of the two lasers is studied and the conditions for robust measurements are suggested. As a benchmark for this technique, the thermal conductivity of a single crystal silicon sample was measured to within 2 percent of reported values. The thermal contact conductance was measured for Al-Si samples, each about 0.22 mm thick, in the pressure range of 0.8-10 MPa. In contrast to traditional contact conductance measurement techniques that require steady state operation and insertion of thermocouples in thick solid samples, the non-contact dynamic optical technique requires much less time and is particularly well suited for electronic packaging materials that are typically in the thickness range of 0.1-5 mm. In addition, localized conductance measurements are now possible with a spatial resolution of about four times the thickness of the solid and can be used to detect interfacial voids and defects.

¹ Visiting scholar from Mechanical Engineering Research Laboratory, Hitachi Ltd., 502 Kandatsu, Tsuchiura, Ibaraki 300-0013, Japan. Email: ohsone@merl.hitachi.co.jp

² To whom correspondence should be addressed. Email: majumdar@me.berkeley.edu

Nomenclature

a	radius of heating laser spot [m]
A	sample surface area [m ²]
b	coordinate along thickness of solid [m]
C	heat capacity [J/kg-K]
C_{TR}	coefficient of thermorefectance [1/K]
d	thickness of solid [m]
f	frequency [Hz]
F	load [N]
h	thermal contact conductance [W/m ² -K]
I	probe laser intensity [W]
k	thermal conductivity [W/m-K]
P	pressure [N/m ²]
q	heat flux [W/m ²]
Q	heating laser power absorbed [W]
r	radial coordinate [m]
R	reflectivity
s	Laplace transform variable
t	time [s]
T	temperature [K]
u	temperature [K]
v	Laplace transform of u
w	Hankel transform of v
z	vertical coordinate along thickness of solid [m]
α	thermal diffusivity [m ² /s]
β	spectral noise density of intensity [W/ $\sqrt{\text{Hz}}$]
χ	defined in equation (14)
λ	Hankel transform variable
μ	defined as $ (dh/d\phi)/h $ [1/rad]
ϕ	phase lag [radians]
ρ	density [kg/m ³]
ω	angular frequency [rad/s]

Subscripts

1	solid 1
2	solid 2

1. Introduction

The thermal contact conductance between two solid surfaces depends on a variety of factors such as the structure of surface roughness and waviness, surface hardness and elastic modulus, thermal conductivity, and surface damage of each surface, as well as the type of interstitial gas. Prediction of the thermal contact conductance has been a major challenge in the past, mainly due to the large uncertainty and complexity of surface properties. Although several theories have been developed to predict the thermal contact conductance (Cooper et al., 1969; Mikic, 1974; Fletcher, 1988; Majumdar and Tien, 1991; Nishino et al., 1995; Salgon et al., 1997; Lambert and Fletcher, 1997; Leung et al., 1998) it is rare to have agreement between theory and experiment to within 50 percent. Yet, thermal contact resistance is known to be a significant fraction of the total thermal resistance in electronic packages (Kraus and Bar-Cohen, 1983; Childres and Peterson, 1989). Therefore, its measurement, prediction, and control are critical to the thermal management of electronic and optoelectronic packages. In light of the difficulties in theoretical prediction, one must resort to measuring thermal contact conductance for conditions that are representative of those found in electronic packages. Such measurements can identify the upper and lower bounds for the value of thermal contact conductance and also provide the opportunity to try different schemes for increasing and controlling the conductance.

The technique that is widely used (Yovanovich, 1987; Seyed-Yagoobi et al., 1992; Williamson and Majumdar, 1992; Maddren and Marschall, 1995; Nishino et al., 1995) for measuring thermal contact conductance is illustrated in Fig. 1. Two solid pieces are brought together under compressive load while being heated on one side and cooled on the other. A series of thermocouples are inserted along the two solids to measure the temperature profile. At steady state, the linear profile is extrapolated to the interface to estimate the temperature jump, ΔT , at the interface. For a known heat flux, q , supplied by the heater and extracted by the cooler, the thermal contact conductance, h , is estimated by the relation, $h = q/\Delta T$. Since the heat flux, q , must be known, the solid pieces should be insulated along the length to reduce heat losses. This is often achieved in a vacuum environment. Although two thermocouples are sufficient to get a

temperature gradient, at least four in each solid are usually recommended for accuracy and to ensure that steady state is reached throughout the solid. The time required to reach steady state depends on the size or thermal mass of the system, and is usually about an hour or more for a typical laboratory set-up. Hence, a single data set of conductance versus load containing about eight data points requires at least a day.

Electronic packages contain solids such as semiconductor wafers as well as ceramic and metal substrates whose thickness range from 0.1 mm to about 5 mm. These are sometimes bonded together or often pressed under compressive load. To measure the contact conductance between such thin samples, the technique described in Fig. 1 cannot be used since it is practically impossible to insert four thermocouples within a distance of 1 mm. In addition, the steady-state technique can be prohibitively time consuming, specially when new control strategies and improvements must be explored. To measure the thermal conductance for a thin sample, it is usually sandwiched between two thick samples and measured with the experimental set-up of Fig. 1 where the thermocouples are then inserted in the thick sample (Seyed-Yagoobi et al., 1992; Mohr et al., 1997). However, this generates two interfaces between the thin sample and the surrounding materials. Hence, this technique requires that the thermal conductivity of the thin sample must be known and that the two interfaces must have exactly the same conductance. There is no direct method of measuring the thermal contact conductance of an interface between two thin samples.

In view of the need to measure thermal contact conductance of wafer-like thin samples, a different approach is proposed in this study. This technique relies on photothermal heating and optical temperature measurement and is, therefore, fully non-contact. Although photothermal and photoacoustic techniques have been used to characterize interfaces and their associated thermal boundary resistance (Lepoutre et al., 1985; Tam et al., 1986; Lachar, 1985), the new technique is based on a different temperature measurement method as described in section 2. Section 2 explains the principle underlying this technique and describes the experimental

apparatus. A theoretical analysis is needed to estimate the thermal contact conductance and thermophysical properties from the measured data, and is described in section 3. Section 4 presents the experimental results whereas the conclusions are in section 5.

2. Experiments

2.1 Principle Figure 2(a) describes the experimental technique used in this study. The intensity of the heating laser is modulated at a frequency, f , and focused on a spot on the top surface of solid 1. Absorption of this laser on the top surface sends out a thermal wave through the bulk and interface of solids 1 and 2. The bottom surface of solid 2 is coated with a gold film of about $0.5\ \mu\text{m}$ thickness. A probe laser is used to measure the temperature oscillation at frequency, f , of a spot on the gold surface directly under the heating laser spot through reflectance thermometry (Cardona, 1969; Rosei and Lynch, 1972). This technique is based on the temperature dependence of the optical constants of a material which leads to a temperature dependence of its reflectivity. Reflectance thermometry has been widely used for non-contact temperature measurement (Epperlein, 1993; Claeys et al., 1993; Qiu et al., 1993; Quintard et al., 1996; Ju and Goodson, 1997, 1998). A photodiode measures the reflected probe laser intensity and sends the output to a lock-in amplifier, which provides the amplitude and the phase of the signal at frequency, f . The signal amplitude depends on the absorbed power of the heating laser, the heating laser spot size, the coefficient of thermorefectance of gold, as well as the reflectivity of the gold surface. Since these quantities are not always precisely known or require significant effort in calibration, estimation of the thermal conductance from the signal amplitude is difficult. The phase lag, ϕ , between the probe and the heating lasers is, however, immune to these property uncertainties and can be directly related to the thermal conductance. Therefore, this study used the phase lag to estimate the thermal properties of and the thermal contact conductance between solids 1 and 2. These estimations require an elaborate theoretical model which is described in section 3.

2.2 Apparatus and Measurements Figure 2(b) shows the apparatus for the loading unit and the probe laser. The loading unit consisted of a loading wheel that was used to rotate a screw with a thread pitch of 100 μm . The load was applied to a spring box which contained 8 parallel compression springs each of 13930 N/m stiffness. The springs were chosen in a way that for a five degree rotation of the wheel, which was assumed to be the minimum change, the load changed by 5.5 N. The maximum travel of the springs was 1 cm which yielded the maximum load to be 1114.4 N. Since the samples were chosen to be 1 cm x 1 cm, the corresponding maximum pressure and the minimum change in pressure were 11.1 MPa and 55 kPa, respectively. A ball bearing was used to minimize any torsional load on the unit. The spring box had a sliding fit with the frame of the loading unit. A load cell was used in series to measure the force which was verified with the value calculated from the spring compression. A top cap was screwed on to the frame to provide a reactive force. A cut through the loading unit frame allowed the optical rail of the probe laser system to access the bottom surface of the sample. The samples were placed on ceramic sample holders which provided sufficient rigidity so that uniform load could be applied on the sample despite the hole at the center used for optical access. When the samples were too thin such that the surface pressure became non-uniform under compressive load, they were placed between two thick glass pieces. The glass pieces provided optical access while ensuring rigidity and uniform load on the sample.

Optical heating was provided by a diode laser emitting at 676 nm wavelength with a maximum power output of 550 mW. The power was modulated using the sinusoidal output from a lock-in amplifier which provided the input for the laser driver. The heating laser beam was focused on to a spot approximately 1 mm x 1 mm, yielding a flux in the range of $10^5 - 10^6$ W/m². To maximize the absorption of the heating laser, a 50 nm carbon coating was applied on the top surface of the top sample. The effect of this very thin film on the phase lag can be expected to be negligible. A HeNe laser with 0.4 mm beam diameter, 5 mW output power at 632.8 nm wavelength, and 1 mrad beam divergence was used as the probe laser. A prism-shaped mirror was used to direct the horizontal incident beam vertical and the vertical reflected beam

horizontal and on to a silicon photodiode. A gold film was deposited on the bottom surface as the highly-reflective layer. Although the thermorefectance coefficient of Si is higher than that of gold, the gold film was still used for its well-calibrated data and for applications in non-silicon cases. The photodiode had a noise equivalent power of $2.3 \times 10^{-14} \text{ W}/\sqrt{\text{Hz}}$, a conversion factor of 0.4 A/W at 632.8 nm, and was operated under a reverse bias of 9 V. The photocurrent was passed through a 10 K Ω resistor and the voltage output across the resistor was fed into the lock-in amplifier. Optical filters were used in front of the photodiode to block the heating laser beam at 676 nm and allow only the probe laser beam at 632.8 nm wavelength.

Optical alignment of the system was crucial. Both the heating and the probe lasers were mounted on x-y-z micropositioners. The probe laser beam was aligned onto the photodiode by moving one of the mirrors on the optical rail as well as by translating and rotating the HeNe laser. Before the experiments were started, it was important to ensure that the dc photodiode output was sufficiently high. The heating and the probe laser beams were also aligned, first visually and then by studying the output of the lock-in amplifier for the photodiode signal. Precise alignment of the heating and probing beams is rather difficult in the present experimental setup, but one can circumvent this difficulty as described in section 3. Although the alignment would be easier if both laser beams are focused on the same side of the sample, it can not be implemented in this technique since the heating of the sample requires a highly absorptive surface whereas reflectance thermometry requires a highly reflective one. Figure 3 shows a typical scan of the spectrum analyzer indicating the peak at 350 Hz corresponding to the thermorefectance signal. The white-noise floor in this spectrum corresponds to a spectral noise density, $\beta = 6 \times 10^{-9} \text{ W}/\sqrt{\text{Hz}}$. The dominant noise source, hence, was not from the photodiode but from another source, perhaps the laser.

The coefficient of thermorefectance, $C_{TR} = (dR/dT)/R$, of gold is on the order of 10^{-5} K^{-1} at 632.8 nm (Scouler, 1967; Cardona, 1969; Rosei and Lynch, 1972). The temperature resolution, ΔT_{min} , defined for a signal-to-noise ratio of 2 can be estimated by the relation

$$\Delta T_{min} = \frac{2\Delta I}{IRC_{TR}} = \frac{2\beta\sqrt{\Delta f}}{IRC_{TR}} \quad (1)$$

where $\Delta I = \beta\sqrt{\Delta f}$ is the noise in the intensity measurement for a bandwidth Δf of the lock-in amplifier, I is the probe laser intensity incident on the photodiode, and R is the reflectivity of the gold film at 632.8 nm wavelength. The typical bandwidth chosen for the measurements was $\Delta f = 7.8 \text{ MHz}$ which led to $\Delta I = 0.53 \text{ nW}$ for the white-noise floor in Fig. 3. A bandwidth of 7.8 MHz corresponds to a time constant of 10 s for the lock-in amplifier. Since it took at least 5-10 time constants for the measured phase to be stable, it required 1-2 minutes to measure the phase lag for a single experimental condition. This is much shorter than 30-60 minutes required for each data point for the steady-state technique illustrated in Fig. 1. Assuming some losses due to reflections from the glass surfaces, $I = 3 \text{ mW}$ for the probe laser. Using $R = 0.95$ and $C_{TR} = 10^{-5} \text{ K}^{-1}$ for gold, one can estimate using equation (1) the minimum detectable temperature change to be 0.04 K. Although the technique is based on phase measurements, the minimum detectable temperature is an important quantity since, as will be indicated by the theory, it determines the frequency range for the measurements.

The internal resistance of the lock-in amplifier and the capacitance of the photodiode resulted in a time constant which was less than 1 μs . The phase lag of the system was also experimentally studied by measuring the phase lag between the heating and the probe laser while heating a gold film of 0.5 μm thickness. The measured phase lag was found to be negligible in the 0-2 kHz frequency range, thus indicating that the system phase lag could be ignored in all measurements.

3. Theoretical Analysis

Consider the geometry in Fig. 2(a). Solid 1 occupies the region $0 < z < b_1$ and has a thickness $d_1 = b_1$, thermal diffusivity α_1 and thermal conductivity k_1 . Solid 2 occupies the region $b_1 < z < b_2$ with properties α_2 and k_2 and a thickness, $d_2 = b_2 - b_1$. It is assumed that the heating laser is focused to a circular spot of radius, $r = a$, and is absorbed on the top surface of solid 1. The heat conduction equations in cylindrical coordinates are

$$\frac{f^2 u_j}{fr^2} + \frac{1}{r} \frac{fu_j}{fr} + \frac{f^2 u_j}{fz^2} = \frac{1}{\alpha_j} \frac{fu_j}{ft}; \quad (j = 1, 2) \quad (2)$$

where u_j is the temperature in solid j . It is assumed that most of the heat flow occurs in the r and z directions in the solid and the heat loss to the surrounding air is negligible. The boundary conditions at $z = 0$ are

$$\begin{aligned} -k_1 \frac{fu_1}{fz} \Big|_{z=0} &= \frac{Q}{\pi a^2} e^{-i\alpha r} \quad \text{for } r \leq a \\ \frac{fu_1}{fz} \Big|_{z=0} &= 0 \quad \text{for } r > a \end{aligned} \quad (3)$$

where Q is the incident laser power absorbed on the top surface which is modulated at an angular frequency of $\omega = 2\pi f$. At $z = b_2$

$$\frac{fu_2}{fz} \Big|_{z=b_2} = 0 \quad (4)$$

The energy balance at the interface can be written as

$$k_1 \frac{fu_1}{fz} \Big|_{z=b_1} = k_2 \frac{fu_2}{fz} \Big|_{z=b_1} = h(u_2 - u_1) \Big|_{z=b_1} \quad (5)$$

Since the periodic steady state is of interest, the starting temperatures are not important and for convenience $u_j(r, z, 0) = 0$ for $j = 1, 2$. It must be noted that a laser beam usually has a Gaussian intensity distribution and does not provide a uniform flux as assumed in equation (3). However, one can think of the radius a as an effective radius obtained by averaging over the Gaussian distribution. The agreement between the predictions based on top-hat and Gaussian distributions are good in the high frequency range as illustrated in Fig. 5.

Details of the method to solve the governing equations in conjunction with the boundary conditions can be found in the appendix and also partly in Dryden et al. (1998). The solution for the temperature distribution in the two solids are given as

$$u_1(r, z, t) = \frac{Qe^{-i\alpha x}}{k_1 \pi a} \times \int_{\lambda=0}^{\infty} \left[\frac{1}{\eta_1} \left\{ -\sinh \eta_1 z + \cosh \eta_1 z \left[\frac{\cosh \eta_1 b_1}{\sinh \eta_1 b_1} - \frac{k_2 \eta_2}{k_1 \eta_1} \frac{\sinh \eta_2 (b_2 - b_1)}{\sinh \eta_1 b_1} \xi(\lambda, s) \right] \right\} \right]_{s=-i\omega} J_1(a\lambda) J_0(r\lambda) d\lambda \quad (6)$$

$$u_2(r, z, t) = \frac{Qe^{-i\alpha x}}{k_1 \pi a} \int_{\lambda=0}^{\infty} \left[\frac{\xi(\lambda, s)}{\eta_1} \cosh \eta_2 (b_2 - z) \right]_{s=-i\omega} J_1(a\lambda) J_0(r\lambda) d\lambda \quad (7)$$

where λ and s are the variables resulting from the Hankel and Laplace transforms, respectively, J_0 and J_1 are the zeroth and first order Bessel functions, respectively, and

$$\eta_j = \left(\lambda^2 + \frac{s}{\alpha_j} \right)^{1/2}$$

$$\xi(\lambda, s) = \left[\frac{\sinh \eta_1 b_1 \cosh \eta_2 (b_2 - b_1) + \frac{k_2 \eta_2}{k_1 \eta_1} \cosh \eta_1 b_1 \sinh \eta_2 (b_2 - b_1)}{+ \frac{k_2 \eta_2}{h} \sinh \eta_1 b_1 \sinh \eta_2 (b_2 - b_1)} \right]^{-1} \quad (8)$$

Since the measurements with the probe laser were made at $r = 0$ and $z = b_2$, these values can be used to simplify the integrand in equation (7). The phase lag at a given position either on the top or the bottom surface can be found from equations (7) and (8). For example, in the expression for u_2 , the integral in equation (7) is a complex number which can be written as

$$u_2(r, b_2, t) = |u_2| e^{-i(\alpha x - \phi)} \quad (9)$$

The angle ϕ is the phase lag with respect to the incident radiant flux. This quantity can be used for estimation of the contact conductance as well as the thermophysical properties of the materials.

To establish validity of the conductance measurement technique, it is necessary to compare the measured phase lag with theoretical predictions for a benchmark case. This case was selected to be that of a single material (with no interface) of known thickness and thermal properties. The temperature rise of the bottom surface, $z = b$, at $r = 0$ can be derived (see appendix) to be

$$u(0, b, t) = \frac{Qe^{-i\omega t}}{k\pi a} \int_{\lambda=0}^{\infty} \left[\frac{1}{\eta} \frac{1}{\sinh \eta b} \right]_{s=-i\omega} J_1(a\lambda) d\lambda \quad (10)$$

The integral in equation (10) was calculated numerically and the phase lag was estimated from this computation. The high-frequency limit of equation (10) can be derived analytically and is given as

$$u(0, b, t) = \frac{Q \exp \left[-b \sqrt{\frac{\pi f}{\alpha}} \right]}{\pi a^2 \sqrt{\pi f k \rho C}} \exp \left[-i \left(\omega t - \left(b \sqrt{\frac{\pi f}{\alpha}} + \frac{\pi}{4} \right) \right) \right] \quad (11)$$

Therefore, the phase lag in the high-frequency limit can be written as

$$\phi = b \sqrt{\frac{\pi f}{\alpha}} + \frac{\pi}{4} \quad (12)$$

The phase lag of $\pi/4$ in equation (12) results from the inherent phase difference between the heat flux and the temperature at any point. For the two-solid problem that involves contact resistance at the interface, the high-frequency limit of equation (7) can be written as

$$u_2(0, b_2, t) = \frac{2\sqrt{2}Q \exp \left[- \left(d_1 \sqrt{\frac{\pi f}{\alpha_1}} + d_2 \sqrt{\frac{\pi f}{\alpha_2}} \right) \right] \exp \left[-i \left(\omega t - \left(d_1 \sqrt{\frac{\pi f}{\alpha_1}} + d_2 \sqrt{\frac{\pi f}{\alpha_2}} + \frac{\pi}{4} \right) \right) \right]}{\pi a^2 \sqrt{\pi f (k\rho C)_1} \left[1 + \sqrt{\frac{(k\rho C)_2}{(k\rho C)_1}} + \frac{(1-i)\sqrt{\pi f (k\rho C)_2}}{h} \right]} \quad (13)$$

where $d_1 = b_1$ is the thickness of solid 1 and $d_2 = b_2 - b_1$ is the thickness of solid 2. The phase lag in the high-frequency limit can be written as

$$\phi = \chi + \tan^{-1} \left[\frac{\left(\frac{\sqrt{\pi f (k\rho C)_2}}{h} \right)}{1 + \sqrt{\frac{(k\rho C)_2}{(k\rho C)_1}} + \frac{\sqrt{\pi f (k\rho C)_2}}{h}} \right]; \quad \text{where } \chi = d_1 \sqrt{\frac{\pi f}{\alpha_1}} + d_2 \sqrt{\frac{\pi f}{\alpha_2}} + \frac{\pi}{4} \quad (14)$$

Hence, the thermal contact conductance, h , can be expressed in terms of phase lag as

$$h = \frac{\sqrt{\pi f (k\rho C)_2} [1 - \tan(\phi - \chi)]}{\left[1 + \sqrt{\frac{(k\rho C)_2}{(k\rho C)_1}} \right] \tan(\phi - \chi)} \quad (15)$$

Note in equation (14) that when $h \rightarrow \infty$, i.e. in the absence of an interface, the phase lag reduces to the expression in equation (12) except for the fact that the phase lag of the two materials is added. On the other hand, when $h \rightarrow 0$ the additional phase lag from the interface is $\tan^{-1}(1)$ which is $\pi/4$. Hence, the whole range of h corresponds to phase lag range $0 < \phi < \pi/4$. It is also worth noting that if the material subscripts 1 and 2 are switched, the expression in equation (15) remains unchanged.

In addition to estimating h from equation (15) it is also important to determine the percentage error in h due to error in phase measurement. To facilitate the estimation, the quantity $\mu = |(dh/d\phi)/h|$ can be calculated to be

$$\mu = \left| \frac{1}{h} \left(\frac{dh}{d\phi} \right) \right| = \left| \frac{\tan(\phi - \chi)}{\sin^2(\phi - \chi) [1 - \tan(\phi - \chi)]} \right| \quad (16)$$

The percentage error in the measured conductance can be expressed as $\Delta h/h = \mu \Delta \phi$ where $\Delta \phi$ is the error in phase measurement.

Figure 4 shows a series of plots of phase lag, ϕ , versus the non-dimensional frequency, $b\sqrt{\pi f/\alpha}$, for different values of the ratio, $2a/b$. If the thickness of the material remains constant, variation of $2a/b$ represents changing the spot size of the heating laser. On each graph, $\phi - b\sqrt{\pi f/\alpha}$ curves are plotted for different values of the ratio r/b at the bottom surface. Since $r = 0$ corresponds to the center of the heating laser spot, variation of r/b at the bottom surface attempts to simulate the effect of misalignment of the heating and the probe lasers. It can be clearly seen that if $2a/b < 2$, a slight misalignment of the heating and the probe lasers can lead to large variations in the measured ϕ . Hence, this case is very sensitive to the location of the probe laser and is susceptible to errors. For the range $2a/b > 4$, all the $\phi - b\sqrt{\pi f/\alpha}$ curves for different values of $r/b < 2$ coincide. This makes the dependence of ϕ on r/b negligible which is the preferable condition for conducting experiments. Since the probe laser beam radius was 0.2 mm and the sample thickness ranged from 0.2 mm to 0.5 mm, alignment of the probe laser with the heating laser was possible within $r/b < 2$. On the other hand, the probe laser measured the average temperature and phase lag over a region equal to the probe beam diameter. To ensure that the phase lag over this whole region was almost uniform, it was necessary to satisfy the condition $2a/b > 4$ as suggested by Fig. 4. Increase of the heating laser spot size reduces the incident heat flux and, therefore, can decrease the temperature oscillations below the detectable limit estimated by equation (1). Note that although the phase lag, ϕ , starts from zero at low frequencies, it asymptotes to the value $b\sqrt{\pi f/\alpha} + \pi/4$ for higher frequencies, i.e. for $b\sqrt{\pi f/\alpha} > 1.5$, as suggested by equation (12). For the experiments results described in the next section, this region of $b\sqrt{\pi f/\alpha}$ was found to be useful for comparing the predictions with measurements.

4. Results

4.1 Single Material To confirm the accuracy of this technique, it was first necessary to compare the results for a single sample of known thermal properties. Figure 5(a) shows the theoretical prediction and the measurements of the phase lag for a single crystal silicon sample with both surfaces polished. The thickness, b , of the sample was 0.225 mm and the p -doping level was $1.2 \times 10^{16} \text{ cm}^{-3}$. The theoretical prediction of the phase lag as a function of $b\sqrt{\pi f/\alpha}$ resulted in a single curve. To compare the measurements with the theory, it was necessary to guess the thermal diffusivity to normalize the experimental data in terms of the coordinate $b\sqrt{\pi f/\alpha}$. The same experimental data of phase lag is plotted in Fig. 5(a) for three selected values of α . For $b\sqrt{\pi f/\alpha} < 0.8$, there is large disagreement between the predictions and the measurements. It must be noted that $b\sqrt{\pi f/\alpha}$ can also be written as b/δ , where δ is the thermal penetration depth. The results suggest that when the penetration depth is larger than the material thickness, the predictions do not agree with the measurements. The reason for this is at present unclear, although it may be due to the assumption of insulating boundary conditions at the bottom surface. However, the agreement for $b\sqrt{\pi f/\alpha} > 0.8$ provides a range for using this technique.

The inset in Fig. 5(a) magnifies the results to show the effect of the chosen α on the comparison of the measurements with the theory. The region of $b\sqrt{\pi f/\alpha} > 1.5$ is intentionally chosen because, as indicated before, the phase lag varies as $b\sqrt{\pi f/\alpha} + \pi/4$. It can be seen that the best agreement occurs for $\alpha = (80 \pm 3) \times 10^{-6} \text{ m}^2/\text{s}$. The error margin in the estimation of α was obtained from the error bars in the phase measurements as shown in Fig. 5(a). Using the density and heat capacity of silicon to be 2330 kg/m^3 and 712 J/kg-K (Incropera and Dewitt, 1990), respectively, the thermal conductivity of the silicon sample can be estimated from the measured α to be $k = 132.7 \pm 5 \text{ W/m-K}$. Recent measurements have shown that the thermal conductivity of silicon with both p -doping concentration of $4 \times 10^{14} \text{ cm}^{-3}$ and n -doping concentration of 10^{18} cm^{-3} is 135.1 W/m-K at 300 K (Lee and Cahill, 1997). This is not only

within the error margin of the present measurements, the average values are within 2 percent of each other. The close agreement provides a benchmark test for the optical measurement technique.

Figure 5(b) shows the similar data set for an Al(6061 alloy) sample that was 0.223 mm thick. The inset shows that the best fit between the experiments and theory occurred for thermal diffusivity $\alpha = (73 \pm 3) \times 10^{-6} \text{ m}^2/\text{s}$. Using density $\rho = 2700 \text{ kg/m}^3$ and heat capacity $C = 896 \text{ J/kg-K}$ (Boyer et al., 1985), the thermal conductivity of the Al sample was found to be $176.6 \pm 7.3 \text{ W/m-K}$. The reported values of thermal diffusivity and conductivity of Al6061 are $74.4 \text{ m}^2/\text{s}$ and 180 W/m-K (Boyer et al., 1985), respectively, which are within the error margin of the present measurements and the average values are within 2 percent. The fact that the errors between reported and measured values are within 2 percent for both Si and Al samples suggests that the technique is quite accurate.

It is important to note that when the penetration depth is smaller than the material thickness, $b/\delta > 1$, the temperature oscillations at the bottom surface varies as $\exp(-b\sqrt{\pi f/\alpha})$ (see equation (11)). As the frequency is increased, the temperature oscillations decrease. The minimum detectable temperature, as estimated by equation (1), provides an upper limit to the frequency. This, for the results presented here, is typically in the range of 2-4 kHz. A small systematic deviation from the theoretical analysis in the high frequency limit may be due to a larger system phase lag. To make measurements in the high-frequency regime, i.e. $f > 500 \text{ Hz}$, it was impossible to use wire thermocouples since the smallest time constant of commercially available ones are typically on the order of 10 ms. It is for this reason that an optical temperature measurement technique was adopted. In the present work, the maximum frequency for reflectance thermometry was not limited by the sensor response time or the lock-in amplifier bandwidth (which was 100 kHz), but by the minimum detectable temperature as explained above.

4.2 Two Solids with Contact Conductance It is clear from equation (14) that the phase lag, ϕ , in the high-frequency limit can be plotted against the quantity $d_1\sqrt{\pi f/\alpha_1} + d_2\sqrt{\pi f/\alpha_2}$ since under the limiting condition of $h \rightarrow \infty$, the phase lag should vary as $d_1\sqrt{\pi f/\alpha_1} + d_2\sqrt{\pi f/\alpha_2} + \pi/4$. Figure 6 shows a such a plot for the Al-Si contact conductance measurements. The Al and Si samples were exactly the same as the ones used for single material measurements described in section 4.1, and the measured values of α_1 and α_2 were used for data analysis. The RMS roughness of the contacting surfaces of Al and Si samples were 8.58 μm and 3.2 nm, respectively. Under compressive load $F = 1000$ N the phase lag was measured over a wide frequency range and shown as filled circles in Fig. 6. The plot shows that for $d_1\sqrt{\pi f/\alpha_1} + d_2\sqrt{\pi f/\alpha_2} > 1.5$, the high-frequency behavior is observed. In this regime, equation (15) could be applied to estimate the contact conductance. The modulation frequency $f = 350$ Hz was chosen so that it fell in the high-frequency regime, and then the load was reduced to 80 N. It can be observed that the phase lag increased as the load was decreased. This is expected since the decrease in load results in a decrease of the real area of contact and thereby a reduction in thermal contact conductance. Also shown are the predictions for the phase lag as a function $d_1\sqrt{\pi f/\alpha_1} + d_2\sqrt{\pi f/\alpha_2}$ for variation of h over two orders of magnitude. Although one could try to fit the predictions to each data at different loads, the closed form solution in equation (15) provides a simple method to estimate the contact conductance from the measured phase lag in the high-frequency regime.

The estimated contact conductance data as a function of load and pressure, $P = F/A$, are shown in Fig. 7. Using the values of ϕ and χ from Fig. 6, the value of μ was calculated using equation (16) and found to vary between 6 and 9 rad^{-1} . Although the lock-in amplifier had an intrinsic phase error of about 10^{-5} radians, the actual phase error, $\Delta\phi$, measured during the experiments was typically about 10^{-2} radians. From the relation, $\Delta h/h = \mu\Delta\phi$, the percentage error in the estimated conductance varied between 6 and 9 percent. The phase error and the percentage conductance error for each value of load is shown in Figs. 6 and 7, respectively.

The inset in Fig. 7 shows the conductance-pressure data in a log-log plot. The plot indicates that the conductance varied with pressure as $h \propto P^{1.76}$. It should be noted that previous experimental studies have shown the load exponent to be in the range of 0.6-1.0 and theoretical studies have attempted to explain the origin of the exponent by various means. To the best of our knowledge, an exponent of 1.76 is higher than most observed and predicted values. The reason for this high value is at present unclear. However, it is important to note a significant difference between previous measurements and the present one. Previous measurements based on the technique illustrated in Fig. 1 have all measured the average contact conductance over the whole contact interface which were typically about 1-2 cm in characteristic length. These measurements averaged the conductance over local roughness or surface waviness. In contrast, the present technique measured the local contact conductance over a region that was typically about 2 mm in diameter whereas the samples were 1 cm x 1 cm in size. Hence, if the surface contained any waviness with wavelengths greater than or equal to 2 mm, then the present measurements would certainly be affected by it. If this is true, then these measurements cannot be compared with those of previous ones since the average conductance was not measured. In addition, it would be difficult to compare with previous theories since they are all based on a nominally flat surface. However, it is unclear at present whether local surface waviness led to such a high exponent value, but it is certainly a possibility. On the other hand, the non-uniform distribution of load across the sample could be another possibility.

5. Conclusions

This paper presents a fully non-contact optical technique for the measurement of thermal contact conductance of wafer-like thin solid samples. The technique is based on heating one exposed solid surface using a modulated high-power laser beam, and the simultaneous measurement of the corresponding temperature modulation on the other exposed solid surface by monitoring the reflectance of a low-power probe laser beam. Because the phase lag between the probe laser signal and the heating laser is independent of the optical properties of the solid and

the laser intensities, it was used to estimate the thermal contact conductance of the interface between the two solids.

A detailed theoretical analysis was developed to estimate the thermal contact conductance as well as the thermophysical properties of the solids from the measured phase lag as a function of the modulation frequency and thickness of the solids. The analysis showed that if the heating laser beam spot is small compared to the thickness of the solid, a slight misalignment between the heating and probe laser beams can lead to large errors in the measured phase lags. The analysis provided the conditions for robust measurement so that slight misalignments do not lead to changes in phase lags. Closed form solutions were also obtained in the high-frequency limit which provided a simple procedure to estimate thermophysical properties solids as well as the thermal contact conductance of interfaces.

As a benchmark for this technique, the phase lag was measured as a function of modulation frequency for a single crystal silicon wafer that was 0.225 mm thick. Although the low frequency data did not agree well with the theory, agreement was excellent in the high-frequency range, i.e., when the sample thickness was larger than the thermal penetration depth. Comparison of theory and measurements in the high-frequency range was used to estimate the thermal conductivity of the silicon sample, which was found to be within 2 percent of previously reported data. Measurements of thermal contact conductance as a function of pressure were successfully made for Al-Si samples that were each about 0.225 mm thick.

In conclusion, it is important to note the differences between the optical technique presented here and the traditional techniques that are widely used for measuring thermal contact conductance. Each data point in the dynamic optical technique requires about 1-2 minutes whereas it can take about 1 hour for the traditional techniques since they are based on steady state measurements. The traditional techniques require thick samples since thermocouples need to be inserted to measure temperature gradients in the solids. In contrast, the optical technique is

fully non-contact and can be used for thin solids samples. This is particularly suited for electronic packaging materials which are typically 0.1-5 mm thick. Previous steady state techniques need precise measurement of heat flux and temperature thereby requiring a well calibrated heater, a controlled steady-state cooling unit, and thermal insulation around the sample. In contrast, because the optical technique is based on phase lag data, temperature and heat flux need not be measured precisely. In addition, the solids do not have to be insulated. Finally, whereas the traditional techniques measure average thermal contact conductance between the two solids, the optical technique can measure local conductance to a resolution of about four times thickness of the solid. Hence, by moving the laser spot, variations of contact conductance induced by surface waviness, property variations, and interface voids can be measured.

Acknowledgments

This work was partly supported by a grant from Hitachi. Our thanks to Dr. Shigeki Hirasawa of Hitachi Mechanical Engineering Research Laboratory for his interest and support of this work. We take this opportunity to express our deepest gratitude and respect for late Prof. Kunio Hijikata who helped initiate this collaboration. GW and AM were supported by the US National Science Foundation through grant CTS-9796166. The work of F.W.Zok was supported by the Office of Naval Research under Award No. N00014-97-1-0394 (Contract Officer: Dr. Stephen G. Fishman).

References

- Boyer, H. E. and Gall, T. L., 1985, *Metals Handbook*, Am. Soc. Metals, 9th edn., Vol. 2, pp. 115-116.
- Cardona, M., 1969, "Modulation spectroscopy," in *Solid State Physics*, Suppl. 11, Seitz, F., Turnbull, D., and Ehrenreich, H., eds., Academic Press, New York.
- Childres, W. S. and Peterson, G. P., 1989, "Quantification of thermal contact conductance in electronic packages," *IEEE Trans. Components, Hybrids, & Manufacturing Technol.*, Vol. 12, pp. 717-723.
- Claeys, W., Dilhaire, S., Quintard, V. Dom, J. P., and Danto, Y., 1993, "Thermoreflectance optical test probe for the measurement of current-induced temperature changes in microelectronic components," *Quality & Reliability Eng. Int.*, Vol. 9, pp. 303-308.
- Cooper, M. G., Mikic, B. B., and Yovanovich, M. M., 1969, "Thermal contact conductance," *Int. J. Heat Mass Transfer*, Vol. 12, pp. 279-300.
- Dryden, J. R, McDonald, K. R., Majumdar, A., and Zok, F. W., 1998, "A photothermal technique for the determination of the thermal conductance of interfaces and cracks," submitted for journal publication.
- Epperlein, P. W., 1993, "Micro-temperature measurements on semiconductor laser mirrors by reflectance modulation: A newly developed technique for laser characterization," *Jpn. J. Appl. Phys.*, Vol. 32, pp. 5514-5522.
- Fletcher, L. S., 1988, "Recent developments on contact conductance heat transfer," *ASME JOURNAL OF HEAT TRANSFER*, Vol. 110, pp. 1059-1070.
- Incropera, F. P. and DeWitt, D. P., 1990, *Fundamentals of Heat and Mass Transfer*, 3rd edn., John Wiley, New York.
- Ju, Y. S. and Goodson, K. E., 1997, "Short-timescale thermal mapping of interconnects," *IEEE Proc. Int. Reliab. Phys. Symp.*, Denver, CO, pp. 320-324.
- Ju, Y. S. and Goodson, K. E., 1998, "Short-time-scale thermal mapping of microdevices using scanning thermoreflectance technique," *ASME JOURNAL OF HEAT TRANSFER*, Vol. 120, pp. 306-313.
- Kraus, A. D. and Bar-Cohen, A., 1983, *Thermal Analysis and Control of Electronic Equipment*, Hemisphere, New York.
- Lachapelle A., 1985, "Thermal analysis by photoacoustic phase measurements: Effect of sample thickness," *J. Appl. Phys.*, Vol. 57, pp. 5075-5077.

Lambert, M. A. and Fletcher, L. S., 1997, "Review of models for thermal contact conductance of metals," *J. Thermophysics and Heat Transfer*, Vol. 11, pp. 129-140.

Lee, S. M. and Cahill, D. G., 1997, "Heat transport in thin dielectric films," *J. Appl. Phys.*, Vol. 81, pp. 2590-2595.

Lepoutre, F., Fournier, D. and Boccara, A. C., 1985, "Nondestructive control of weldings using the mirage detection," *J. Appl. Phys.*, Vol. 57, pp. 1009-1015.

Leung, M., Hsieh, C. K., and Goswami, D. Y., 1998, "Prediction of thermal contact conductance in vacuum by statistical mechanics," *ASME JOURNAL OF HEAT TRANSFER*, Vol. 120, pp. 51-57.

Maddren, J. and Marschall, E., 1995, "Predicting thermal contact resistance at cryogenic temperatures for spacecraft applications," *J. Spacecraft and Rockets*, Vol. 32, pp. 469-474.

Majumdar, A. and Tien, C. L., 1991, "Fractal network model of contact conductance," *ASME JOURNAL OF HEAT TRANSFER*, Vol. 113, pp. 516-525.

Mikic, B. B., 1974, "Thermal contact conductance: theoretical considerations," *Int. J. Heat Mass Transfer*, Vol. 17, pp. 205-214.

Mohr, J. W., Seyed-Yagoobi, J., and Price, D. C., 1997, "Thermal contact conductance of a paper/elastomer interface," *ASME JOURNAL OF HEAT TRANSFER*, Vol. 119, pp. 363-366.

Nishino, K., Yamashita, S., and Torii, K., 1995, "Thermal contact conductance under low applied load in vacuum environment," *Experimental Thermal and Fluid Science*, Vol. 10, pp. 258-271.

Qiu, T. Q., Grigoropoulos, C. P., and Tien, C. L., 1993, "Novel technique for non-contact and microscale temperature measurements," *Experimental Heat Transfer*, Vol. 6, pp. 231-241.

Quintard, V., Deboy, G., Dilhaire, Lewis, D., Phan, T., and Claeys, W., 1996, "Laser beam thermography of circuits in the particular case of passivated semiconductors," *Microelectronic Engineering*, Vol. 31, pp. 291-298.

Rosei, R. and Lynch, D. W., 1972, "Thermomodulation spectra of Al, Au, and Cu," *Phys. Rev. B.*, Vol. 5, pp. 3883-3893.

Salgon, J. J., Robbe-Valloire, F., Blouet, J., and Bransier, J., 1997, "A mechanical and geometrical approach to thermal contact resistance," *Int. J. Heat Mass Transfer*, Vol. 40, pp. 1121-1129.

Scouler, W. J., 1967, "Temperature-modulated reflectance of gold from 2 to 10 eV," *Phys. Rev. Lett.*, Vol. 18, pp. 445-448.

Seyed-Yagoobi, J., Ng, K. H., Fletcher, L. S., 1992, "Thermal contact conductance of a bone-dry paper handsheet/metal interface," *ASME JOURNAL OF HEAT TRANSFER*, Vol. 114, pp. 326-330.

Tam, A. C. and Sontag H., 1986, "Measurement of air gap thickness underneath an opaque film by pulsed photothermal radiometry," *Appl. Phys. Lett.*, Vol. 49, pp. 1761-1763.

Williamson, M. and Majumdar, A., 1992, "Effect of surface deformations on contact conductance," *ASME JOURNAL OF HEAT TRANSFER*, Vol. 114, pp. 802-810.

Yovanovich, M. M., 1987, "Theory and applications of constriction and spreading resistance concepts for microelectronic thermal management," *Proceedings of the International Symposium on Cooling Technology for Electronic Equipment*, Honolulu, HI.

Appendix

Let $v_j(r, z, s)$ be the Laplace transform of $u_j(r, z, t)$ so that

$$v_j(r, z, s) = \int_{t=0}^{\infty} e^{-st} u_j(r, z, t) dt \quad (\text{A.1})$$

and let $w_j(\lambda, z, s)$ be the Hankel transform of $v_j(r, z, s)$ so that

$$w_j(\lambda, z, s) = \int_{r=0}^{\infty} v_j(r, z, s) r J_0(\lambda r) dr \quad (\text{A.2})$$

where J_0 is the Bessel function of zeroth order.

Laplace transform of equations (2) - (5)

$$\begin{aligned} \frac{\partial^2}{\partial r^2} \int_{t=0}^{\infty} u_j e^{-st} dt + \frac{1}{r} \frac{\partial}{\partial r} \int_{t=0}^{\infty} u_j e^{-st} dt + \frac{\partial^2}{\partial z^2} \int_{t=0}^{\infty} u_j e^{-st} dt - \frac{1}{\alpha_j} \int_{t=0}^{\infty} \frac{\partial u_j}{\partial t} e^{-st} dt &= 0 \\ \frac{\partial^2 v_j}{\partial r^2} + \frac{1}{r} \frac{\partial v_j}{\partial r} + \frac{\partial^2 v_j}{\partial z^2} - \frac{1}{\alpha_j} \left([u_j e^{-st}]_{t=0}^{\infty} + s \int_{t=0}^{\infty} u_j e^{-st} dt \right) &= 0 \\ \frac{\partial^2 v_j}{\partial r^2} + \frac{1}{r} \frac{\partial v_j}{\partial r} + \frac{\partial^2 v_j}{\partial z^2} - \frac{1}{\alpha_j} \left\{ (u_j(r, z, \infty) \cdot 0 - u_j(r, z, 0) \cdot 1) + s \int_{t=0}^{\infty} u_j e^{-st} dt \right\} &= 0 \\ \frac{\partial^2 v_j}{\partial r^2} + \frac{1}{r} \frac{\partial v_j}{\partial r} + \frac{\partial^2 v_j}{\partial z^2} - \frac{s}{\alpha_j} v_j &= 0 \end{aligned} \quad (\text{A.3})$$

$$\int_{t=0}^{\infty} k_1 \frac{\partial u_1}{\partial z} \Big|_{z=0} e^{-st} dt = k_1 \frac{\partial v_1}{\partial z} \Big|_{z=0} = -\frac{Q}{\pi a^2} \int_{t=0}^{\infty} e^{-i\omega t} e^{-st} dt = -\frac{Q}{\pi a^2} \frac{-1}{(s+i\omega)} \left[e^{-(s+i\omega)t} \right]_{t=0}^{\infty}$$

$$k_1 \frac{\partial v_1}{\partial z} = -\frac{Q}{\pi a^2} \frac{1}{(s+i\omega)} \quad r \leq a$$

$$\frac{\partial v_1}{\partial z} \Big|_{z=0} = 0 \quad r \geq a$$

$$\frac{\partial v_2}{\partial z} \Big|_{z=b_2} = 0 \quad (\text{A.4})$$

$$k_1 \frac{\partial v_1}{\partial z} \Big|_{z=b_1} = k_2 \frac{\partial v_2}{\partial z} \Big|_{z=b_1} = h(v_2 - v_1) \Big|_{z=b_1} \quad (\text{A.5})$$

Note that

$$r \frac{\partial^2 v_j}{\partial r^2} + \frac{\partial v_j}{\partial r} = \frac{\partial}{\partial r} \left(r \frac{\partial v_j}{\partial r} \right), \quad \lim_{x \rightarrow \infty} J_\nu(x) = 0, \quad \frac{d}{dr} J_0(\lambda r) = -\lambda J_1(\lambda r), \quad \frac{d}{dr} [r J_1(\lambda r)] = \lambda r J_0(\lambda r),$$

Hankel transforms of equations (A.3)-(A.5) are

$$\int_{r=0}^{\infty} \left(r \frac{\partial^2 v_j}{\partial r^2} + \frac{\partial v_j}{\partial r} \right) J_0(\lambda r) dr + \int_{r=0}^{\infty} \frac{\partial^2 v_j}{\partial z^2} r J_0(\lambda r) dr - \frac{s}{\alpha_j} \int_{r=0}^{\infty} v_j r J_0(\lambda r) dr = 0$$

$$\begin{aligned}
& \int_{r=0}^{\infty} \frac{\partial}{\partial r} \left(r \frac{\partial v_j}{\partial r} \right) J_0(\lambda r) dr + \frac{\partial^2}{\partial z^2} \int_{r=0}^{\infty} v_j r J_0(\lambda r) dr - \frac{s}{\alpha_j} \int_{r=0}^{\infty} v_j r J_0(\lambda r) dr = 0 \\
& \left[r \frac{\partial v_j}{\partial r} J_0(\lambda r) \right]_{r=0}^{\infty} - \int_{r=0}^{\infty} r \frac{\partial v_j}{\partial r} (-\lambda) J_1(\lambda r) dr + \frac{\partial^2 w_j}{\partial z^2} - \frac{s}{\alpha_j} w_j = 0 \\
& \lambda \int_{r=0}^{\infty} \frac{\partial v_j}{\partial r} r J_1(\lambda r) dr + \frac{\partial^2 w_j}{\partial z^2} - \frac{s}{\alpha_j} w_j = 0 \\
& \lambda \left[v_j r J_1(\lambda r) \right]_{r=0}^{\infty} - \lambda \int_{r=0}^{\infty} v_j \lambda r J_0(\lambda r) dr + \frac{\partial^2 w_j}{\partial z^2} - \frac{s}{\alpha_j} w_j = 0 \\
& -\lambda^2 w_j + \frac{\partial^2 w_j}{\partial z^2} - \frac{s}{\alpha_j} w_j = 0 \\
& \therefore \frac{\partial^2 w_j}{\partial z^2} - \left(\lambda^2 + \frac{s}{\alpha_j} \right) w_j = 0 \tag{A.6}
\end{aligned}$$

$$\begin{aligned}
\int_{r=0}^{\infty} \frac{\partial v_1}{\partial z} \bigg|_{z=0} r J_0(\lambda r) dr &= \frac{\partial w_1}{\partial z} \bigg|_{z=0} = \int_{r=0}^a \left[-\frac{Q}{k_1 \pi a} \frac{1}{(s+i\omega)} \right] r J_0(\lambda r) dr + \int_{r=a}^{\infty} 0 \times r J_0(\lambda r) dr \\
&= -\frac{Q}{k_1 \pi a^2} \frac{1}{(s+i\omega)} \int_{r=0}^a r J_0(\lambda r) dr = -\frac{Q}{k_1 \pi a^2} \frac{1}{(s+i\omega)} \left[\frac{r}{\lambda} J_1(\lambda r) \right]_{r=0}^a \\
&= -\frac{Q}{k_1 \pi a^2} \frac{1}{(s+i\omega)} \frac{a J_1(\lambda a)}{\lambda}
\end{aligned}$$

$$\begin{aligned}
& \therefore \int r J_0(\lambda r) dr = \frac{r}{\lambda} J_1(\lambda r) \\
& \frac{\partial w_1}{\partial z} \bigg|_{z=0} = -\frac{Q}{k_1 \pi a} \frac{1}{(s+i\omega)} \frac{J_1(\lambda a)}{\lambda} \tag{A.7}
\end{aligned}$$

$$\frac{\partial w_2}{\partial z} \bigg|_{z=b_2} = 0 \tag{A.8}$$

$$k_1 \frac{\partial w_1}{\partial z} \bigg|_{z=b_1} = k_2 \frac{\partial w_2}{\partial z} \bigg|_{z=b_1} = h(w_2 - w_1) \bigg|_{z=b_1} \tag{A.9}$$

Solution of the differential equation (A.6) can be written as

$$w_j = A_j \sinh \eta_j z + B_j \cosh \eta_j z \quad \eta_j = \left(\lambda^2 + \frac{s}{\alpha_j} \right)^{1/2} \tag{A.10}$$

Using the boundary condition at $z = b_2$, the solution for w_2 is

$$w_2 = C_2 \cosh \eta_2 (z - b_2) \tag{A.11}$$

Using the boundary conditions at $z = 0$ and $z = b_1$, the solution for w_1 is

$$w_1 = A_1 \sinh \eta_1 z + B_1 \cosh \eta_1 z \tag{A.12}$$

where

$$\begin{aligned} A_1 &= -\frac{Q}{k_1 \pi a} \frac{1}{(s + i\omega)} \psi(\lambda, s) \\ B_1 &= -A_1 \left[\frac{\cosh \eta_1 b_1}{\sinh \eta_1 b_1} - \frac{k_2 \eta_2}{k_1 \eta_1} \frac{\sinh \eta_2 (b_2 - b_1)}{\sinh \eta_1 b_1} \xi(\lambda, s) \right] \\ C_2 &= -A_1 \xi(\lambda, s) \end{aligned} \quad (\text{A.13})$$

and

$$\begin{aligned} \psi(\lambda, s) &= \frac{J_1(a\lambda)}{\eta_1 \lambda} \\ \xi(\lambda, s) &= \left[\sinh \eta_1 b_1 \cosh \eta_2 (b_2 - b_1) + \frac{k_2 \eta_2}{k_1 \eta_1} \cosh \eta_1 b_1 \sinh \eta_2 (b_2 - b_1) \right]^{-1} \\ &\quad + \frac{k_2 \eta_2}{h} \sinh \eta_1 b_1 \sinh \eta_2 (b_2 - b_1) \end{aligned} \quad (\text{A.14})$$

The steady periodic behavior of temperature in each material is given by inverting the Hankel and Laplace transforms. The Hankel inverse transform is given as

$$v_j(r, z, s) = \int_{\lambda=0}^{\infty} w_j(\lambda, z, s) \lambda J_0(r\lambda) d\lambda \quad (\text{A.15})$$

so one can find that

$$\begin{aligned} v_1(r, z, s) &= \frac{Q}{k_1 \pi a} \frac{1}{(s + i\omega)} \int_{\lambda=0}^{\infty} \psi(\lambda, s) \times \\ &\quad \left\{ -\sinh \eta_1 z + \cosh \eta_1 z \left[\frac{\cosh \eta_1 b_1}{\sinh \eta_1 b_1} - \frac{k_2 \eta_2}{k_1 \eta_1} \frac{\sinh \eta_2 (b_2 - b_1)}{\sinh \eta_1 b_1} \xi(\lambda, s) \right] \right\} \lambda J_0(r\lambda) d\lambda \end{aligned} \quad (\text{A.16})$$

$$v_2(r, z, s) = -\frac{Q}{k_1 \pi a} \frac{1}{(s + i\omega)} \int_{\lambda=0}^{\infty} \psi(\lambda, s) \xi(\lambda, s) \cosh \eta_2 (b_2 - z) \lambda J_0(r\lambda) d\lambda \quad (\text{A.17})$$

The Laplace inverse transform can be used to determine the temperature distribution. This follows as

$$\begin{aligned} u_1(r, z, t) &= \frac{Q e^{-i\omega t}}{k_1 \pi a} \times \\ &\quad \int_{\lambda=0}^{\infty} \left[\frac{1}{\eta_1} \left\{ -\sinh \eta_1 z + \cosh \eta_1 z \left[\frac{\cosh \eta_1 b_1}{\sinh \eta_1 b_1} - \frac{k_2 \eta_2}{k_1 \eta_1} \frac{\sinh \eta_2 (b_2 - b_1)}{\sinh \eta_1 b_1} \xi(\lambda, s) \right] \right\} \right]_{s=-i\omega} J_1(a\lambda) J_0(r\lambda) d\lambda \end{aligned} \quad (\text{A.18})$$

$$u_2(r, z, t) = \frac{Qe^{-i\omega t}}{k_1 \pi a} \int_{\lambda=0}^{\infty} \left[\frac{\xi(\lambda, s)}{\eta_1} \cosh \eta_2 (b_2 - z) \right]_{s=-i\omega} J_1(a\lambda) J_0(r\lambda) d\lambda \quad (\text{A.19})$$

The temperature rise on bottom surface of the specimen at $r = 0$ is

$$u_2(0, b_2, t) = \frac{Qe^{-i\omega t}}{k_1 \pi a} \int_{\lambda=0}^{\infty} \left[\frac{\xi(\lambda, s)}{\eta_1} \right]_{s=-i\omega} J_1(a\lambda) d\lambda \quad (\text{A.20})$$

Now consider a special case for determining the thermal diffusivity of a single material of thickness, b . The absence of an interface in this case can be represented as $1/h \rightarrow 0$. The temperature distribution in the single material can be derived to be

$$u(r, z, t) = \frac{Qe^{-i\omega t}}{k \pi a} \int_{\lambda=0}^{\infty} \left[\frac{1}{\eta} \frac{\cosh \eta (b - z)}{\sinh \eta b} \right]_{s=-i\omega} J_1(a\lambda) J_0(r\lambda) d\lambda \quad (\text{A.21})$$

Hence, the temperature rise on the bottom surface, $z = b$ at $r = 0$ is

$$u(0, b, t) = \frac{Qe^{-i\omega t}}{k \pi a} \int_{\lambda=0}^{\infty} \left[\frac{1}{\eta \sinh \eta b} \right]_{s=-i\omega} J_1(a\lambda) d\lambda \quad (\text{A.22})$$

Figure Captions

- Figure 1 Schematic diagram illustrating a traditional steady-state technique for measuring the thermal contact conductance between solids. The technique requires a thick solid sample since thermocouples need to be inserted. In addition, it requires a heating unit, a steady-state cooling unit, and thermal insulation since the heat flux needs to be precisely measured and should be uniform across the two solids.
- Figure 2 (a) Schematic diagram illustrating the principle of the dynamic optical technique; (b) the experimental set-up used for the measurements in this paper.
- Figure 3 A frequency spectrum of the photodiode signal showing the peak due to thermorefectance at the heating frequency of 350 Hz with a full-width half maximum of 0.2 Hz.
- Figure 4 Effect of the spot size of the heating laser on the top surface and misalignment of the measurement point on the bottom surface on the measured phase lag. The results indicate that if the heating laser spot diameter is more than four times the thickness of the solid then a slight misalignment in the probing point on the bottom leads to only small changes in phase lag.
- Figure 5 (a) Plot of the phase lag as a function of non-dimensional frequency for the silicon sample. The frequency is non-dimensionalized by choosing the value of thermal diffusivity which gives the closest fit to the predictions (solid line). The inset shows details of the effect of the thermal diffusivity on the agreement between theory and experiments. (b) Similar plot of phase lag versus non-dimensional frequency for the aluminum sample.
- Figure 6 Plot of phase lag as a function of non-dimensional frequency for the Al and Si sample in contact with each other. A frequency was carried out for the load of 1000 N. Then the frequency was fixed at 350 Hz and the load was reduced to 80 N while the phase lag was measured. The inset shows details of how the phase lag changes with load.
- Figure 7 Plot of thermal contact conductance estimated from the phase lag measurements as a function of compressive load for the Al-Si interface.

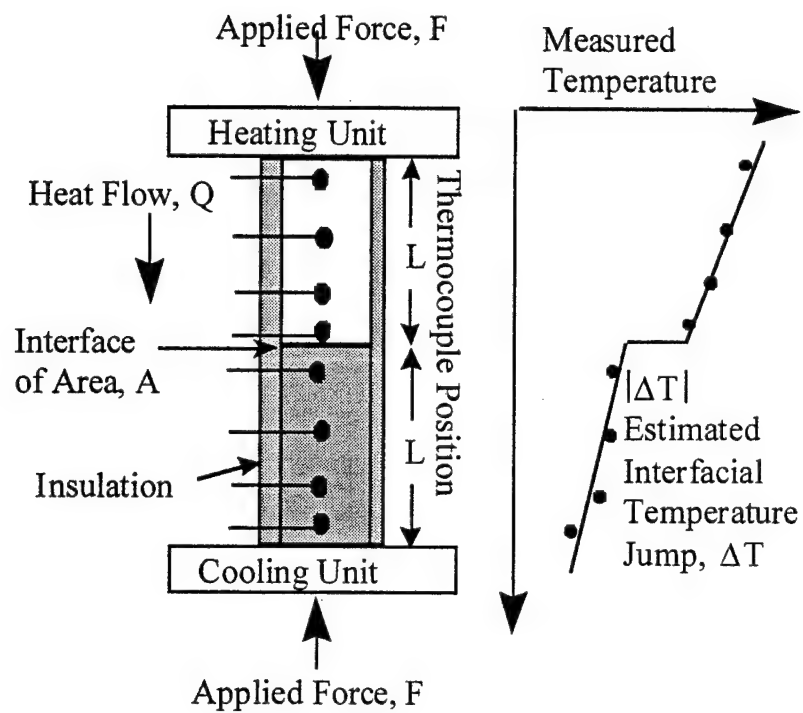


Figure 1

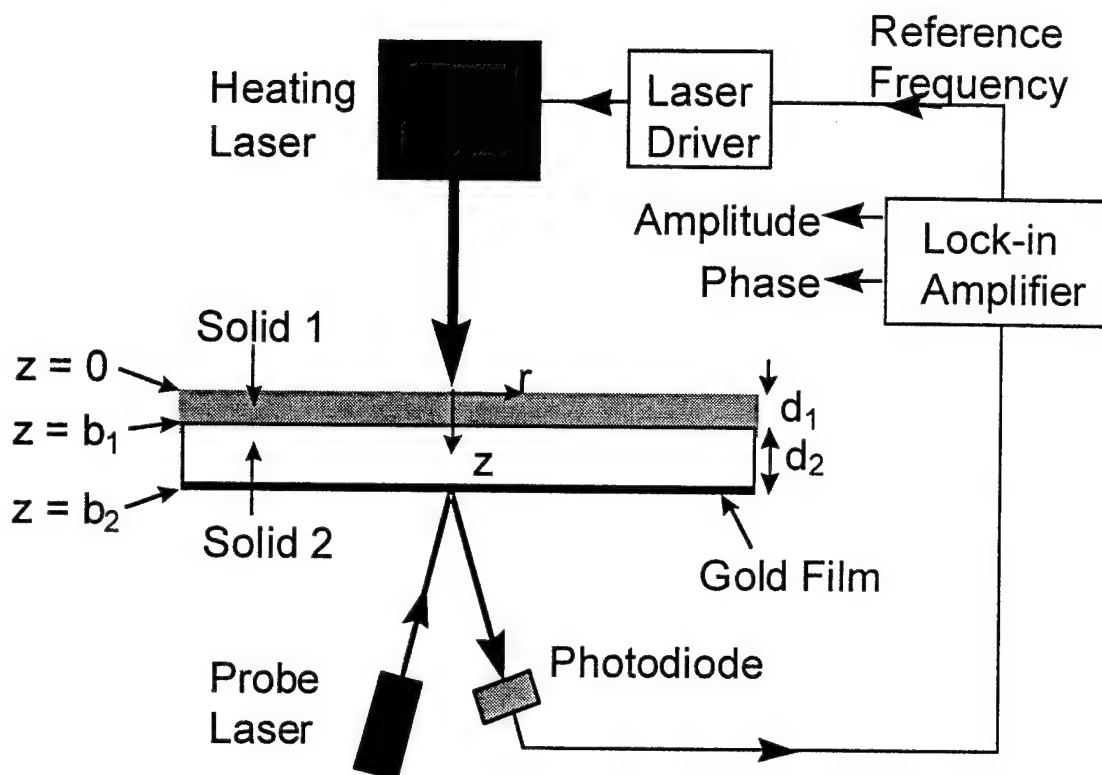


Figure 2 (a)

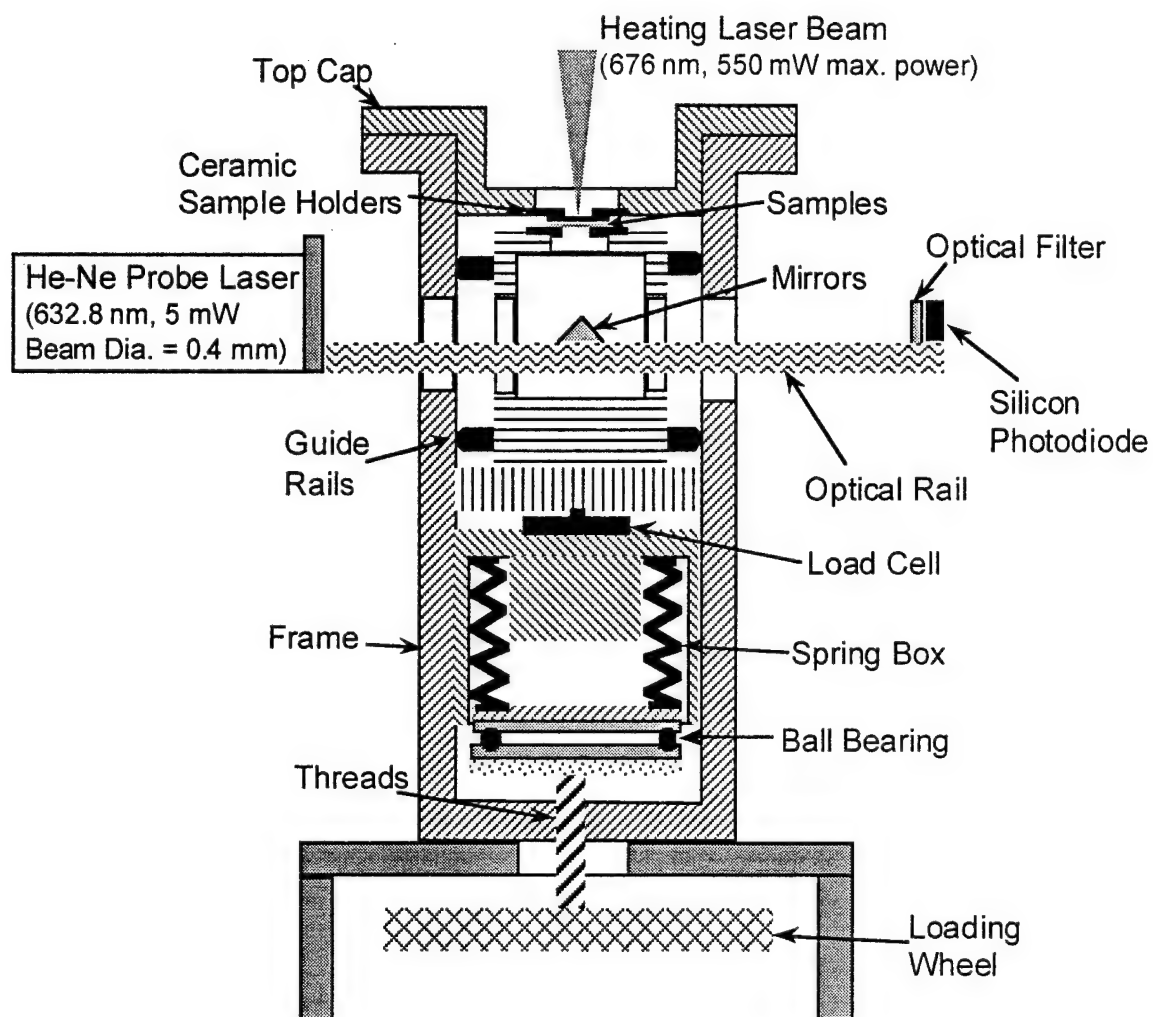


Figure 2 (b)

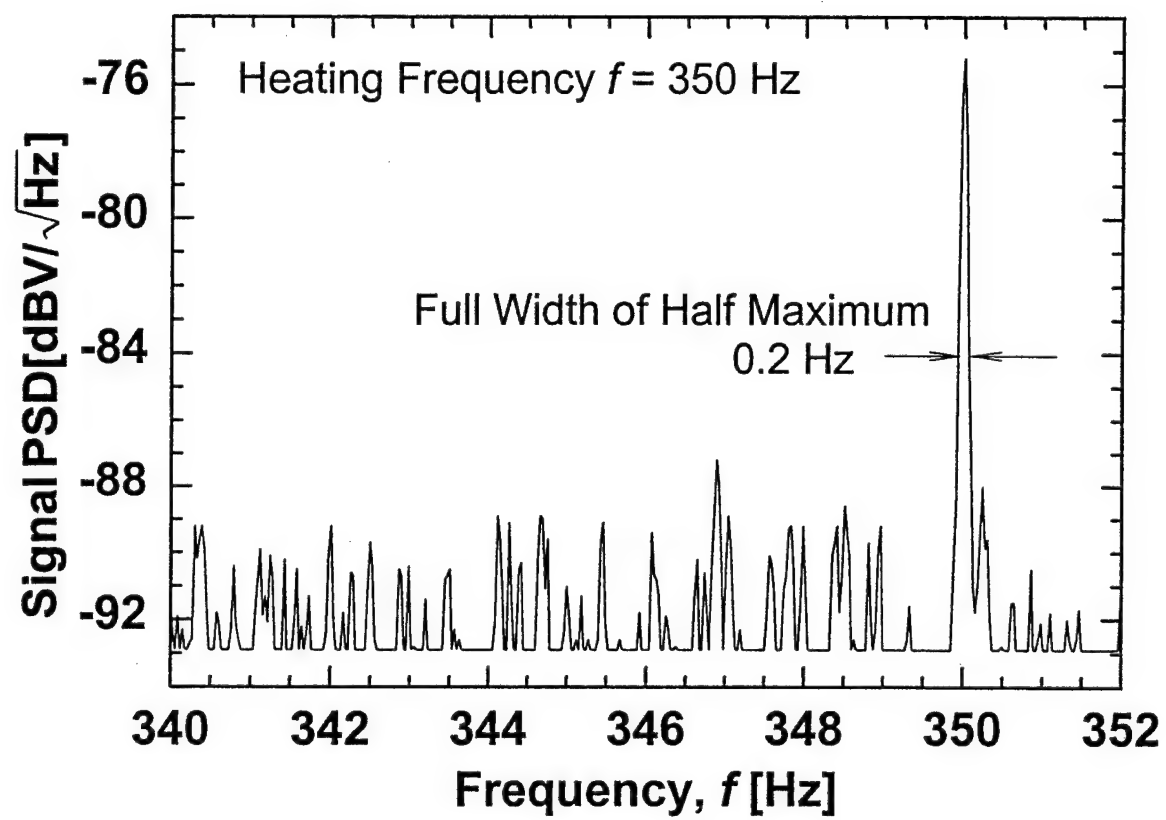


Figure 3

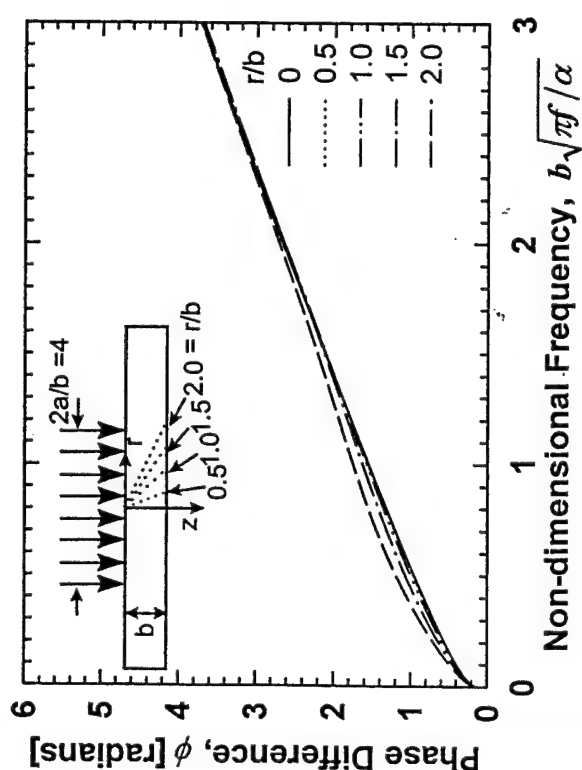
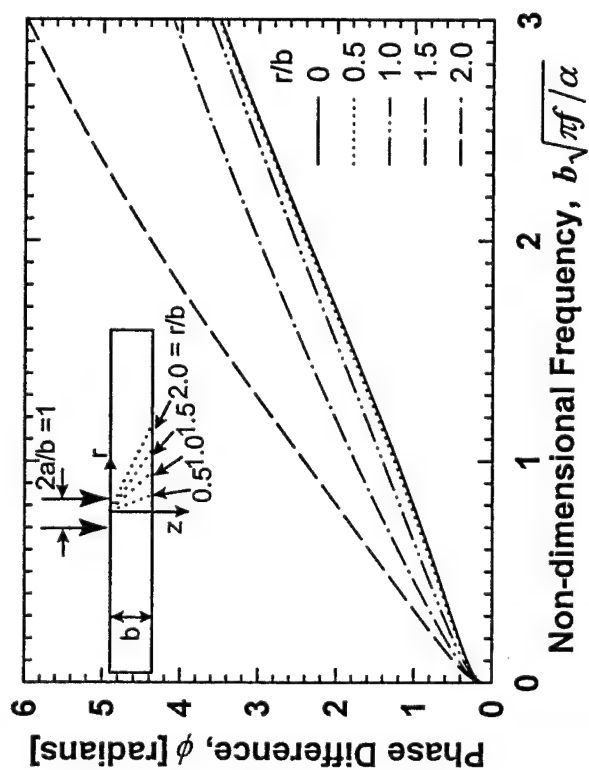
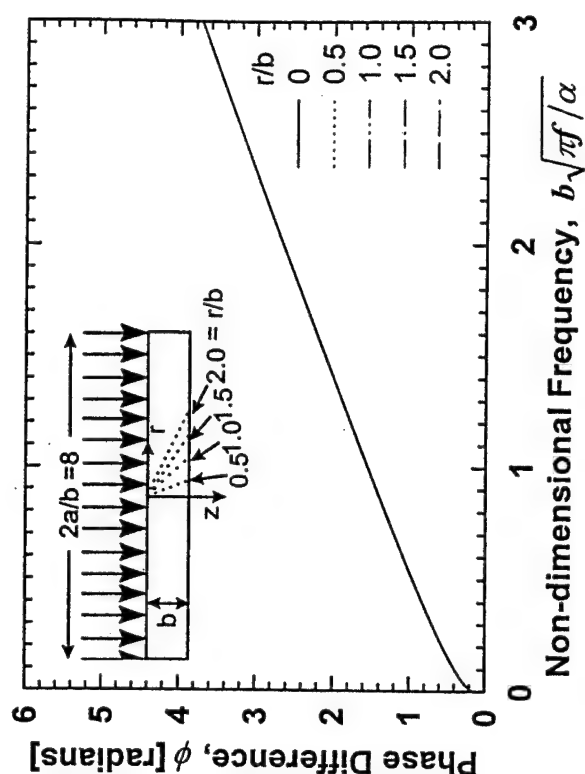
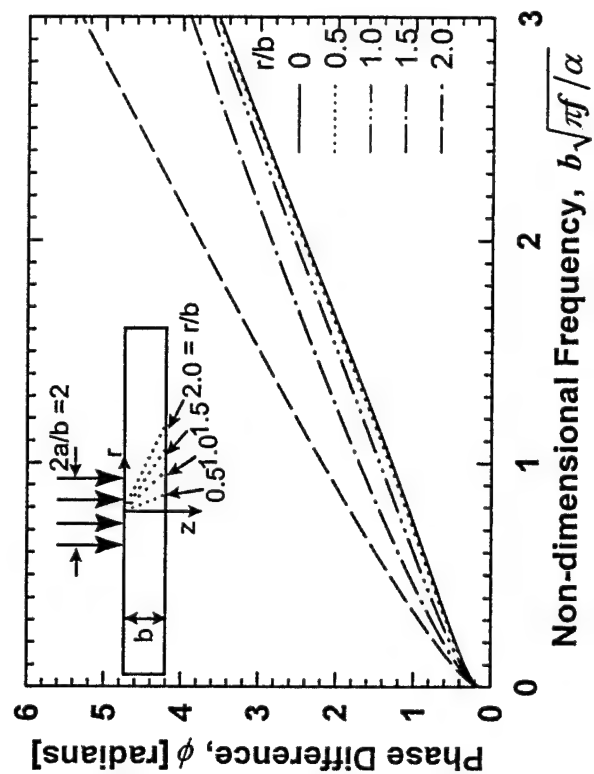


Figure 4

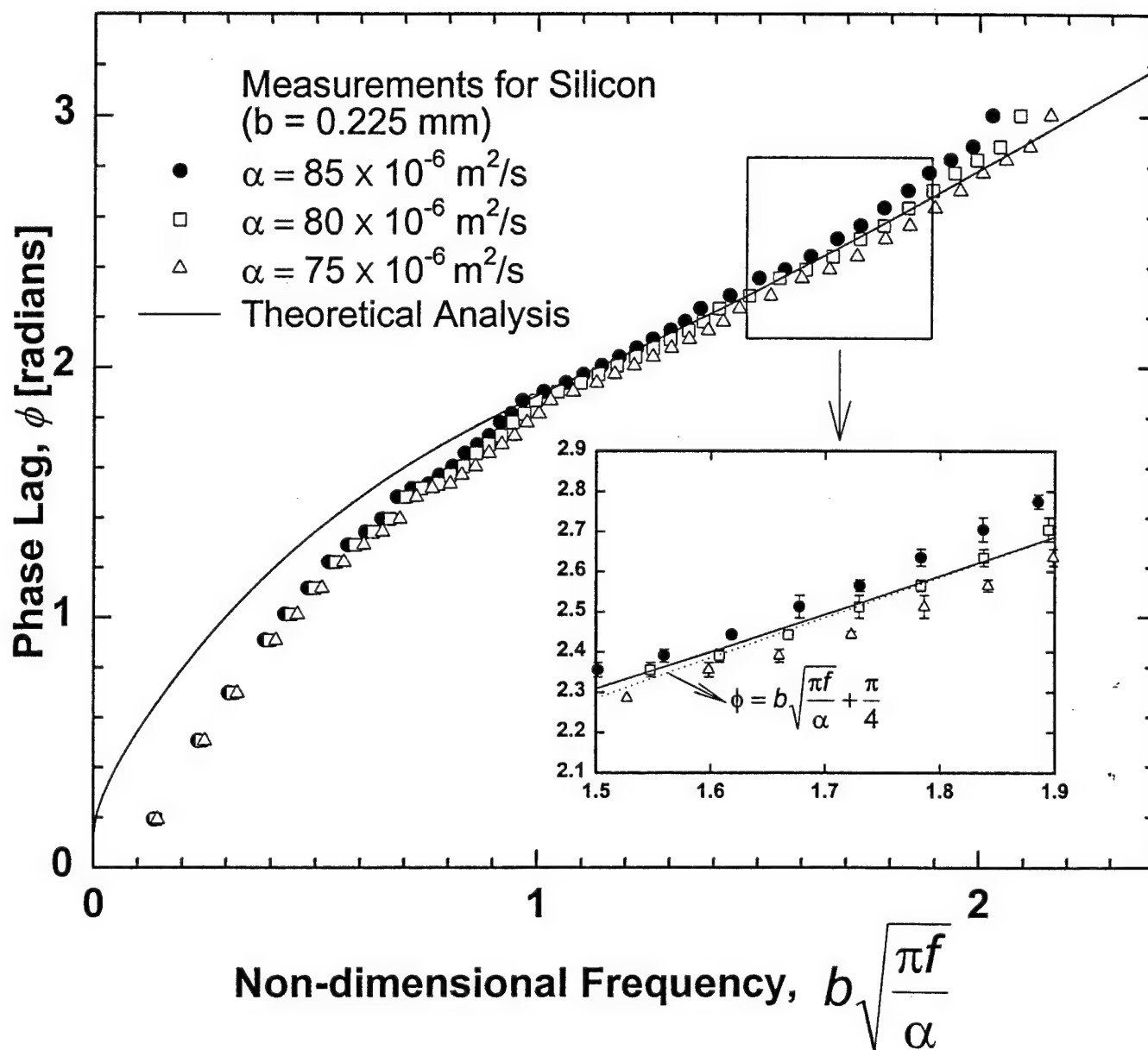


Figure 5(a)

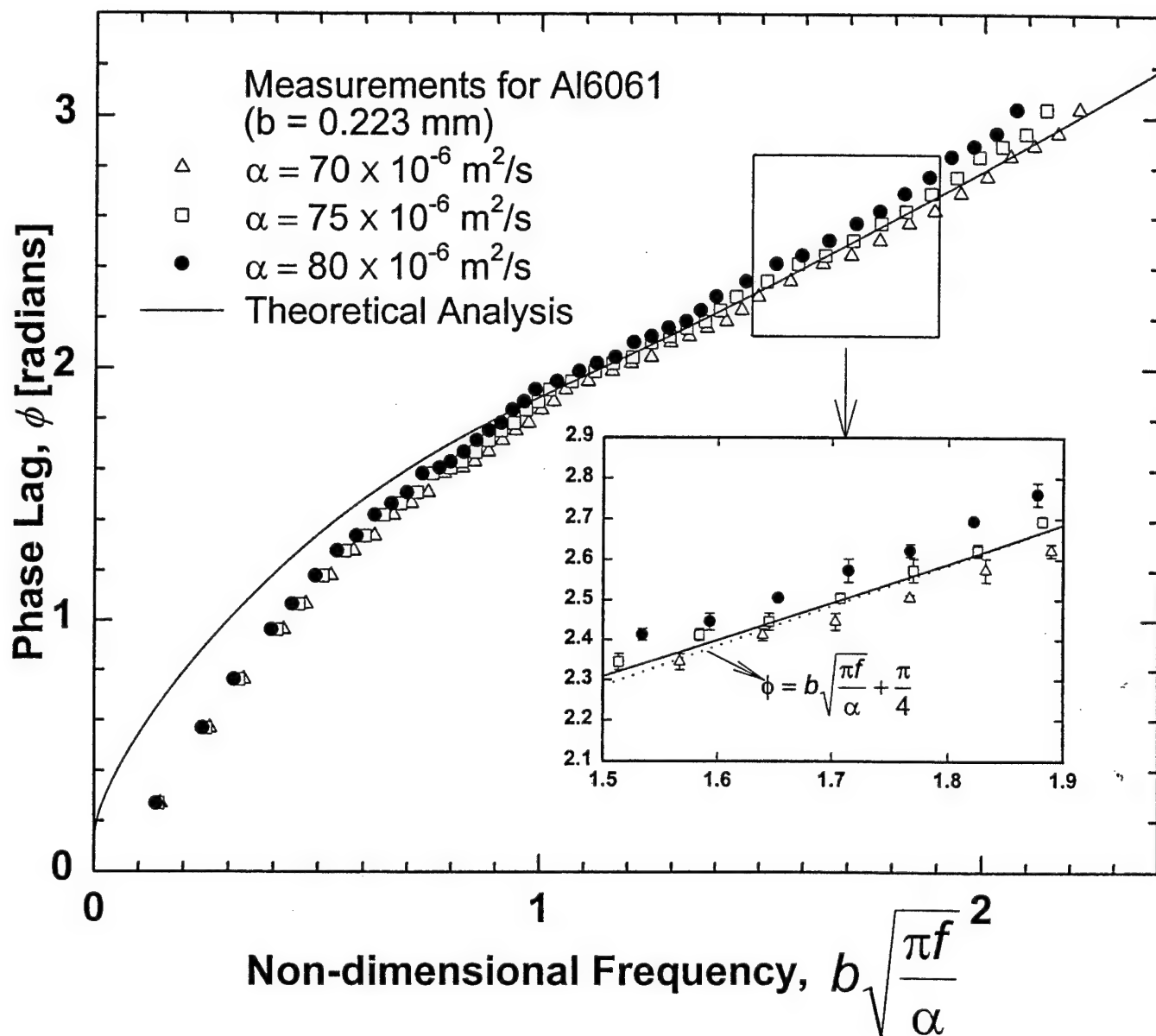


Figure 5(b)

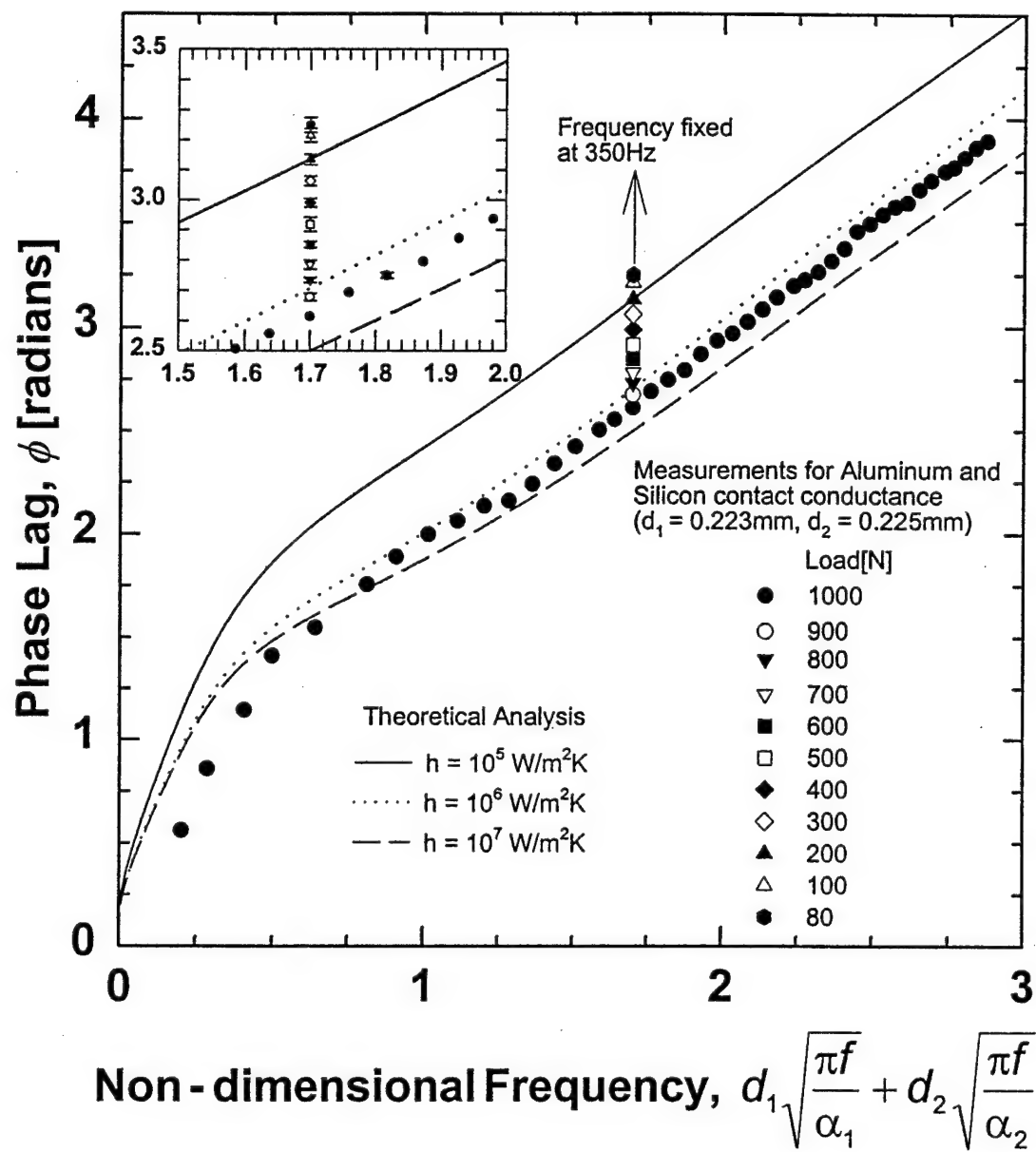


Figure 6

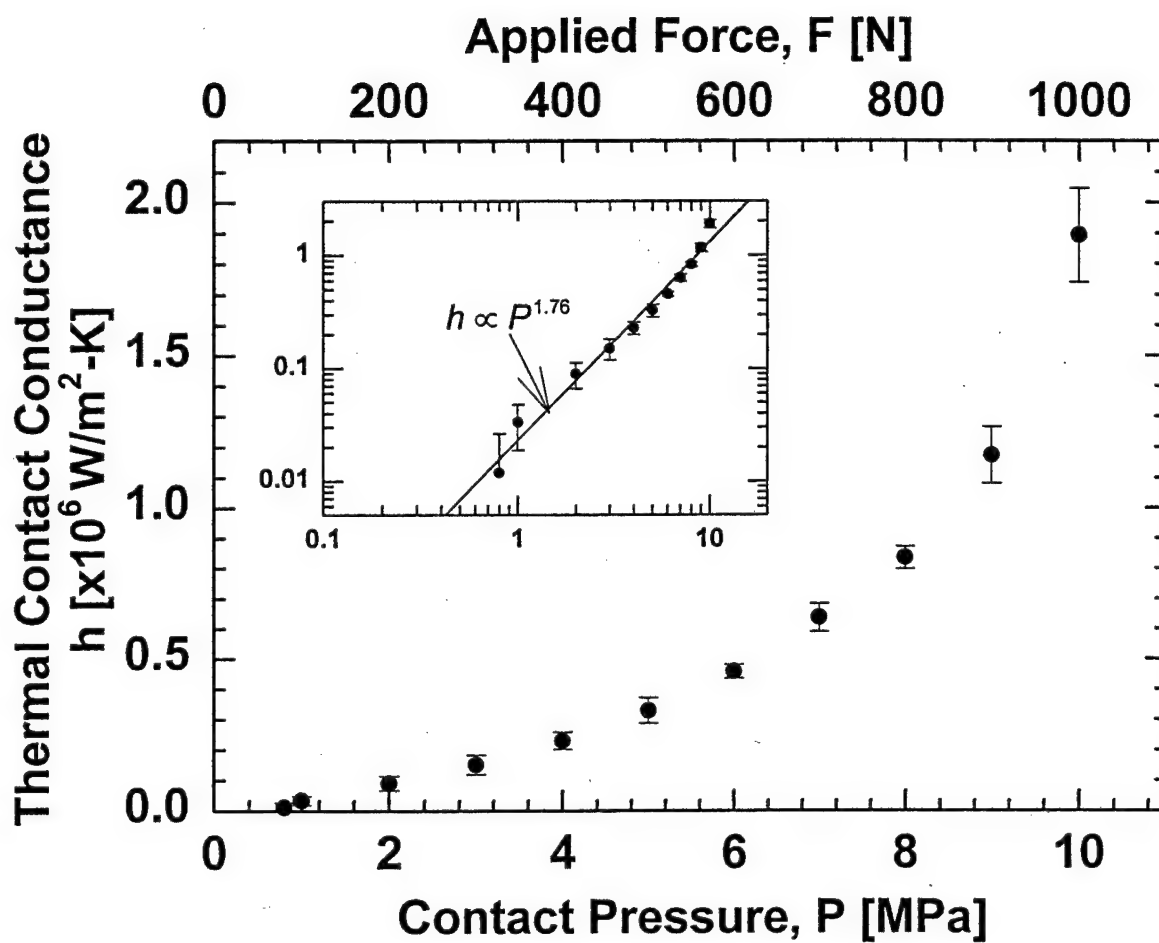


Figure 7



THERMAL CONDUCTANCE OF DELAMINATION CRACKS IN A FIBER REINFORCED CERAMIC COMPOSITE

K.R. McDonald, J.R. Dryden*, A. Majumdar† and F.W. Zok

Materials Department
University of California
Santa Barbara, California 93106

*Department of Mechanical & Materials Engineering
Faculty of Engineering Science
University of Western Ontario
London, Ontario N6A 5B9
Canada

†Department of Mechanical Engineering
6169 Etcheverry Hall
University of California
Berkeley, CA 94720

May, 1999

ABSTRACT

The thermal conductance of delamination cracks in a unidirectionally reinforced ceramic composite is investigated. A phase-sensitive photothermal technique is used to measure the crack conductance *in situ* under load. Special emphasis is placed on the effects of the local crack opening displacement. A model for the crack conductance that takes into account the contributions from both the air and the fibers within the crack is developed and compared with the measurements. Despite considerable scatter in the experimental data, the model adequately predicts the elevation in conductance associated with fiber bridging as well as the overall trend with crack opening displacement.

1. INTRODUCTION

Fiber-reinforced ceramic matrix composites (CMCs) are attractive for use in thermostructural applications because of their high damage tolerance, strength and creep resistance at elevated temperature. Additionally, for most hot structures, they must also exhibit high resistance to thermal shock, as manifest by a high thermal conductivity and a low thermal expansion coefficient. Indeed, the selection of SiC-based CMCs for gas turbine applications has been motivated in part by the high conductivity and low thermal expansion of SiC in relation to other structural ceramics. Despite the importance of these properties in failure of CMC structures, relatively little experimental information exists regarding thermal properties, especially following typical service conditions. In particular, since CMCs are likely to sustain microstructural damage, degradation in thermal properties is expected, potentially leading to elevation in thermal stresses and further damage and degradation in properties.

CMCs with 2D fiber architectures exhibit two characteristic damage modes.

(i) Under in-plane tensile loading, the damage involves multiple matrix cracks normal to the loading direction as well as interfacial debonding and sliding. The resulting nonlinear straining imparts high fracture toughness and low notch sensitivity. However, such cracks also impede heat flow in the plane containing the fibers, thereby reducing thermal conductivity [1-3]. (ii) Under out-of-plane loading, failure occurs by delamination through the matrix, with relatively little resistance coming from the fibers. Furthermore, delamination cracks present a particularly large impediment to heat flow in the through-thickness direction [4] because of the relatively small amounts of fiber bridging and hence the large crack opening displacements. The latter damage mode is the focus of the present paper. A study of the role of multiple matrix cracks on the in-plane properties is reported elsewhere [5].

To further motivate the current work, it is useful to consider the problem of a thin CMC plate containing a long delamination crack along the midplane and subject to a steady-state temperature difference, ΔT , between the two surfaces of the plate. The resulting energy release rate for the crack is given by [6]

$$\mathcal{G} = EA (\alpha \Delta T)^2 / 32(1+b)^2 \quad (1)$$

where E is the in-plane modulus, A is the plate thickness, and b is the Biot modulus, defined by $b \equiv Ah/k$, with h being the crack conductance (assumed to be uniform) and k the through-thickness thermal conductivity of the pristine composite. The maximum energy release rate is obtained when the crack is perfectly insulating ($h = 0$), whereupon $b = 0$ and $\mathcal{G} \equiv \mathcal{G}_0 = EA (\alpha \Delta T)^2 / 32$. The energy release rate diminishes rapidly with increasing crack conductance, especially for $b \gtrsim 1$. For instance, with $b = 2$, the energy release rate is reduced by almost an order of

magnitude. Knowledge of the typical values of h , and hence b , are crucial for identifying the thermal loading conditions under which delamination is expected to occur.

This paper examines the thermal conductance of delamination cracks in a relatively simple unidirectional CMC. A photothermal technique that allows *in-situ* measurement of the crack conductance under load is described and demonstrated. Experiments are performed to determine the variation in crack conductance, h , with crack opening displacement, δ . A rudimentary model for the crack conductance law, $h(\delta)$, is developed. An assessment of the model is made through comparisons with the measurements of $h(\delta)$ coupled with auxiliary measurements to determine the nature and extent of fiber bridging during delamination.

The paper is organized in the following way. Section 2 describes the technique and the crack conductance measurements. The analysis used for interpreting the measurements is based on a standard heat flow analysis, with the main theoretical results being summarized in the Appendix. A key conclusion from these measurements is that the crack conductance lies above the level predicted on the basis of air conduction alone, especially when the crack opening displacement is small ($\lesssim 50 \mu\text{m}$). The inference is that the conductance is enhanced by fibers that bridge the delamination crack. A model for the crack conductance that takes into account the contributions from both the air and the fibers within the crack is presented in Section 3. The key unknown properties in the model are the angle of inclination of the fibers with respect to the matrix crack plane and the volume fraction of fibers contained within the crack. Measurements are made to determine these parameters and subsequently make an assessment of the predictive capability of the model, also presented in Section 3.

2. PHOTOTHERMAL MEASUREMENTS

2.1 Background and Theory

Measurements of thermal conductance and thermal diffusivity were made using a phase-sensitive photothermal technique. The technique utilizes periodic heating at one point on the specimen surface and measurement of the phase shift, ϕ , of the temperature with respect to the heat input at some other point. The pertinent theoretical heat flow analysis for plate specimens is presented partially by Ohson et al. [7] and summarized in the Appendix.

The key parameters governing ϕ are: the distance, r , between the heat source and the thermocouple; the heating frequency, f ; the thermal diffusivity, α ; the volumetric heat capacity, c ; the thermal conductivity, $k = \alpha c$; the specimen thickness, A ; and the crack conductance, h . The effect of crack conductance is conveniently expressed in the form of a nondimensional resistance parameter, $\rho \equiv h/2kA = 1/2b$. Some representative numerical results are shown in Fig. 1.

To illustrate the main effects of these parameters on ϕ , two limiting cases that yield straightforward analytical solutions are considered. (i) When the specimen thickness, A , is large compared with the distance, r , and there is no crack present, the phase lag along the top surface reduces to

$$\phi = \beta r = r \sqrt{\pi f / \alpha} \quad (2)$$

where β is the wave number. Consequently, the thermal diffusivity can be determined from a series of phase lag measurements, either at fixed distance r and with varying frequency, f , or, alternatively, at fixed f and with varying r . A similar result applies to the point on the bottom surface directly across from the heat source; that is, $\phi = \beta A$ when $\beta A > 1$ (dashed line in Fig. 1(b)). (ii) When both the crack conductance and the frequency are sufficiently high, characterized by $\rho \ll 1$ and

$\beta A > 1$, the phase lag on the bottom surface directly across from the heat source approaches [7]

$$\phi = \beta A + \arctan \left[\frac{\rho \beta A}{1 + \rho \beta A} \right] \approx \beta A (1 + \rho) \quad (3)$$

Thus, the *additional* phase lag due to the crack, given by the difference between Eqns. (2) and (3), is

$$\Delta \phi_c \approx \rho \beta A = \frac{c \sqrt{\pi f \alpha}}{2h} \quad (4)$$

This result illustrates how, for the prescribed range of values of ρ and βA , the crack conductance h can be determined from a series of phase lag measurements before and after cracking coupled with measurements of α and c . In the present study, such measurements are made over a broader range of ρ and βA values; consequently, the experimental data are fit by the complete solutions from the heat flow analysis (shown in the Appendix) in order to determine crack conductance.

2.2 Implementation of Photothermal Technique

The apparatus used for the experiments is shown in Fig. 2. It comprises a focused 0.5W diode laser, mounted on a precision x-y-z translation stage. The power to the laser is modulated sinusoidally using a lock-in amplifier. A specimen is held in place beneath the laser, either simply-supported by pins at the edges or in a bend fixture. The temperature is measured at prescribed locations using fine Type T thermocouples, affixed to the specimen surface by colloidal silver paint. The signal from the thermocouple is input into the lock-in amplifier, and, upon comparison with the input signal to the laser, the phase shift, ϕ , is obtained.

2.3 Materials and Measurement Procedures

Experimental measurements were made on a unidirectional composite comprising a magnesium aluminosilicate (MAS) matrix and 36 vol% of ceramic grade Nicalon fibers. The thermal diffusivity of the pristine material was measured both parallel and perpendicular to the fiber direction. This was done by mounting a thermocouple on the surface of a plate and performing a series of phase lag measurements at varying distances from the heating source along the two principal directions. To mitigate the effects of the thermal resistance of the thermocouple itself, all measurements and subsequent analysis were based on the *difference* in phase lag relative to a reference measurement. For instance, in determining the pristine diffusivity, the measured phase lag, $\phi(r)$, was subtracted from the value obtained at the location nearest to the thermocouple, $\phi_0(r_0)$, yielding a difference $\Delta\phi(\Delta r) = \phi(r) - \phi_0(r_0)$ where $\Delta r = r - r_0$. In this way, the phase lag associated with the thermocouple is removed and the resultant measurement becomes a function of only the thermal properties and the geometry of the system. The diffusivities were then obtained by fitting the experimental data with the theoretical analysis presented in the Appendix.

The through-thickness diffusivity was measured by Holometrix using the laser flash method [8]. Because of the transverse isotropy of the composite, the through-thickness diffusivity is expected to be the same as the in-plane diffusivity transverse to the fibers. Comparisons between the two measurements were used as a validation of the present experimental technique. The volumetric heat capacity (which is needed for the determination of the crack conductance) was also measured by Holometrix using the same laser flash method.

Measurements of the thermal conductances of delamination cracks were obtained using the specimen and loading configuration shown in Fig. 3. Long

rectangular specimens were cut from the composite plate parallel to the fiber direction. The specimens were notched at the center, transverse to the fibers, to a depth of 1/2 of the width. One side surface of each specimen was then polished to a 1 μ m finish to facilitate measurement of crack opening displacements.

Thermocouples were attached at several locations along the bottom surface. The specimens were inserted into a four-point bending fixture, mounted directly beneath the laser (Fig. 3). Prior to loading, a series of through-thickness phase lag measurements were made at each thermocouple location over the frequency range, $f = 0.05$ -1.5 Hz. Additionally, the polished side surface was replicated using cellulose acetate tape.

Upon loading a specimen, a delamination crack initiated at the notch root and propagated along the specimen length (parallel to the fibers). Once the crack tip had proceeded beyond 3 or 4 of the thermocouples, the test was interrupted and an additional set of phase lag measurements was made at each thermocouple location. The differences in the phase lag, $\Delta\phi_c$, before and after cracking were used to determine the local crack conductance (above the thermocouple location), using the analysis in the Appendix. The polished side surface was again replicated and used for measurement of crack opening displacements, following the procedure described below. All phase lag measurements and surface replicas were taken under load at a fixed crack length. After the measurements were completed, the load was increased, causing additional crack growth and further opening of the crack. The phase lag measurements and surface replication were again repeated.

The local crack opening at each measurement location was determined through comparison of the surface replicas taken before and after cracking. For this purpose, well-defined surface features were selected on either side of the crack and the separation distance between them was measured in an optical microscope. These distances were then compared to those of the same features on replicas taken prior

to cracking, the difference being the crack opening displacement. (The crack opening displacement could not be measured directly from the crack edges because of inconsistent edge resolution on the replicas.) Figure 4 shows a typical set of replicas from the same region under increasing crack opening displacement. The fidelity of the replication technique was assessed in a few cases by comparing the surface replica with the corresponding region of the specimen surface viewed directly in an optical microscope. The two imaging methods yielded the same values for crack opening displacement.

2.4 Diffusivity and Conductance Measurements

The phase lag measurements made on the pristine composites in the longitudinal and transverse orientations are plotted in Fig. 5. The solid lines are based on calculations that give the best fit to the data (Appendix), using the thermal diffusivity, α , as a fitting parameter. The average results of the fitting procedure, obtained from 3-4 sets of measurements in each direction, are: $\alpha_T = 1.08 \times 10^{-6} \text{ m}^2/\text{s}$ and $\alpha_L = 1.48 \times 10^{-6} \text{ m}^2/\text{s}$. The variations between measurements at various locations on the plate were typically $< 10\%$. Evidently, the degree of anisotropy in diffusivity is rather small: $\alpha_L/\alpha_T \approx 1.4$.

The through-thickness diffusivity, measured by the laser flash method, is $1.04 \times 10^{-6} \text{ m}^2/\text{s}$, with an uncertainty of 5%. As expected, the through-thickness and in-plane transverse diffusivities are essentially the same, the difference ($\approx 4\%$) being less than the uncertainty in the respective measurements. The volumetric heat capacity was found to be $c = 704 \text{ J/kg K}$.

Figure 6 shows representative results of the phase lag measurements across the cracked specimens for four different values of crack opening displacement. The results are presented in terms of the phase lag difference, $\Delta\phi_c$, associated with the crack. The results demonstrate qualitatively that the thermal resistance and hence

the phase lag increase with increasing δ . The solid lines in the figure show the calculated results (Appendix), using the crack conductance h as a fitting parameter. The two dashed lines adjacent to each solid line represent calculations for conductance values that differ by $\pm 20\%$ of the best-fit value. The latter lines provide an indication of the sensitivity of $\Delta\phi_c$ to h .

The crack conductance values obtained from all measurements are plotted against δ in Fig. 7. Despite the scatter in the results (varying by as much as a factor of 3 at a fixed δ), the conductance clearly diminishes with increasing δ , by almost two orders of magnitude over the range $4\mu\text{m} \leq \delta \leq 150\mu\text{m}$. At the simplest level, this trend might be rationalized on the basis of the thermal resistance of the air contained within the crack, whereupon the conductance is predicted to be $h = k_a/\delta$, with k_a being the thermal conductivity of air (0.026 W/mK). This prediction is also shown on Fig. 7. It appears to predict the correct general trend in h with δ , but underestimates the average values of the measurements, especially at low values of δ . The latter discrepancy is believed to be associated with the presence of bridging fibers spanning the crack faces, an example of which is shown in Fig. 8. Since the conductivity of the fibers is about two orders of magnitude greater than that of air, even small amounts of fiber bridging are expected to have a large effect on the crack conductance. Indeed, the subsequent analysis and measurements confirm that the fibers can enhance the conductance by almost a factor of 10 for low values of δ . Furthermore, it is demonstrated that the correlation between the prediction ($h = k_a/\delta$) and the measurements is somewhat fortuitous, a consequence of δ being underestimated by the surface replication technique. More realistic estimates of the crack opening displacement yield lower values for the air contribution to the conductance, the inference being that the fiber contribution is higher than the value obtained by comparing the experimental measurements with the preceding prediction.

3. EFFECTS OF FIBER BRIDGING ON CRACK CONDUCTANCE

3.1 A Model for Crack Conductance

The conductance of a delamination crack can be partitioned into two components: one due to the air and the second due to bridging fibers. It is proposed that the combined effects can be represented by a series of resistors (analogous to that used in electrical circuits), as shown in Fig. 9. In this analog, the fiber is represented by two resistors connected in series. The first is associated with the constriction resistance at the point at which the fiber emerges from the composite. In general, this resistance can be expressed as [3, 9-11]

$$R_c = g_1 r / k_f \quad (5)$$

where r is the fiber radius, k_f is the fiber conductivity, and g_1 is a nondimensional function that accounts for the local geometry, the interface conductance, and the conductivity ratio, k_m/k_f , with k_m being the matrix conductivity. The second is due to the thermal resistance of the fiber itself, given by

$$R_f = g_2 \ell / k_f \quad (6)$$

where ℓ is the length of the bridging segment of the fiber and g_2 is another nondimensional function. If the fiber is inclined at an angle θ to the matrix crack plane, then the fiber length is $\ell = \bar{\delta} / \sin \theta$, with $\bar{\delta}$ being the effective crack opening displacement (defined below) and the resistance becomes

$$R_f = \frac{g_2 \bar{\delta}}{k_f \sin \theta} \quad (7)$$

The contribution from air conduction is represented by a third resistor, connected in parallel with the other two, with a resistance

$$R_a = g_3 \bar{\delta} / k_a \quad (8)$$

where g_3 is yet another nondimensional function. Upon combining these resistances and weighting the fiber and air contributions by their respective volume fractions within the crack, V_f^c and $1-V_f^c$, the crack conductance becomes

$$h = V_f^c \left[g_1 \frac{r}{k_f} + \frac{g_2 \bar{\delta}}{k_f \sin \theta} \right]^{-1} + (1 - V_f^c) \frac{k_a}{g_3 \bar{\delta}} \quad (9)$$

The values of the function g_i are presently unknown. However, previous studies on the thermal resistance associated with asperity contacts [9-11] and with bridging fibers oriented normal to the crack plane [3] indicate that the functions are not very different from unity, provided the fraction of solid contacts along the crack (V_f^c in the present case) is small.

3.2 Measurement of Bridging Parameters

An assessment of Eqn. 9 was made by measuring the relevant bridging parameters and subsequently comparing the predicted conductances with the measured values. The conductivities are well known: $k_f = 1.6$ W/mK [12, 13] and $k_a = 0.026$ W/mK [14]. Furthermore, the average fiber radius is $r = 7.5 \mu\text{m}$. It remains to determine V_f^c and θ . These parameters were measured using the following techniques.

Following completion of the crack conductance measurements and while the specimen was still under load, the delamination crack was impregnated with "super glue" in order to lock the bridging fibers in place and keep the crack open. The specimen was then unloaded, cut in half along the notch plane, and the two halves

mounted in epoxy. One of the two halves was polished along a plane parallel to the side surface of the specimen and used for measuring the fiber angle, θ . This was done by focusing onto the bridging fibers slightly below the sectioning plane in an optical microscope. The angles were measured from optical micrographs of the fibers, such as the one shown in Fig. 8. The fiber angle measurements are compiled in Fig. 10(a). Evidently there is considerable scatter, with the angles varying from ~ 2 - 20° . Furthermore, there is no apparent effect of the crack opening displacement. The average value is $\approx 8^\circ$ and the standard deviation $\approx 4^\circ$.

The other half of the specimen was ground and polished along a plane parallel to the initial notch plane. In this orientation, the bridging fibers are seen "end-on". Micrographs were taken of the entire cross-section and used for measuring the volume fraction of fibers within the crack, following standard quantitative metallographic procedures. Measurements were also made of the local crack opening displacement, $\bar{\delta}$, taken as the ratio of the total crack area to the crack width. The same specimen was then ground and polished further to expose a different section of the crack, and the fiber volume fraction and crack opening displacement measurements were repeated. The measurements were made at numerous locations in several specimens.

Figure 11 shows typical micrographs of the latter sections at four locations, each showing bridging fibers embedded within the crack. An additional notable feature is the presence of small matrix fragments within the crack. Evidently these fragments are produced as the fibers pull away from the crack faces. Consequently, the fragments are of a size comparable to the fiber diameter. Further evidence of matrix fragmentation was obtained through *in-situ* optical observations that were made during some of the delamination experiments. In the latter case, the fragments were seen to be ejected from the specimen during cracking. The inference is that not all of the fragments remain within the crack and hence their volume

fraction cannot be reliably measured from micrographs of the type shown in Fig. 11. Indeed, inspection of the micrographs reveals that the amount of matrix fragments remaining within the crack diminishes at large crack opening displacements, consistent with the observed ejection of the fragments. Similar fragments were also found attached to the surface replicas. A further implication is that the effective crack opening displacement (defined as the average separation between the two matrix crack faces) must be greater than the displacement measured on the side surface using the replication technique. Such effects arise both from matrix fragmentation and fiber debonding. Estimates of the additional crack opening displacement due to these effects are provided in the next section.

The fiber volume fraction measurements are plotted in Fig. 10(b). Again, considerable scatter in the data is evident, the measurements varying by as much as a factor of 2 at fixed δ . However, in contrast to the trend in the fiber angle, V_f^c decreases with increasing δ , following roughly an inverse relationship.

The latter inverse relationship can be rationalized on the basis of the geometric model illustrated in Fig. 12. Here the matrix crack is assumed to propagate through the narrowest ligament between neighboring fibers and all the fibers encountered by the crack are assumed to debond from both faces of the matrix crack and subsequently bridge the crack. The area of each fiber is πr^2 and the relevant crack area per fiber is $L\delta$ where L is the distance between fibers along the crack plane. The latter distance, in turn, can be related to the volume fraction of fibers in the composite, V_f , and the fiber radius through $L = \gamma r \sqrt{\pi / V_f}$, where γ is a numerical coefficient that depends on the fiber array. For the arrays shown in Figs. 12 (a)-(c), γ varies between 1 and 1.41. The resultant fiber area fraction, A_f^c and hence fiber volume fraction, V_f^c is predicted to be

$$A_f^c = V_f^c = \frac{\pi r^2}{L\delta} = \frac{r \sqrt{\pi V_f}}{\gamma \delta} \quad (10)$$

This geometric model can be adapted to cases in which the crack is not planar, but instead follows a zig-zag path between neighboring fibers. One such example is shown in Fig. 12(d). The main effect of the crack following such a path is that the number of fibers intercepted by the crack is greater, as manifest by the lower value of γ (0.71); the dependence of V_f^c on the other parameters (r , V_f and $\bar{\delta}$) remains unchanged.

The predictions of Eqn. 10, for γ values given in Fig. 12, are compared with the experimental measurements in Fig. 10(b). Despite the scatter, the predicted trends appear to be in broad agreement with the measurements. This correlation suggests that the *number* of fibers within the crack remains roughly constant (independent of δ), without appreciable fiber fracture occurring during opening. Nevertheless, the scatter in the measurements indicates that the material is rather heterogeneous, with some regions of the crack exhibiting considerably higher fiber volume fractions than others. This scatter is believed to be a major source of scatter in the measured conductance.

3.3 Comparison of Model and Experiment

The predictions of the crack conductance model are compared with the measurements in Fig. 13. For the model, V_f^c is assumed to follow Eqn. 10, with an average value of γ (≈ 1.1), and the fiber angle is fixed at its average value, 8° . Furthermore, for simplicity, the functions g_i in Eqn. 9 are taken to be unity. With these assumptions made, the model yields a predicted conductance:

$$h = \frac{k_a}{\bar{\delta}} + \frac{k_f}{\bar{\delta}} \frac{\sqrt{\pi V_f}}{\gamma} \left[\frac{\sin \theta}{\sin \theta + \bar{\delta}/r} - \frac{k_a}{k_f} \frac{r}{\bar{\delta}} \right] \quad (11)$$

As noted, the effective crack opening displacement, $\bar{\delta}$, is greater than the measured displacement, δ , in part because of the matrix fragmentation that occurs during delamination. The additional displacement due to this process is taken as Ωr where Ω is a numerical coefficient, expected to be of order unity. Yet an additional component of crack opening displacement is obtained from the separation of the fibers from the matrix, thereby causing fiber bridging. Using the fiber arrays in Fig. 12, this component is predicted to be $\pi r^2/L = r \sqrt{\pi V_f} / \gamma$. Combining these two effects yields the relation:

$$\bar{\delta} = \delta + r \left(\Omega + \sqrt{\pi V_f} / \gamma \right) \quad (12)$$

The calculated curves in Fig. 13 are for Ω values of 0, 1 and 2. Also shown are the predictions based on air conduction alone, $k_a/\bar{\delta}$, using the same Ω values. (The latter estimates of the air conduction are lower than the ones shown on Fig. 7 because of the higher crack opening displacement.) Despite the scatter in the experimental data and the uncertainty in some of the bridging parameters, the crack conductance model appears to agree well with the experimental measurements over the entire range of δ .

The difference between the full model (incorporating bridging effects) and the estimate based on air conductance alone is especially pronounced at low values of δ , by almost an order of magnitude. In this regime, the full model agrees well with the measurements. At large values of δ ($\geq 100\mu\text{m}$), the contributions from fiber bridging become small and thus the two sets of predictions converge, both correlating well with the measurements. It should be noted that the reduction in the *relative* contribution from bridging at large values of δ is due to the reduction in the fiber volume fraction within the crack (through Eqn. 10), not to the increased length of these fibers. For large values of δ , it can be readily shown that the ratio, ϵ , of the

contribution from the fibers (the second term on the right side of Eqn. 11) and that from the air ($k_a/\bar{\delta}$) is given approximately by

$$\varepsilon = \frac{r\sqrt{\pi V_f}}{\gamma\bar{\delta}} \frac{k_f}{k_a} \sin \theta \quad (13)$$

This reveals an inverse dependence on $\bar{\delta}$. To illustrate the effect further, taking $\bar{\delta} = 10\mu\text{m}$, the predicted ratio becomes $\varepsilon \approx 10$; that is, the fiber contribution is about an order of magnitude greater than the air contribution. In contrast, for $\bar{\delta} = 100\mu\text{m}$, $\varepsilon \approx 1$. Fiber fracture at large values of $\bar{\delta}$ would reduce this ratio further yet, but evidently this does not occur to an appreciable extent over the range of $\bar{\delta}$ probed by the present experiments.

4. CONCLUDING REMARKS

An experimental technique for measuring the conductance of delamination cracks *in-situ* under load has been demonstrated on a unidirectional CMC. The measurements indicate a strong dependence of conductance on crack opening displacement. A rudimentary model that takes into account the contributions from the air and the bridging fibers has been developed. Despite the scatter in the measurements, broad agreement between the model and the measurements is obtained. The scatter is believed to be due mainly to the intrinsic variability in the extent of fiber bridging, as evidenced by the measurements of the fiber angle and fiber volume fraction within the crack, coupled perhaps with variations in the extent of matrix fragmentation. In light of this scatter, further refinements in the model are probably not warranted at this time.

A salient feature of the delamination process revealed by the present experiments pertains to the difference between the opening displacements obtained

from surface measurements and the actual crack face separation. The latter quantity is greater because of fragmentation of the matrix as well as separation of the fibers from the matrix. For this reason, the predictions of crack conductance based on air conduction alone, using the crack opening displacement from surface measurements, is anomalously high and the resulting correlations with the measurements at small crack opening displacements is fortuitous. The conductance in this regime is adequately described by the crack bridging model, using more realistic estimates of the crack opening displacement, obtained through appropriate corrections to the surface measurements.

The present crack conductance model tacitly assumes that the contribution from the fibers occurs by heat flow directly along the length of the bridging fibers at an angle, θ , from one crack surface to the other. For very small opening displacements (less than a fiber radius), a significant component is expected to arise from heat flowing along a path normal to the crack plane, first passing through the air gap adjacent to the fibers and then through the fibers themselves. A model for this pattern of heat flow would be intrinsically 3-dimensional in nature. Furthermore, when the displacements are $\leq 1 \mu\text{m}$, the contributions from air would be dictated by the mean free path of the molecules, independent of δ . For these reasons, the present model is restricted to the regime of larger crack opening displacements, roughly in the range $\delta \geq 5 \mu\text{m}$.

ACKNOWLEDGMENTS

This material is based upon work supported by the Office of Naval Research under Award No. N00014-97-1-0394 (Contract Officer: Dr. Stephen G. Fishman).

REFERENCES

1. D.P.H. Hasselman, A. Venkateswaran, M. Yu and H. Tawil, "Role of Interfacial Debonding and Matrix Cracking in the Effective Thermal Diffusivity of SiC-Fiber-Reinforced Chemical Vapor Deposited SiC Matrix Composites", *J. Mater. Sci.*, **10** 1037-1042 (1991).
2. D.P.H. Hasselman, A. Venkateswaran and H. Tawil, "Role of Interfacial Debonding and Matrix Cracking in the Effective Thermal Diffusivity of Alumina-Fiber-Reinforced Chemical Vapor Infiltrated SiC Matrix Composites", *J. Am. Ceram. Soc.*, **74** [7] 1631-1634 (1991).
3. T.J. Lu and J.W. Hutchinson, "Effect of Matrix Cracking on the Overall Thermal Conductivity of Fibre-reinforced Composites", *Phil. Trans. Royal Soc. London , Series A - Phys. Sci. Eng.*, **351** [1697] 595-610 (1995).
4. K.Y. Donaldson, B.D. Trandell, Y. Lu and D.P.H. Hasselman, "Effect of Delamination on the Transverse Thermal Conductivity of a SiC-Fiber-Reinforced SiC-Matrix Composite", *J. Am. Ceram. Soc.*, **81** [6] 1583-1588 (1998).
5. K.R. McDonald, J.R. Dryden, A. Majumdar, and F.W. Zok, "Influence of Multiple Matrix Cracks on the In-plane Thermal Diffusivity of Ceramic Composites", in preparation.
6. J.W. Hutchinson and T.J. Lu, "Laminate Delamination Due to Thermal Gradients", *J. Eng. Mat. Tech. - Transactions of ASME*, **117** [4] 386-390 (1995).
7. Y. Ohsone, G. Wu, J.R. Dryden, F.W. Zok and A. Majumdar, "Optical Measurement of Thermal Contact Conductance Between Wafer-Like Thin Solid Samples", *J. Heat Transfer*, in press (1999).
8. J. Parker, R.J. Jenkins, C.P. Butler, and G.L. Abbot, "A Flash Method of Determining Thermal Diffusivity, Heat Capacity, and Thermal Conductivity", *Journal of Applied Physics*, **32** (1961) 1679.
9. M.A. Lambert and L.S. Fletcher, "Review of Models for Thermal Contact Conductance of Metals", *J. Thermophysics Heat Transfer*, **11** [2] 129-140 (1997).

10. B.B. Mikic, "Thermal Contact Conductance; Theoretical Considerations", *Int. J. Heat Mass Transfer*, **17** [2] 205-214 (1974).
11. M.G. Cooper, B.B. Mikic, and M.M. Yovanovich, "Thermal Contact Conductance", *Int.J.Heat Mass Transfer*, **12** [3] 279-300 (1969).
12. J.J. Brennan, L.D. Bentsen, and D.P.H. Hasselman, "Determination of the Thermal Conductivity and Diffusivity of Thin Fibers by the Composite Method", *J. Mat. Sci.*, **17** [8] 2337-2342 (1982).
13. M. Oksanen, R. Scholz, and L. Fabbri, "On the Longitudinal Thermal Diffusivity of SiC-based Fibres", *J. Mater. Sci. Letters*, **16** [13] 1092-1094 (1997).
14. D.R. Poirier and G.H. Geiger, Transport Phenomena in Materials Processing, TMS, Warrendale, PA, 1994, p. 619.
15. H.S. Carslaw and J.C. Jaeger, Conduction of Heat in Solids, Second Edition, Clarendon Press, Oxford, UK, 1986.

APPENDIX: Heat Flow Analysis

The specimen geometry to be analyzed is shown in the inset of Fig. 1(b). A crack with normalized resistance ρ is situated parallel to the top and bottom surfaces at $z = B$, with z being measured from the top surface. A periodic heat source is input at $(r, z) = (0, 0)$ at a frequency $\omega = 2\pi f$. The top and bottom surfaces are taken to be insulating. Solutions for the steady periodic temperature and the phase lag relative to the heat input at various positions on the specimen surface are presented below. The limiting case of $\rho = 0$ represents the one in which the crack is absent and the corresponding result is used to determine the thermal diffusivity.

The temperatures in the regions $0 < Z < B$ and $B < Z < A$ are denoted $v(r, z, t)$ and $u(r, z, t)$, respectively; they are required to satisfy the heat flow equations [15]

$$\frac{\partial^2 u}{\partial r^2} + \frac{1}{r} \frac{\partial u}{\partial r} + \frac{\partial^2 u}{\partial z^2} - \frac{1}{\alpha} \frac{\partial u}{\partial t} = 0 \text{ and } \frac{\partial^2 v}{\partial r^2} + \frac{1}{r} \frac{\partial v}{\partial r} + \frac{\partial^2 v}{\partial z^2} - \frac{1}{\alpha} \frac{\partial v}{\partial t} = 0 \quad (\text{A1})$$

where r is the radial distance from the z -axis. At the interface ($z = B$), there is a heat flow balance and the discontinuous temperature jump is proportional to the flux, such that $\partial u / \partial z = \partial v / \partial z = (h/k)(u-v)$. The flux condition on the top surface is given by

$$-k \frac{\partial v}{\partial z} = \frac{Q}{\pi a^2} H(a-r) \cos \omega t \quad (\text{A2})$$

where $H(a-r)$ is the step function, Q is the power, and a is the radius of the spot, assumed to be infinitesimal.

The steady periodic component of the temperatures on the top and bottom surfaces are found to be (in complex form):

$$v(r,0,t) = \exp[-i\omega t] \left\{ \frac{Q}{2\pi k} \frac{\exp[-pr]}{r} + \int_0^\infty E(\eta) J_0(\lambda r) \lambda d\lambda \right\} \quad (A3(a))$$

$$u(r,A,t) = \frac{Q}{2\pi k} \exp[-i\omega t] \left\{ \int_0^\infty \frac{J_0(\lambda r) \lambda d\lambda}{\eta(\sinh \eta A + 2A \rho \eta \sinh \eta B \sinh \eta C)} \right\} \quad (A3(b))$$

where $\eta = \sqrt{\lambda^2 + p^2}$, $p^2 = -i\omega/\alpha$ and the coefficients $F(\eta)$, $D(\eta)$ and $E(\eta)$ are:

$$\begin{aligned} F(\eta) &= \frac{Q}{k\pi n} \frac{J_1(\lambda a)}{\lambda a} \sim \frac{Q}{2k\pi\eta} \quad \text{as } a \rightarrow 0 \\ D(\eta) &= \frac{Q}{2k\pi\eta} \left[\frac{1}{\sinh \eta A + 2A \rho \eta \sinh \eta B \sinh \eta C} \right] \\ E(\eta) &= \frac{Q}{2k\pi\eta} \left[\frac{e^{-\eta B} (\sinh \eta A + 2A \rho \eta \sinh \eta B \sinh \eta C) - \sinh \eta C}{\sinh \eta B (\sinh \eta A + 2A \rho \eta \sinh \eta B \sinh \eta C)} \right] \end{aligned} \quad (A4)$$

with $C = B - A$. The phase lag with respect to the heat input is the argument ϕ of the complex portions of the temperatures in Eqns. A3.

In the absence of a crack ($\rho=0$), the phase lag is dictated by the thermal diffusivity, α . For the purpose of determining α , it is convenient to measure the temperature on the top surface (as shown in the inset of Fig. 1(a)). In this case, the integral in Eqn. A3(a) can be evaluated as an infinite series, yielding the result

$$v_0(r,0,t) = \frac{Qe^{-i\omega t}}{2\pi k} \sum_{n=0,\pm 2,\pm 4,\dots} \frac{\exp[-\beta(1-i)R_n]}{R_n} \quad (A5)$$

where $R_n = \sqrt{r^2 + n^2 A^2}$ and the phase lag is the argument of the summed series.

This result is equivalent to that obtained from the method of images, using a line of image sources placed along the z -axis with the sources located symmetrically at intervals of $2A$ so as to satisfy the adiabatic conditions at $z = 0$ and $z = A$.

Figure 1(a) shows the variation in ϕ with βr for various values of r/A , calculated from Eqn. A5. When $r/A \ll 1$, the term corresponding to $n = 0$ dominates. This situation is identical to that of a point source in an infinite body, wherein the phase lag is simply $\phi = \beta r$. For larger values of r/A , the image sources contribute progressively more to the sum.

Solutions for the phase lag at other locations on the specimen can be derived in a similar manner. For example, the temperature along the bottom surface can be written as

$$u_o(r, A, t) = \frac{Qe^{-i\omega t}}{2\pi k} \sum_{n=\pm 1, \pm 3, \pm 5, \dots} \frac{\exp[-\beta(1-i)R_n]}{R_n} \quad (A6)$$

and the phase lag is again obtained from the argument of the summed series. Numerical results for the phase lag along the bottom surface directly opposite the heat source are shown in Fig. 1(b) (labeled $\rho=0$).

In the presence of a crack ($\rho \neq 0$), the phase lag is measured and interpreted most conveniently on the bottom surface directly opposite the heat source. When the crack is at the mid-plane ($B = A/2$), the expression for $u(0, A, t)$ becomes:

$$u(0, A, t) = \frac{Q}{2\pi k} \exp[-i\omega t] \left\{ \int_0^\infty \frac{\lambda d\lambda}{\eta(\sinh \eta A + A \rho \eta \{\cosh \eta A - 1\})} \right\} \quad (A7)$$

This integral was solved using Simpson's parabolic formula. Fig. 1(b) shows the variation in phase lag ϕ with βA for values of ρ ranging from 0 to 10^3 .

At high frequencies ($\beta A > 1$) and when the thermal resistance of the crack is low ($\rho \ll 1$), it can be shown that the phase lag tends towards the result in Eqn. 3 of the text [7]. This is a useful formula because it reveals the first order effect of the interface upon the phase lag.

FIGURES

- Figure 1 Predictions of phase lag (a) measured on the top surface of a plate (without a crack) and (b) on the bottom surface, directly across from the heat source, with a crack located along the midplane. The dashed line in (b) shows the solution for high frequencies ($\beta A > 1$) and $\rho = 0$.
- Figure 2 Schematic of apparatus for making photothermal measurements *in-situ* under load.
- Figure 3 Schematic of the specimen and loading configuration used to produce delamination cracks and subsequently measure their thermal conductance.
- Figure 4 Series of surface replicas, illustrating the increase in crack opening (a) $\delta = 0$, (b) $18\mu\text{m}$, (c) $50\mu\text{m}$ and (d) $88\mu\text{m}$. The lines in each of the figures are of the same length and represent the initial separation of two surface features (prior to cracking).
- Figure 5 Phase lag measurements on pristine composite both parallel and perpendicular to the fiber direction.
- Figure 6 Typical measurements and calculations for the phase lag across a delamination crack at various opening displacements.
- Figure 7 Effect of crack opening displacement on the crack conductance.
- Figure 8 Optical micrograph showing a bridging fiber at a slight angle to the matrix crack.
- Figure 9 Schematic representation of (a) a bridging fiber and (b) the thermal resistance associated with the fibers and the air.
- Figure 10 Influence of crack opening displacement on (a) the fiber angle, θ , and (b) the fiber volume fraction within the crack, V_f^c . Also shown in (b) are the predictions of the geometric model, based on the fiber arrays in Fig. 12 and Eqn. 10.

- Figure 11 Micrographs showing the fibers within the delamination crack at effective crack opening displacements, δ , of (a) 40 μm , (b) 65 μm , (c) 100 μm and (d) 250 μm . The arrows indicate some of the matrix fragments embedded within the crack.
- Figure 12 Schematics showing the fiber arrays and crack trajectories used in calculating the fiber volume fraction within a delamination crack.
- Figure 13 Comparisons of measured and predicted crack conductances. The top set of lines are based on Eqn. 11, for $\Omega = 0, 1$ and 2; the bottom set are based on air conductance alone (without bridging) for the same values of Ω .

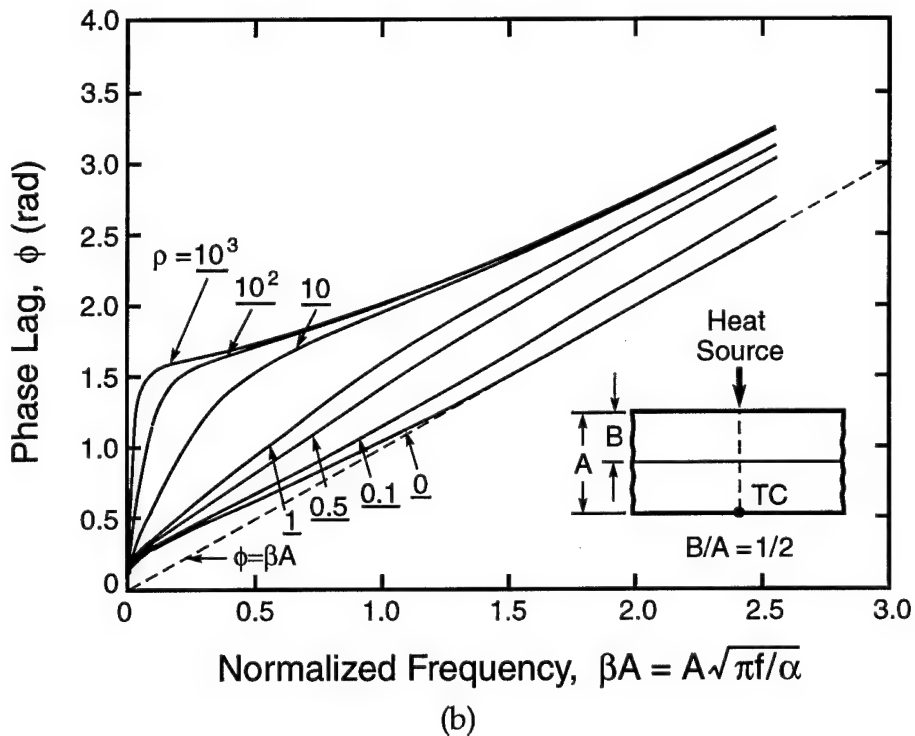
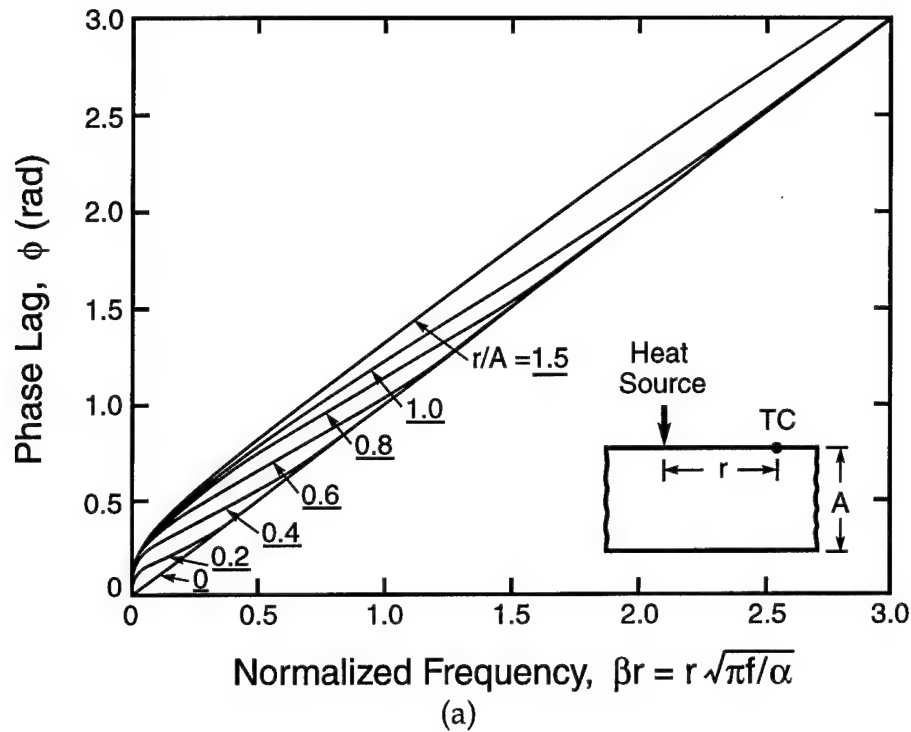


Figure 1 Predictions of phase lag (a) measured on the top surface of a plate (without a crack) and (b) on the bottom surface, directly across from the heat source, with a crack located along the midplane. The dashed line in (b) shows the solution for high frequencies ($\beta A > 1$) and $\rho = 0$.

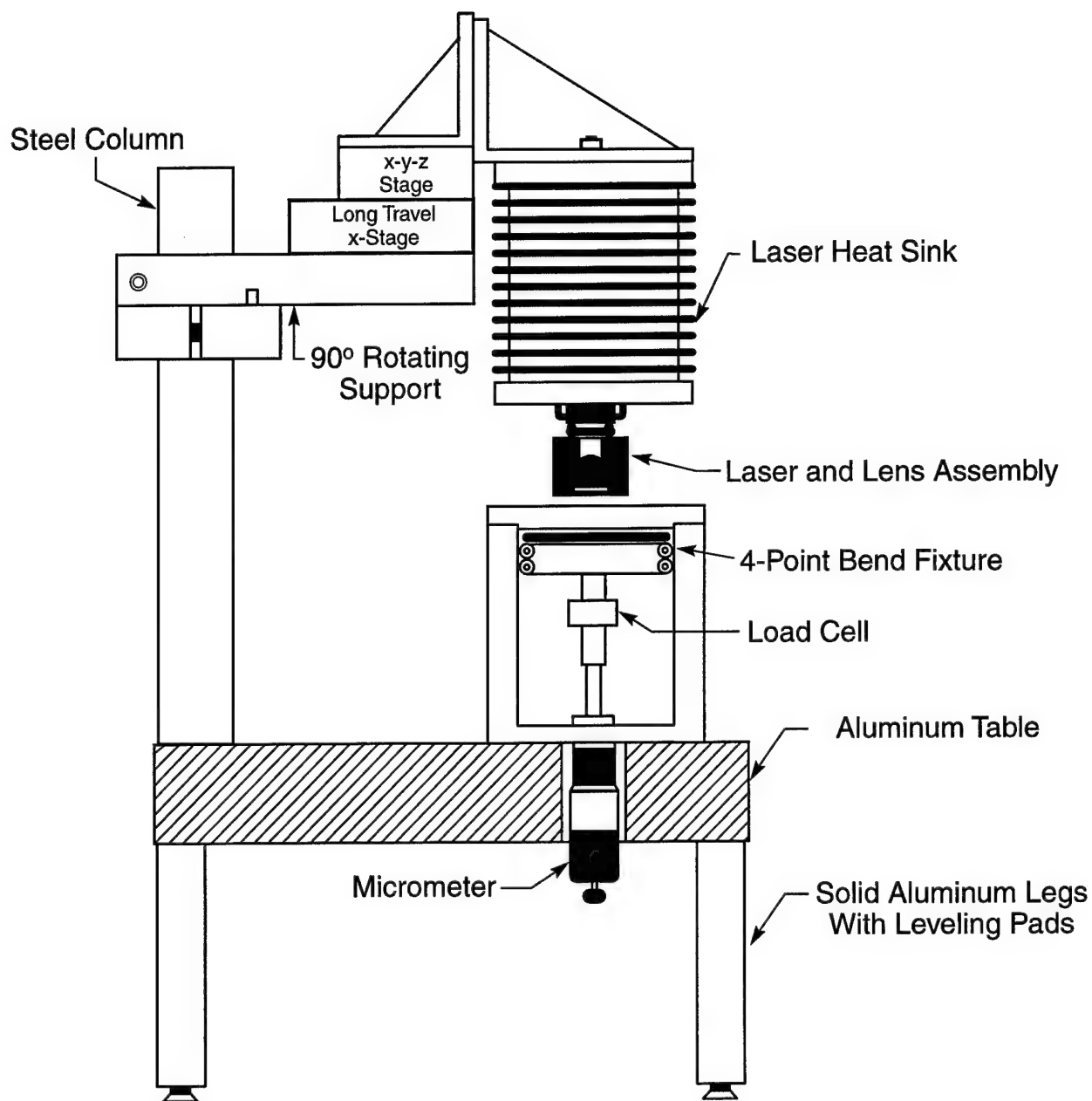


Figure 2 Schematic of apparatus for making photothermal measurements *in-situ* under load.

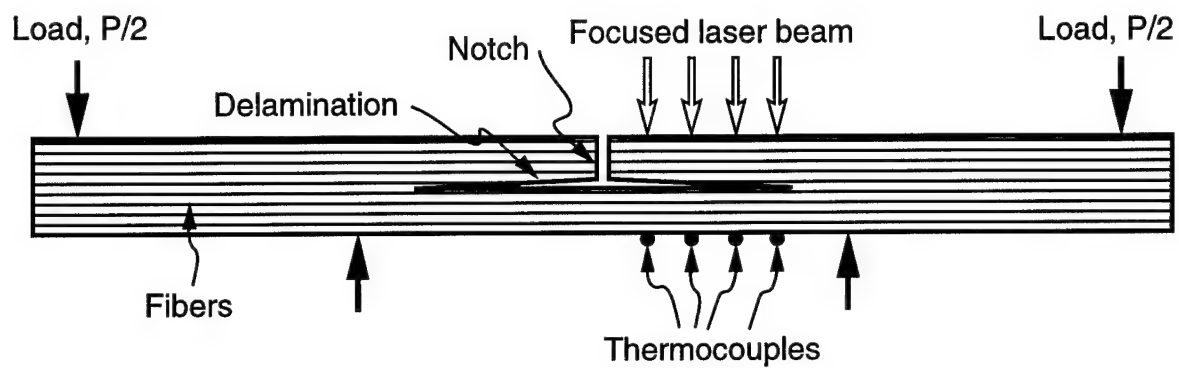


Figure 3 Schematic of the specimen and loading configuration used to produce delamination cracks and subsequently measure their thermal conductance.

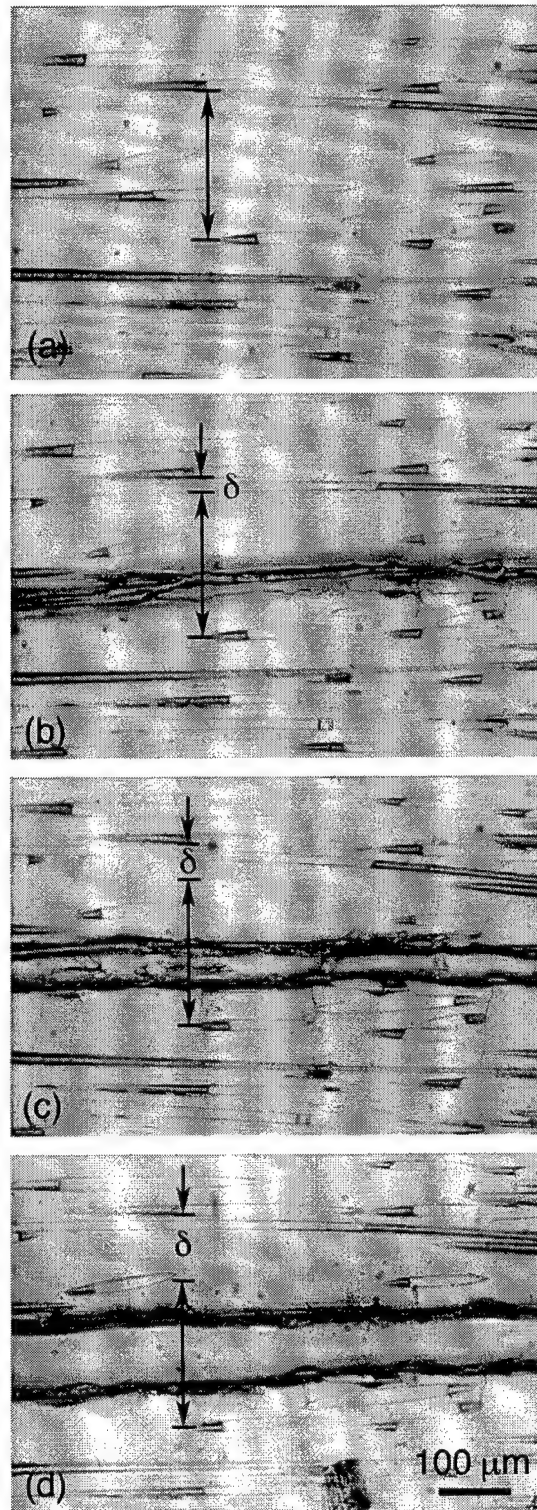


Figure 4 A series of surface replicas, illustrating the increase in crack opening: (a) $\delta = 0$, (b) 18 μm , (c) 50 μm and (d) 88 μm . The lines in each of the figures are of the same length and represent the initial separation of two surface features (prior to cracking).

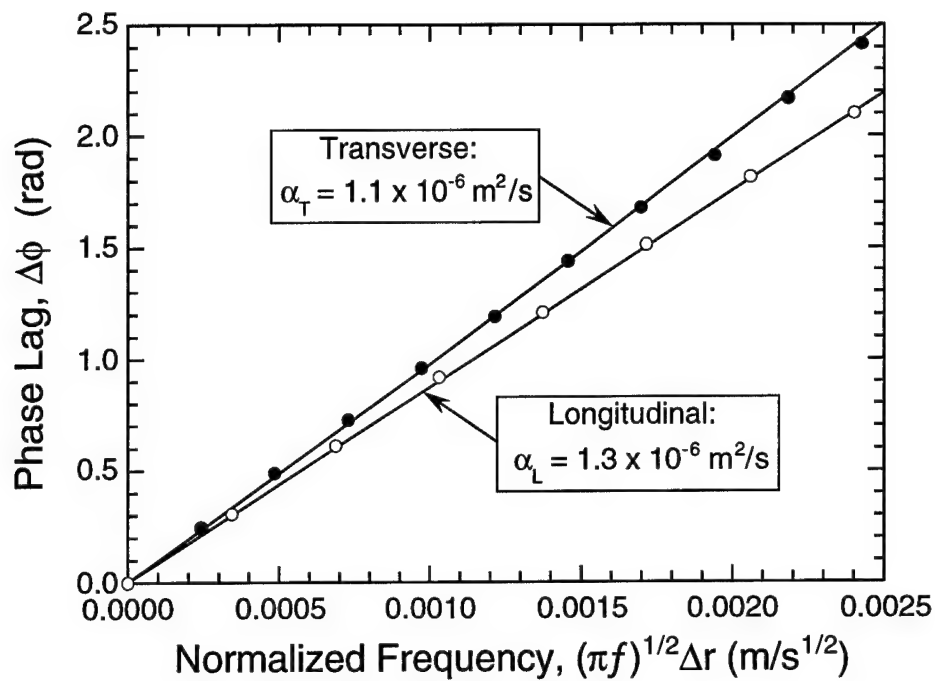


Figure 5 Phase lag measurements on pristine composite both parallel and perpendicular to the fiber direction.

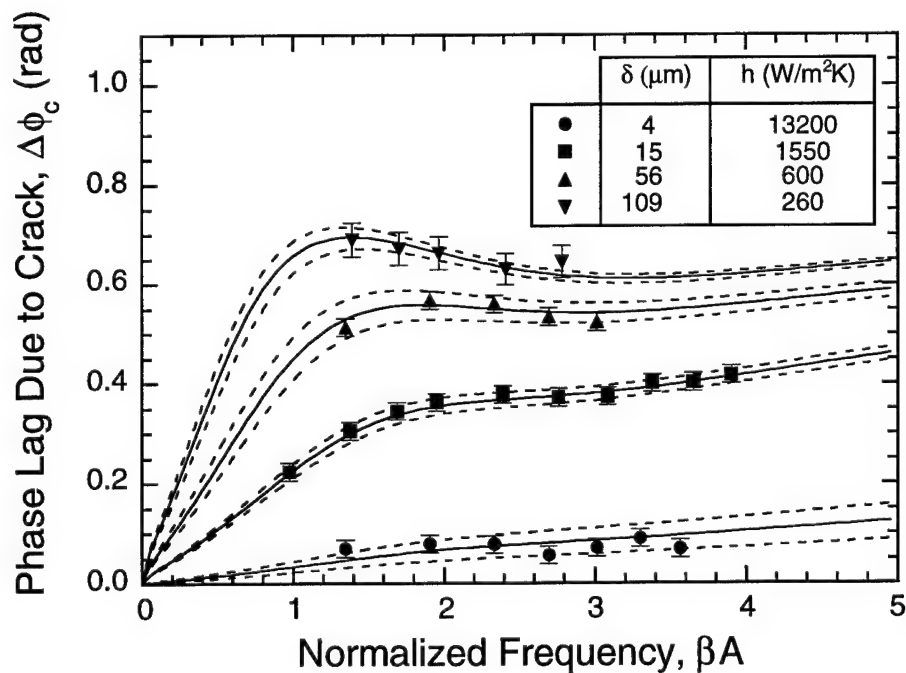


Figure 6 Typical measurements and calculations for the phase lag across a delamination crack at various opening displacements.

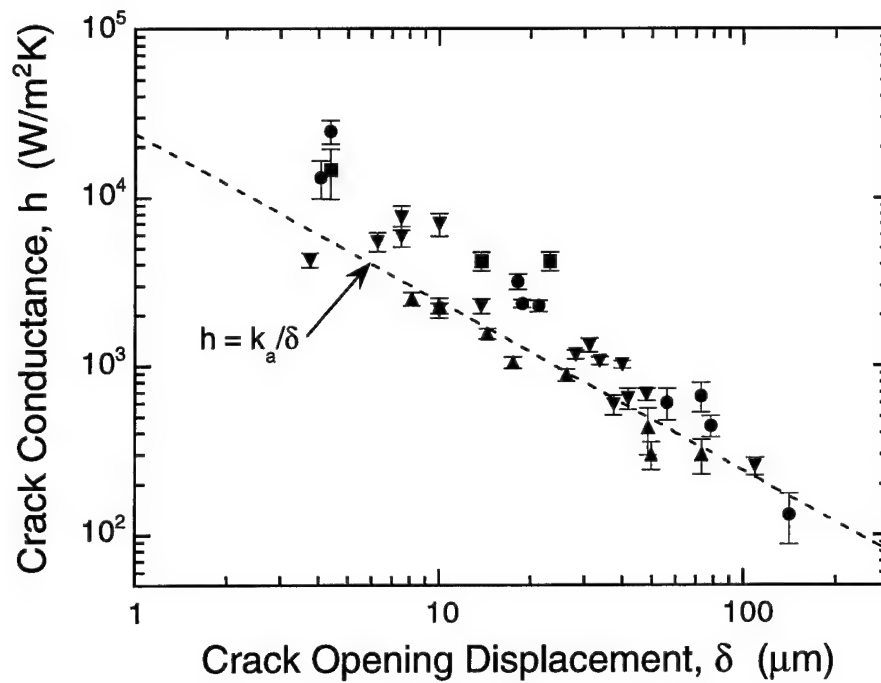


Figure 7 Effect of crack opening displacement on the crack conductance.

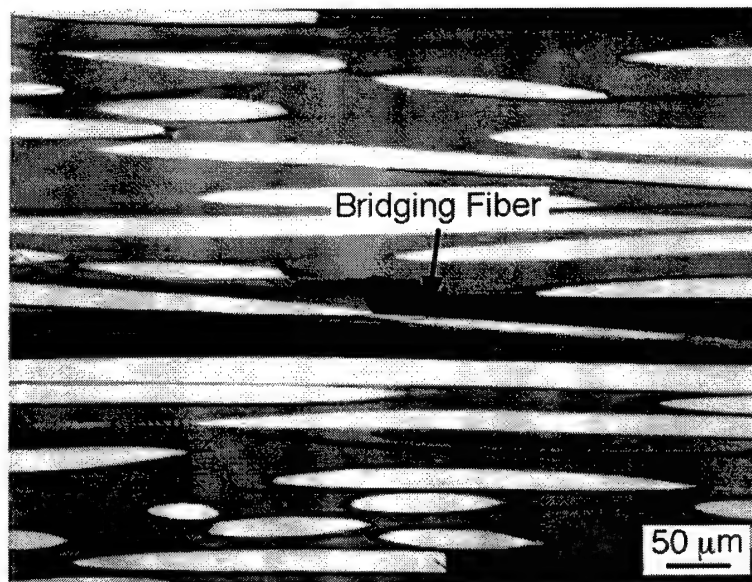
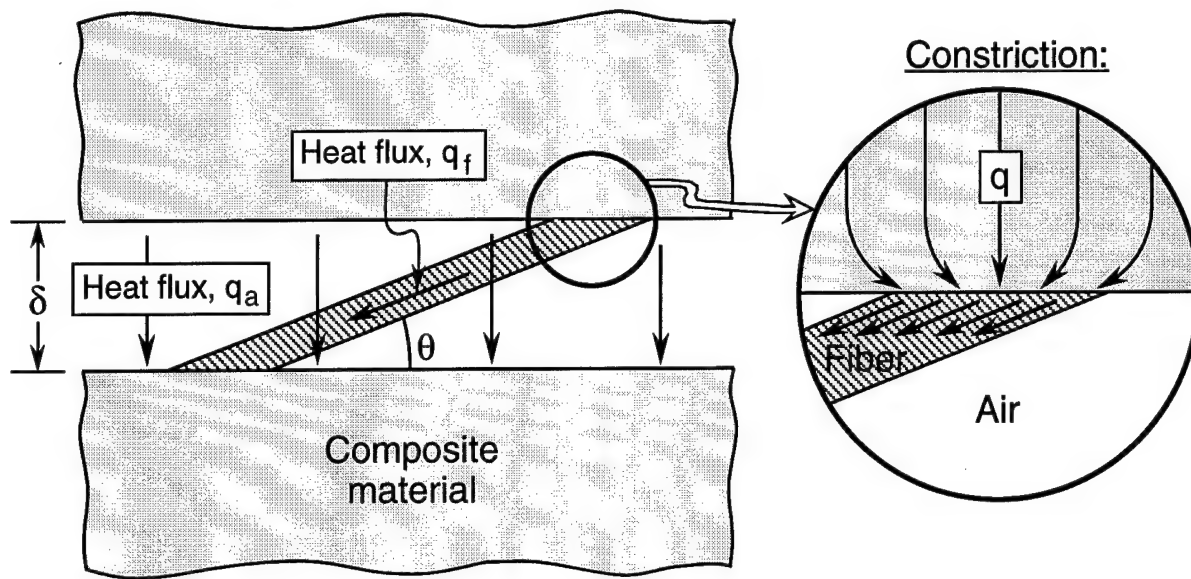
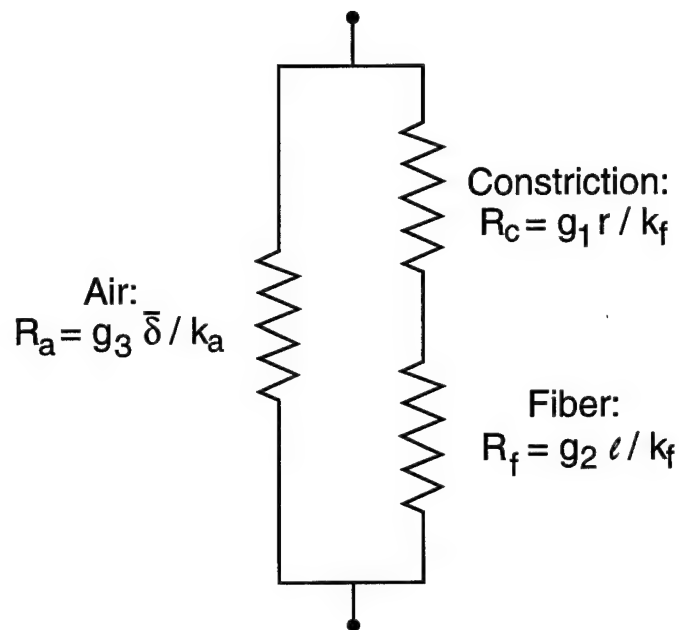


Figure 8 Optical micrograph showing a bridging fiber at a slight angle to the matrix crack.



(a)



(b)

Figure 9 Schematic representation of (a) a bridging fiber and (b) the thermal resistance associated with the fibers and the air.

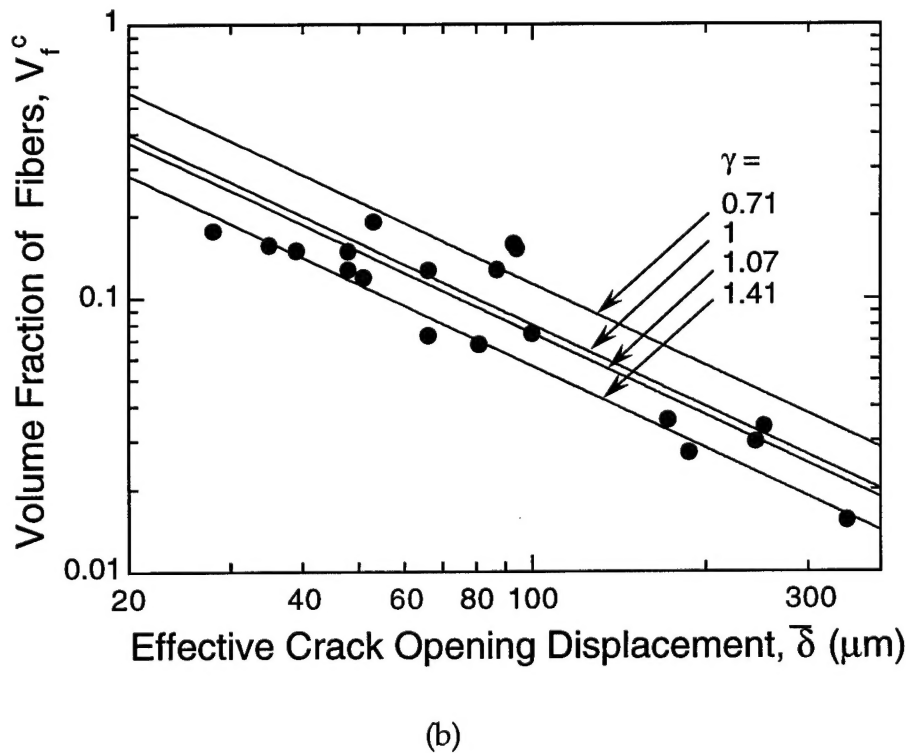
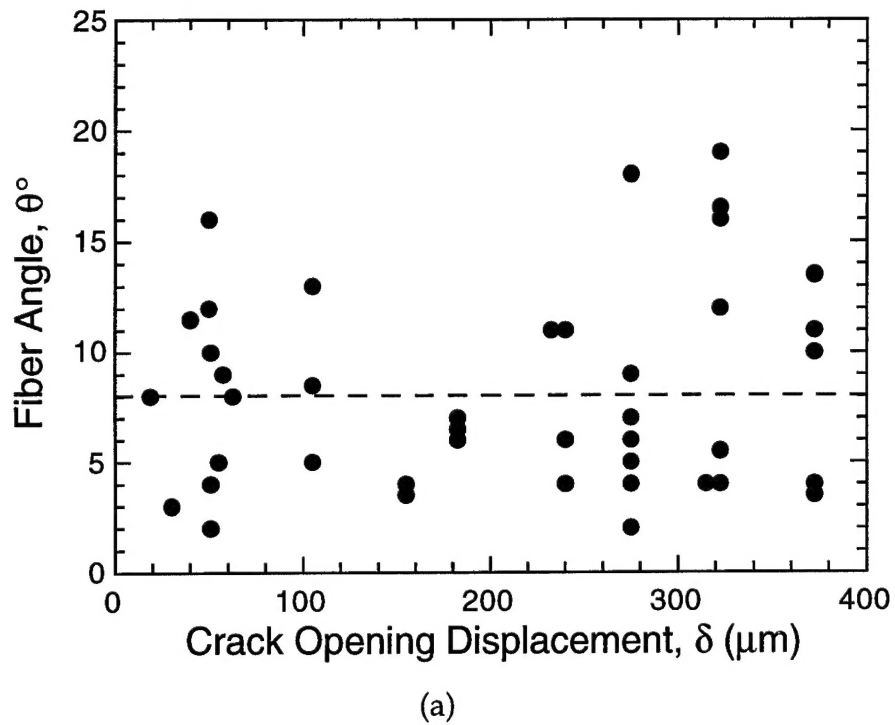


Figure 10 Influence of crack opening displacement on (a) the fiber angle, θ , and (b) the fiber volume fraction within the crack, V_f^c . Also shown in (b) are the predictions of the geometric model, based on the fiber arrays in Fig. 12 and Eqn. 10.

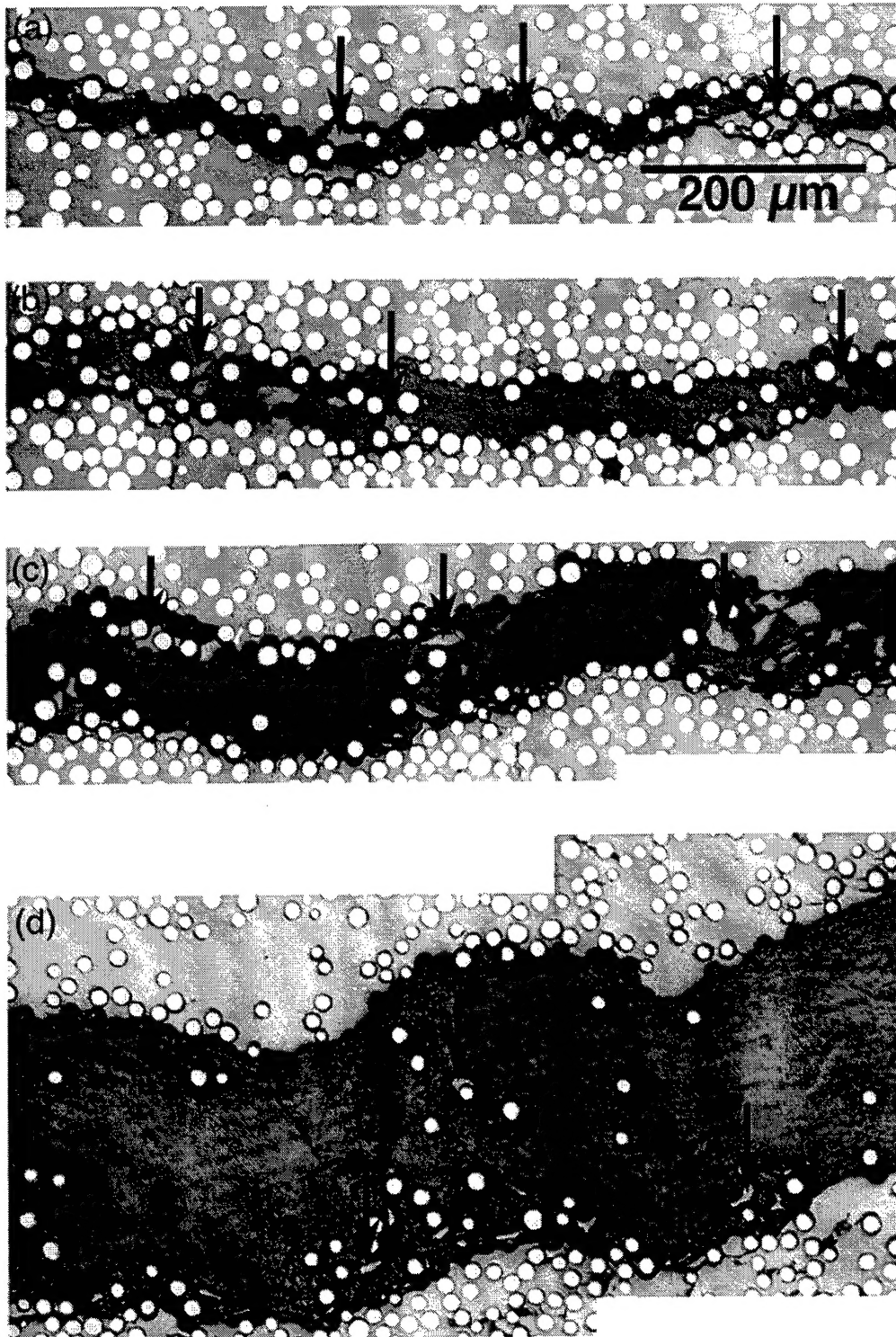
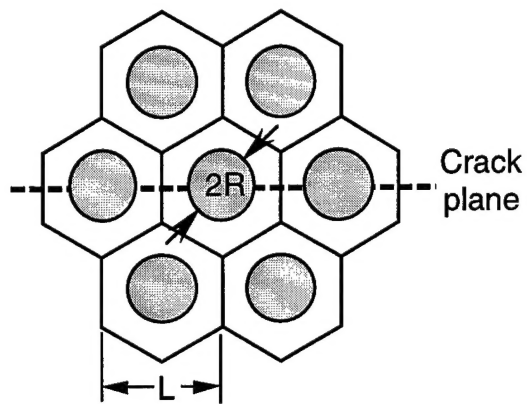
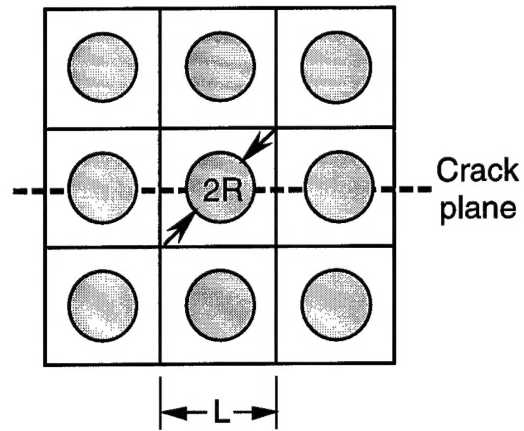


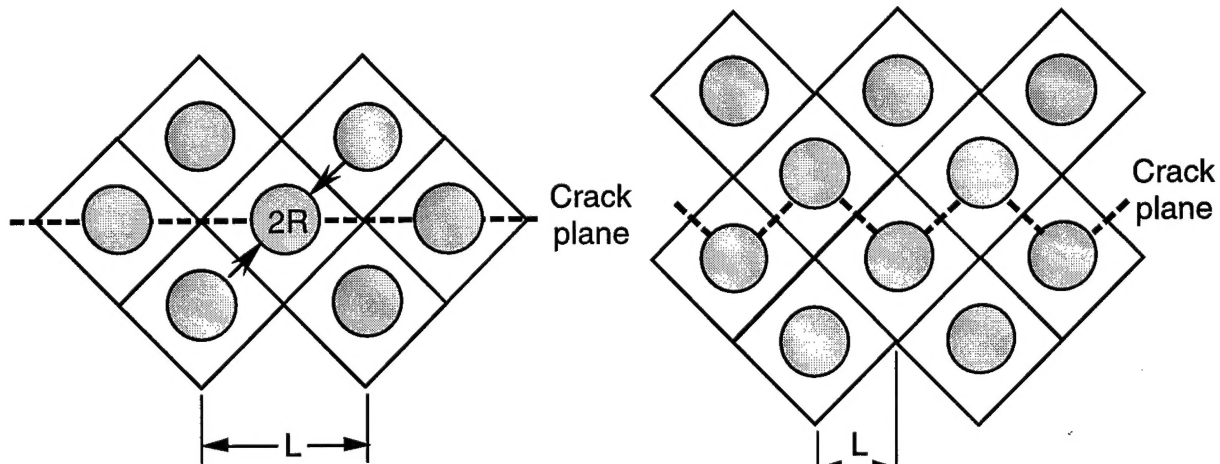
Figure 11 Micrographs showing the fibers within the delamination crack at effective crack opening displacement, δ , of (a) $40\mu\text{m}$, (b) $65\mu\text{m}$, (c) $100\mu\text{m}$ and (d) $250\mu\text{m}$. The arrows indicate some of the matrix fragments embedded within the crack.



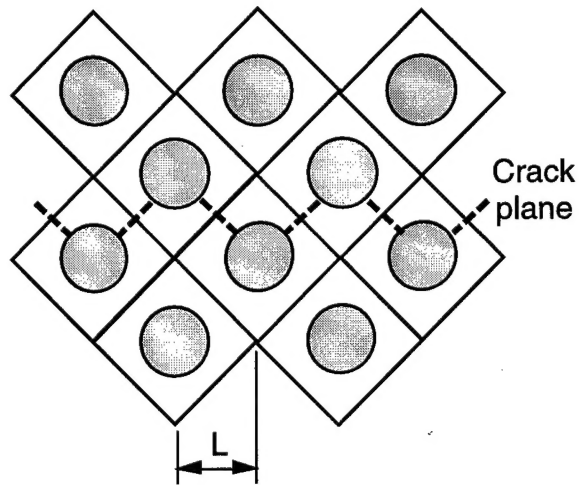
(a) $\gamma = \sqrt{2/\sqrt{3}} \approx 1.07$



(b) $\gamma = 1$



(c) $\gamma = \sqrt{2} \approx 1.41$



(d) $\gamma = 1/\sqrt{2} \approx 0.71$

Figure 12 Schematics showing the fiber arrays and crack trajectories used in calculating the fiber volume fraction within a delamination crack.

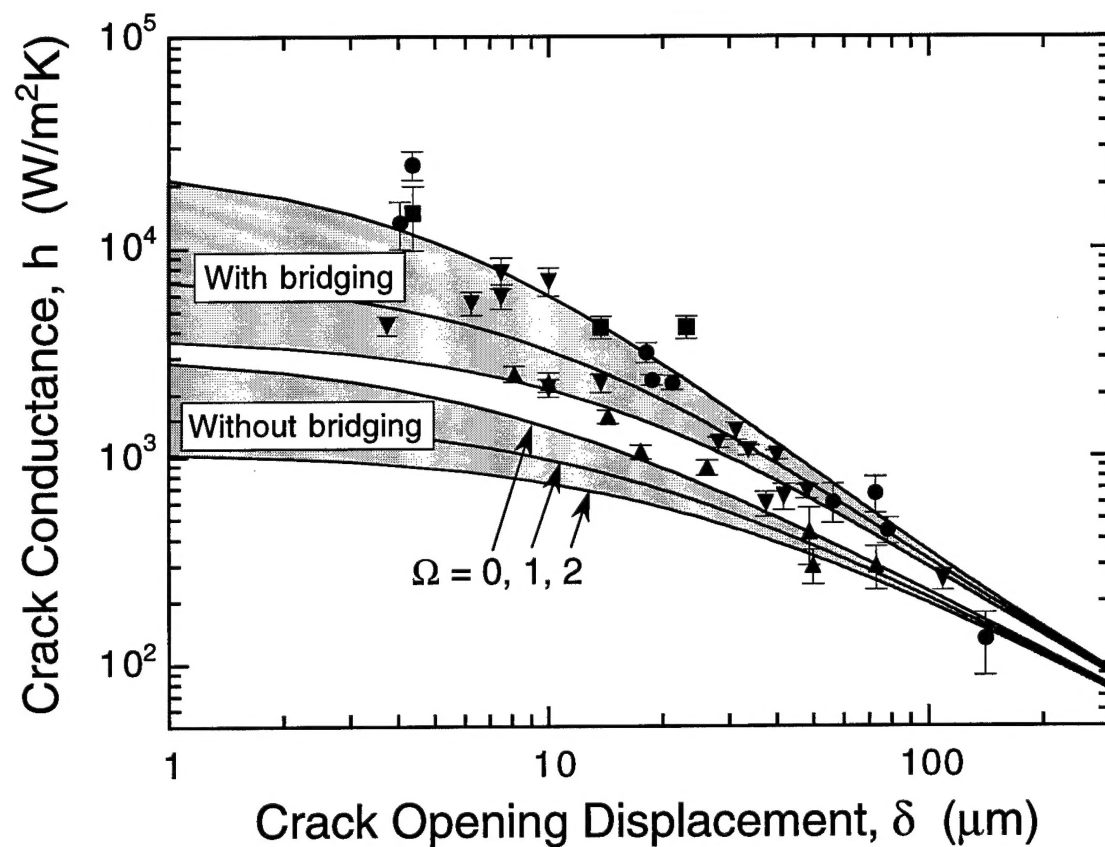


Figure 13 Comparisons of measured and predicted crack conductances. The top set of lines are based on Eqn. 11, for $\Omega = 0, 1$ and 2 ; the bottom set are based on air conductance alone (without bridging) for the same values of Ω .